REPUBLIC OF TURKEY
YILDIZ TECHNICAL UNIVERSITY
GRADUATE SCHOOL OF NATURAL AND APPLIED SCIENCES

AN X-RAY STUDY OF SHELL-TYPE GALACTIC SUPERNOVA REMNANTS

NERGİS CESUR

MSc. THESIS
DEPARTMENT OF PHYSICS
PROGRAM OF PHYSICS

ADVISER
ASSIST. PROF. DR. MURAT HÜDAVERDİ

İSTANBUL, 2018

REPUBLIC OF TURKEY

YILDIZ TECHNICAL UNIVERSITY

GRADUATE SCHOOL OF NATURAL AND APPLIED SCIENCES

AN X-RAY STUDY OF SHELL-TYPE GALACTIC SUPERNOVA REMNANTS

A thesis submitted by Nergis CESUR in partial fulfillment of the requirements for the degree of **MASTER OF SCIENCE** is approved by the committee on 28.03.2018 in Department of Physics, Physics Program.

Thesis Adviser

Assist. Prof. Dr. Murat HÜDAVERDİ

Yıldız Technical University

Co- Adviser

Assoc. Prof. Dr. Aytap SEZER

Avrasya University

Approved By the Examining Committee

Assist. Prof. Dr. Murat HÜDAVERDİ

Yıldız Technical University ______________________

Prof. Dr. E. Nihal ERCAN, Member

Boğaziçi University ______________________

Assoc. Prof. Taylan YETKİN, Member

Yıldız Technical University ______________________

This study was supported by Yıldız Technical University Scientific Research Projects Coordinator (BAPK) Grant No: FYL-2018-3309.

ACKNOWLEDGEMENTS

This work is a result of the expertise, guidance, support, and invaluable assistance from my advisers Dr. Murat HÜDAVERDİ and Dr. Aytap SEZER. A work of this magnitude would not be possible without their knowledge and experience. I'm deeply thankful to Dr. Murat HÜDAVERDİ for his trust in me over so many years. He is always more than an adviser, as he is also a good friend, and a great supporter, who has always been there for me. I would like to thank to Dr. Aytap SEZER; by her who suggesting me this thesis topic, I'm a lucky person that able first to study the PeVatron research in supernova remnants in Turkey. This thesis proved to be an incredible learning experience that would not have been as enriching without her as an adviser, for that I am very grateful. Her guidance, as well as her warm friendship, helped me make to finish the line.

Foremost, I would like to give my thanks and gratitude to my family for all their support over so many years. Without their encouragement, I would not have even started on such a long path that has eventually led to this work.

I also would like to thank to Turkish Air Force Academy in National Defence University, for providing me with opportunity to give physics laboratory lectures to the future fighter pilots. That will remain one of the most important experiences in my life, which provided me a great mood through the finishing touches of my thesis.

Finally, I, of course, owe thanks for all the support that I have received from fellow students of our laboratory and friends. I would like to express my gratitude to Onur ÜNVER, İlker KAYA, Kıyami ERDİM and Hakan SERT for many great chats and for all the brainstorming about each other's studies. And the final thanks are for Betül BİLİCİ, a best friend and a great supporter.

March, 2018

Nergis CESUR

TABLE OF CONTENTS

Page

LIST OF SYMBOLS

°C	Degree Celsius
α	Fine structure constant
Å	Ångstrom
μ	Mean atomic weight with chemical abundance of solar values
μm	micrometre
ν	Frequency
ν_e	Electron neutrino
νf_{ree}	Velocity for the ejecta
ν_s	Velocity of the blast wave
γ	gamma
λ	lambda, wavelength
Ω	Angular frequency
σ_T	Thomson cross-section
$\sigma_Z(E)$	Cross section of element Z at energy E
ρ_0	Ambient density
τ_{sync}	Synchrotron energy loss time
θ	Electron pitch angle
$B_{\perp}$	Magnetic field perpendicular to the particle orbit
C	Carbon
c	speed of light
C_v	Specific heat at constant volume
C_p	Specific heat at constant pressure
dl	Optical path length over which absorption takes place
e	electron
E	Energy
E_0	Initial explosion energy
E_I	Electron binding energy
E_ν	Photon energy
F	Flux
Fe	Ferrum (Iron)
$g_{ff}(T,\nu)$	Velocity-averaged Gaunt factor
h	Planck's constant
H	Hydrogen
He	Helium
I	Moment of inertia
k_B	Boltzmann's constant
K	Kelvin
$M_\odot$	Mass of the Sun

M	Mass
M_0	Mass of the ejecta
m_e	Mass of the electron
M_{Ej}	Ejecta mass
Mg	Magnesium
m_H	Mass of hydrogen atom
M_{ISM}	Swept-up ambient mass
M_s	Mass of the shell
n_0	Hydrogen ambient density
n	neutron
n_e	Electron density
N_e	Total number of electrons bounded to the shell
Ne	Neon
n_H	Number density of the hydrogen
n_i	Ion density
n_z	Number density of the absorbing element with the atomic number Z
O	Oxygen
P	Pressure
p	proton
R_{free}	Radius of the SNR
R_s	Radius for the expanding shell
s	second
S	Sulfur
Si	Silicon
t	Time
t_{age}	Age of the SNR
t_{kyr}	Age of the SNR in units of 1000 yrs
T_s	Mean temperature behind the shock front
t_{sedov}	Sedov age
V	Volume
Z	Atomic number

LIST OF ABBREVIATIONS

ACIS	Advanced CCD Imaging Spectrometer
arcsec	arcsecond
ARF	Ancillary Response File
ASCA	Advanced Satellite for Cosmology and Astrophysics
ATS	Acceleration time scale
AXAF	Advanced X-ray Astrophysics Facility
AXP	Anomalous X-ray Pulsar
CALDB	Calibration Database
CCD	Charged Coupled Devices
CD	Contact Discontinuity
CIE	Collisional Ionisation Equilibrium
cm	centimetre
CR	Cosmic Ray
CSM	Circumstellar Medium
CXB	Cosmic X-ray Background
CXO	Chandra X-ray Observatory
DDT	Deflagration Detonation Transition
EPIC	European Photon Imaging Camera
ERM	EPIC Radiation Monitor
ESA	European Space Agency
eV	electron-volt
FE	Foreground Emission
FMK	Fast-Moving Knot
FoV	Field of View
FPA	Focal Plane Assembly
FPP	Focal Plane Platform
FS	Forward Shock
FWHM	Full Width at Half Maximum
g	gram
GeV	Giga electron-Volt
GH	Galactic Halo
GRXE	Galactic Ridge X-ray Emission
h	hour
HETGS	High Energy Transmission Grating Spectrometer
HRC	High Resolution Camera
HRMA	High Resolution Mirror Assembly

IME	Intermediate Mass Element
ISM	Interstellar Medium
JFET	Junction Field Effect Transistor
keV	kilo electron-Volt
km	kilometre
LETGS	Low Energy Transmission Grating Spectrometer
LHB	Local Hot Bubble
m	meter
MCP	Micro-Channel Plates
MeV	Mega electron-Volt
MIT	Massachusetts Institute of Technology
MOS	Metal Oxide Semi-conductor
MSP	Mirror Support Platform
N	North
NASA	National Aeronautics and Space Administration
NE	North-east
NEI	Non-equilibrium Ionisation
nm	nanometre
NRAO	National Radio Astronomy Observatory
NT	Non-thermal
NW	North-west
OGB	Outgassing Baffle
OM	Optical Monitor
pc	parsec
PL	Power-law
PM	Proper motion
PS	Post-shock
QSF	Quasi-Stationary Flocculi
RGS	Reflection Grating Spectrometer
RMF	Response Matrix File
ROSAT	Röntgensatellit
RS	Reverse shock
RSG	Red Supergiant
RXTE	Rossi X-ray Timing Explorer
SE	South-east
SGR	Soft Gamma-ray Repeater
SN	Supernova
SNR	Supernova Remnant
SVM	Service Module
SW	South-west
TeV	Tera electron-Volt
TSS	Telescope Sun Shield
VOD	Venting and Outgassing Doors
W	West
WD	White Dwarf
XMM	X-ray Multi-Mirror
yr	year

LIST OF FIGURES

LIST OF TABLES

ABSTRACT

AN X-RAY STUDY OF SHELL-TYPE GALACTIC SUPERNOVA REMNANTS

Nergis CESUR

Department of Physics

MSc. Thesis

Adviser: Assist. Prof. Dr. Murat HÜDAVERDİ

Co-adviser: Assoc. Prof. Dr. Aytap SEZER

Observations of synchrotron X-rays can be a useful tool to investigate cosmic-ray acceleration in young supernova remnants (SNRs). Spectral fitting of the synchrotron radiation in an X-ray band gives us information about the cosmic-ray acceleration mechanism. Recently, Galactic cosmic-ray acceleration is widely attributed to SNR shocks. In this thesis, making contribution to search for PeVatron energies (10^{15} eV) in SNRs and understand the physical process of this energies were aimed. In line with this objective, the results of the systematic X-ray spectral study of small scale structures on the shocks of five well-known Galactic shell-type SNRs (Cas A, RCW 86, RX J1713.7−3946, SN 1006 and Vela Jr.) with *Chandra* and *XMM-Newton* X-ray Observatories were presented. The non-thermal X-ray emission and its contribution with the cosmic-ray acceleration properties with these five SNRs were investigated by extracting the X-ray spectra from different targeted regions. All regions have synchrotron X-ray emission, and the maximum energy of accelerated electrons ($E_{max,e}$) and protons ($E_{max,p}$) were estimated for each target, which led to search for PeVatron energies. In accordance with this purpose, due to calculate the reliable values, the estimated background subtracted spectra of each SNR were modelled with using a combination of thermal and non-thermal spectral models (e.g., *srcut*, *power-law*, *cutoffpl*, *vnei*).

Analysing extended sources, such as SNRs, with accurately modelled background emission is important since it might be effective on spectral results. Environment of an SNR (e.g., its location on the Galactic latitude) is a key point for background estimation, which could be represented by components such as Cosmic X-ray Background, Galactic Ridge X-ray Emission or Foreground Emission. Such parameters

as roll-off frequency or cut-off energy requires accurately modelled background spectra to estimate the reliable values of $E_{max,e}$ and $E_{max,p}$. Thus, the background modelling is a first point to concentrate upon deriving the maximum energies of the particles in this thesis.

Briefly stated, analysis of the background spectrum is critical due to characterise the synchrotron emission with sensitive parameters. This process is required to calculate the shock velocities, roll-off frequencies, especially the maximum energies of accelerated particles where they make PeVatron energies searchable. In addition, during these calculations, the magnetic field value is critical while selecting the proper synchrotron models. In this study, it has claimed that the SNRs Cas A and Vela Jr. contain targeted emission regions which have PeVatron energies. But this results require more reliable analysis methods since current synchrotron models need to be retested and improve. Under these circumstances, all these mentioned parameters could be searched reliably with background modelling method, which is suitable for the purpose of determining the non-thermal characteristics of the shell-type SNRs.

Key words: Supernova remnants, interstellar medium, X-ray astronomy, cosmic-rays

ÖZET

KABUK TİPİ GALAKTİK SÜPERNOVA KALINTILARININ X-IŞINI ANALİZİ

Nergis CESUR

Fizik Anabilim Dalı

Yüksek Lisans Tezi

Tez Danışmanı: Dr. Öğretim Üyesi Murat HÜDAVERDİ

Eş Danışman: Doç. Dr. Aytap SEZER

Sinkrotron X-ışınlarının gözlemi, genç süpernova kalıntılarında (SNK) kozmik ışın ivmelendirilmesini incelemek için kullanışlı bir yoldur. Sinkrotron ışınımının X-ışını bandında tayfsal uyarlaması, bize kozmik ışın ivmelendirme mekanizması hakkında bilgi verir. Son zamanlarda, Galaktik kozmik ışın ivmelenmesinin nedeni genel olarak SNK şoklarına dayandırılmıştır. Bu tezde, SNK'lerde PeVatron (10^{15} eV) enerjilerinin aranmasına ve bu enerjilerin fiziksel süreçlerinin anlaşılmasına katkı sağlanması amaçlanmıştır. Bu amaç doğrultusunda, *XMM-Newton* ve *Chandra* Gözlem Uyduları kullanılarak tanınmış Galaktik kabuk tipi SNK'lerin (Cas A, RCW 86, RX J1713.7−3946, SN 1006 ve Vela Jr.) şoklarında X-ışını bandını kullanarak küçük ölçekli alanların sistematik olarak tayfsal incelenmesinin sonuçları sunulmaktadır. Bu beş kalıntıda hedeflenen farklı alanlardan gelen X-ışını spektrumu elde edilerek, termal olmayan X-ışını emisyonunun kozmik ışını ivmelendirme özellikleriyle olan ilgisi araştırılmıştır. Hedeflenen bütün alanlar, sinkrotron X-ışını emisyonuna sahiptir ve her bir hedef için PeVatron enerjilerini araştırmayı sağlayan ivmelendirilmiş elektronların ve protonların maksimum enerjileri ($E_{max,e}$ ve $E_{max,p}$) hesaplanmıştır. Bu amaç doğrultusunda, her bir SNK'nin arkaplan ışıması çıkarılmış spektrumu, termal ve termal olmayan spektral modellerin (örn.; *srcut*, *power-law*, *cutoffpl*, *vnei*) kombinasyonları kullanılarak modellenmiştir.

SNK'ler gibi yaygın nesneleri, tayfsal sonuçlar üzerinde etkili olabileceğinden doğru bir şekilde modellenmiş arkaplan ışımasıyla analiz etmek önemlidir. SNK'nin bulunduğu ortam (örn., Galaktik düzlemdeki konumu), Kozmik X-ışını Arkaplanı, Galaktik Düzlem X-ışını Emisyonu ya da Önalan Işıması gibi ışımaların değerlendirmesinde kilit noktasıdır. Azalma frekansı veya kesme enerjisi gibi parametreler, $E_{max,e}$ ve $E_{max,p}$'nin güvenilir değerlerini hesaplamak için doğru bir şekilde modellenmiş arkaplan spektrumlarını gerektirir. Bu yüzden, parçacıkların maksimum enerjilerini doğru olarak hesaplayabilmek için bu tezde arkaplan ışıması modellemesi ilk olarak yoğunlaşılan noktadır.

Kısaca belirtmek gerekirse, hassas parametrelerle sinkrotron emisyonunun karakterize edilebilmesi için arkaplan ışımasının spektrumunun analizi kritik bir noktadır. Bu işlem, şok hızlarını, kesme frekanslarını ve özellikle PeVatron enerjilerini aranabilir hâle getirmek için hızlandırılmış parçacıkların maksimum enerjilerini hesaplamak için gereklidir. Buna ek olarak, bu hesaplamalar sırasında, uygun sinkrotron modellerini seçebilmek için manyetik alan değeri önemli bir yere sahiptir. Bu çalışmada, Cas A ve Vela Jr. kalıntılarının PeVatron enerjisine sahip emisyon bölgeleri içerdikleri bulunmuştur. Ancak, mevcut sinkrotron modellerinin tekrar test edilmesi ve iyileştirilmesi gerektiğinden bu sonuçlar daha güvenilir analiz yöntemleri gerektirmektedir. Bu koşullar altında, bahsedilen parametrelerin hepsi, kabuk tipi SNK'lerin termal olmayan özelliklerini belirlenmesine yönelik arkaplan ışıması modelleme yöntemi ile güvenilir şekilde aranabilir.

Anahtar Kelimeler: Supernova kalıntıları, yıldızlararası ortam, X-ışını astronomisi, kozmik ışınlar

CHAPTER 1

INTRODUCTION

1.1 Literature Review

Supernova (SN) explosion of a star at the end of its life cycle is a fundamental process to the evolution of the Universe. Because of the extremely large explosion energy (~10^{51} erg) releasing into the interstellar medium (ISM), an SN is extremely luminous and sometimes outshines a whole galaxy. The remnant might be sustainable over tens of thousands of years.

SNe trigger the formation of newer generations of stars as producing heavy elements with rapid neutron capture in the expanding ejecta merging with the ISM, and enrich the chemical content in the disturbed interstellar clouds. They also affect the distribution of gas, and dust in the host galaxy, and the chemical content of the ISM, and create most of the elements necessary for life. Hence, the evolution of the galaxy may be affected. Besides, SN explosions provide a unique laboratory to study the subjects that cannot be observable elsewhere in the universe. Hereby, they serve for development of the Physics with their uniqueness. Because, they are key to understand the nucleosynthesis of heavy elements, galactic chemical evolution, the physics and the formation of the stars, composition and conditions of ISM, chemical evolution of the universe, and so on. It is evinced with the most of the studies that, their interaction with ISM are also sources of most of the galactic cosmic-rays (CRs), through the powerful shock waves produced by the explosion that heating and ionizing the material encountered.

Currently, about 294 Supernova Remnants (SNRs) are found in the Milky Way. These Galactic SNRs are mostly located near the galactic plane and suffer from large interstellar extinction. The great majority of these remnants are shell-type SNRs (~79%).

Appearance of the shell-type SNRs is characterized by a limb-brightened shell formed by the ejecta from the SN explosion and afterwards also by the swept up surrounding material. Also, in the young SNRs, the dense emission may be caused by the reverse shock (RS) that has not reached the inner parts of the ejecta yet. Eventually, limb-brightening provides the shell-like appearance, which is bright both in X-ray and radio band, but not bright in the emission associated with central regions of the remnant. SNRs are not studied in X-rays, but also in radio, infrared, optical and gamma-ray bands.

The young SNRs are the most critical targets, because of emitting in high energy X-rays and γ-rays, and hence, they accelerate the CRs close to the "knee" energy. Additionally, young shell-type SNRs can be very useful tools to investigate electron acceleration via synchrotron X-rays up to 10 − 100 TeV. From radio to X-ray band, spectral fitting of the synchrotron emission is informative about the acceleration mechanism that correlated with “the roll-off frequency” (ν_{roll}) of the spectrum which is required for the calculating “the maximum energy of the electrons” ($E_{max,e}$), and “the maximum energy of the protons” ($E_{max,p}$). Thus, with the given values of magnetic field (B) and the SNR age (t_{age}), $E_{max,p}$ can be estimated ($E_{max,e}^{2}\,B^{2}\,t_{age}$).

“Magnetic field amplification” in shocks enlighten the problem of the particles between the “knee” and the “ankle” energies, and responsible for the detection of TeV γ-ray emission from plenty of young shell-type SNRs accelerating charged particles to energies of order 10^{14} eV. Hence, SNRs are almost the only sources satisfactorily explain the CR production rate in the Galaxy.

Recently, there is no specific observational evidence of a Galactic *PeVatron* in the high-energy astronomy. It remains a major problem in this field. In our Galaxy Milk Way, Galactic CRs reach energies of at least a few Peta-electron-Volts (PeV; 1 PeV = 10^{15} eV), and this suggest that our Galaxy *the Milky Way* contains PeV accelerators (*PeVatrons*). Inferred from recent gamma-ray observations, Galactic accelerators can accelerate particle to tens of TeV (1 TeV = 10^{12} electron Volts) in the theory.

1.2 Objective of the Thesis

In this thesis, X-ray emission is considered, and possible characteristics of the shell-type remnants Cas A, RCW 86, RX J1713.7−3946, SN 1006, and Vela Jr. are discussed with a comparative approach for each SNR. Also, in recent years, importance of background estimation in spectral analysis have been emphasising in plenty of studies. It is a key process to understand the effect of SNR environment (e.g., distance from the galactic latitude) to the its X-ray emission spectrum. Considering this, the X-ray spectra of the SNRs with and without this approach for a comparable study with both available *XMM-Newton* and *Chandra* observations for each SNR are analysed. On the other hand, beside this analysis methods, CR acceleration up to PeVatron energies is searched for the SNRs.

1.3 Hypothesis

As mentioned before, CRs are being investigated at the present and their origin still remains unclarified. In the studies from the literature, the questions like these are waiting for being answered: "How the CRs are accelerated efficiently in the young SNRs (age ~2000 yr)?"; "How is the relationship between CR acceleration and surrounding material of SNRs?"; "If SNRs accelerate CRs, how high in energy can they accelerate particles?"; "What is the diffusion regime?"; "How do CRs escape from SNRs and diffuse in the ISM?"

CRs are thought to be accelerated in the SNR shocks, and via this mechanism, although it has been proved theoretically that they can be reach the PeV energies, there is no observational evidence.

Synchrotron emission from SNRs has been getting modelled, and that way with obtaining the roll-off frequency, maximum energy of electrons and protons have been calculated. Up to the present, PeVatron could not be found albeit plenty of the studies.

Maximum energy of electrons and protons depends on three parameters (roll-off frequency, magnetic field and shock speed). Thus, reliable calculation of these three parameters can light up the open ended questions about the searching PeVatrons in young shell-type SNRs.

In this thesis, searching PeVatrons in young shell-type SNRs is considered. Therefore, particular importance to background modelling is given for estimating the sensitive parameters of roll-off frequency.

CHAPTER 2

SUPERNOVA AND SUPERNOVA REMNANTS

2.1 Supernovae (SNe) Overview

In 1934, Walter Baade and Fritz Zwicky first found and coined the term “Supernova” (SN) as an extremely bright class of stellar outbursts called “nova”. Nova is a different process than supernova, which is a result of explosion spreads across the surface of a white dwarf (WD) accreting mass from a companion star. On the other hand, SN is explosion of the collapsing the entire star, which as a final stage of the evolution of it when the outward pressure of the WD can no longer withstand the inward gravitational pressure due to the mass of the star that reaches Chandrasekhar limit (1.44 $M_{\odot}$). With a kinetic energy typically reaches ~10^{51} erg, SN explosions are among the most energetic events in a whole galaxy which nucleosyntheses heavy elements, and ejects them into the interstellar medium that affects as a result with its kinematics, composition, and structure formation [1], [2], [3].

Two major categories of SNe are identified observationally from their light curves and optical spectra: Type I and Type II. Emission lines of heavy elements are dominant in the spectra of Type I SNe, while hydrogen Balmer lines are dominant in spectra of Type II SNe [4], [5], [6], [7]. Light curves of Type I and Type II are given in Figure 2.1 [8].

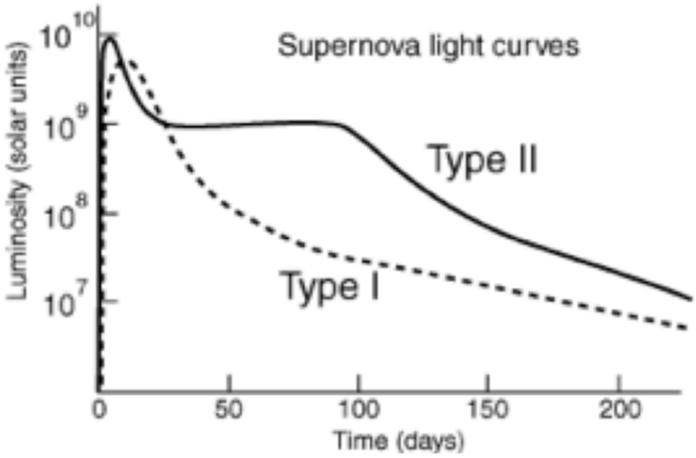

As seen in the figure, Type I SNe reach maximum luminosity in a short time and after one week with this stability, their luminosity begins to decline [9]. On the other hand, Type II SNe show a characteristic rise to a peak brightness, then maintain their stability followed by a decline in the luminosity [8].

Figure 2.1 Light curves of Type I and Type II.

Type I SNe essentially classified into three subclasses Types Ia, Ib, Ic, and they appear both elliptical and spiral galaxies. Types Ib and Ic contain few hydrogen emission, and they only appear in the galaxies which are in the process of high rate of star formation [8], [10]. Also, Type Ib SNe contain helium in their spectrum, while Type Ic SNe do not [3]. Type II SNe contain hydrogen Balmer lines in their spectrum [10] and sub-divided into two classes as Type II-Plateau (II-P) and Type II-Linear (II-L), depending on the shape of their light curves (Figure 2.2) [8]. The light curve of Type II-P SNe have distinctive flat stretch shape (plateau) during the decline for about 100 days before fading, representing a period, where the luminosity decays at a slower rate and most common type of core-collapse (CC) SNe [11]. By contrast, Type II-L SNe show a steady (linear) decline following the maximum brightness [12]. There is also Type IIb SNe, a class between Type Ib and Type II. Their spectra would identify them as Type II, but at late times their spectra evolve into Type Ib spectra [11].

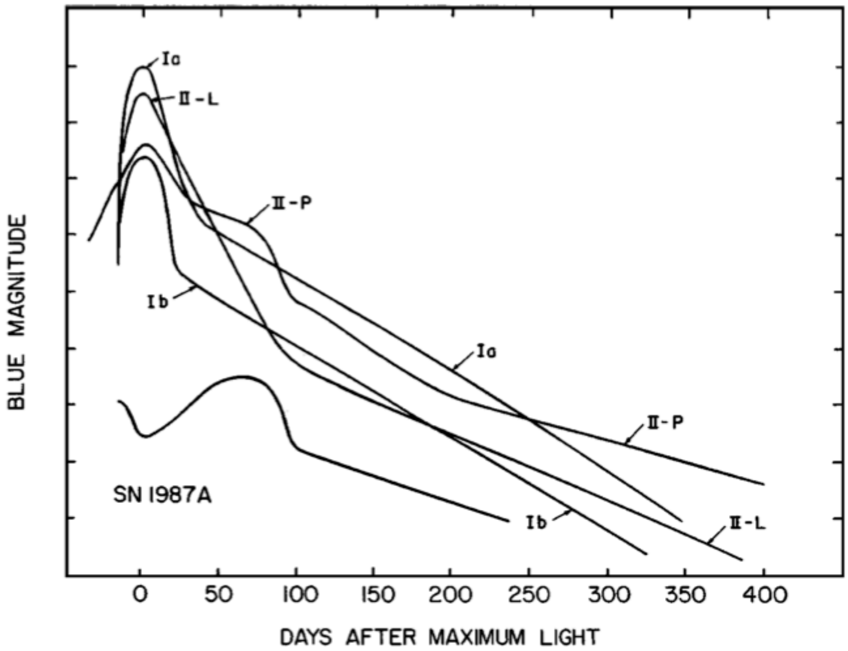

Figure 2.2 Schematic light curves for Type Ia, Ib, II-L, II-P and SN 1987A [13].

Also, Type II SNe only appear in the starburst galaxies, hence, this suggests Types Ib, Ic and Type II belong in the same category. With this approach, SNe also classified into a “CC SNe” (Type II and Type Ib/Ic) results by the collapse of a stellar core at the deaths of the massive stars, and a thermonuclear runaway of WDs (Type Ia), and 80% of Type I SNe include Ia SNe [8], [10].

2.2 Classification of SNe

2.2.1 Type Ia Supernovae (SNe Ia)

The basics of Type Ia SNe theory is under plenty of assumptions, and some of them are tough to prove because of observational information issues belong to the evolution of the progenitor system at a time after the actual explosion, so inevitably the details of the explosion mechanism are obtained indirectly [14].

Type Ia SNe, differ from CC of the massive stars [10] with the explosion energy originates from explosive nuclear burning, are widely agreed that originate from thermonuclear explosions of C/O WD stars [11], [14].

A C/O WD’s mass close to the Chandrasekhar limit, is very likely to be Type Ia progenitors, which is the mass limit of stability of the WD, since WD’s high density makes it ideal for nuclear fusion. Despite the trigger mechanism of this process is not well known, explosion is expected eventually when nuclear reaction in the core is triggered, even the Fermi pressure of the degenerate electrons stabilises WD against gravitational collapse. So, it is reasonable that C/O WDs have to accrete matter, in order to reach the Chandrasekhar limit in an interacting binary system. This argument comes with other subjects for the progenitor systems: double degenerate systems (two WDs), or single degenerate systems (WDs with either a main sequence star or an evolved companion) [11], [14].

Single degenerate systems are the end phases of evolution of low-mass ($<8M_\odot$), and intermediate-mass ($4M_\odot<M<9M_\odot$) stars. It is a mechanism that a long-lasting stable mass accretion from a giant star to a C/O WD in their binary system, as a required process, where WDs are generally formed much below the Chandrasekhar mass. In the first instance, C/O material is accreted directly, in the latter scenario H or He-rich matter is accumulated on top of the C/O WD, and burns hydrostatically into C and O. As a following step, its core is compressed, WD reaches the $1.4M_\odot$ limit, internal temperature and pressure become high enough to fuse carbon in the WD's core, immediately. This reaction releases enough energy to cause explosion that obliterates the star [10].

The other alternative mechanism is double degenerate system which is the merger of two C/O WDs in a binary system [10], [15], [16]. This system creates an object with mass greater than the $1.4M_\odot$, in which carbon fusion is then started, and the carbon burning spreads through the central region [10], [17]. The result is not explosion of the star, but it changes into an O-Ne-Mg WD. Consequentially, this mechanism cannot be affirmed to be an appropriate model suitable for Type Ia SN explosion [10].

Three models are proposed today for thermonuclear explosion, according to the way of the reproduction of carbon burning process: detonation, deflagration, and delayed detonation models [11].

The detonation models predict that once a detonation is triggered the carbon burning produces the shock wave which expands outward at supersonic velocities moving through, and burns the entire star, and thus, causes the explosive nucleosynthesis due the compression, and heating of the plasma by the shock wave. Another prediction is that nearly all of the existing WD matter is ultimately transformed into iron-group elements ($\sim0.6M_\odot$). Nevertheless, detonation models do not provide enough energy to generate a strong shock wave, theoretically [10], [18].

The deflagration models assume nuclear fusion in the burning front by the convective heat transport that interfuses unburnt material into the hot burning zone, and its shock speed is slower than the local sound speed [10], [11]. Based on this model, the observed light curve and the spectrum of Type Ia SN explained successfully by Nomoto et al. [18], who calculated the nucleosynthesis in a C/O WD [14].

The delayed detonation, or deflagration detonation transition (DDT) models [19], which are the currently most popular models for Type Ia SNe, assume that the shock speed reaches supersonic velocities by transition from explosion which starts as a deflagration to detonation wave burning the remainder of the WD into intermediate mass elements (IMEs) [10], [11].

2.2.2 Core-Collapse SNe (SNe II and Ib/Ic)

Type Ia SNe are end of low-mass ($<8M_{\odot}$) stars in the binary systems as discussed above, while as a final stage of their life cycle SNe II and Ib/Ic are results by the collapse of a stellar core of the stars with main sequence masses more massive than $\sim 8\ M_{\odot} - 10M_{\odot}$ [6], [10], [11]. At the beginning of their lives, H atoms in their stellar core is fused into He atoms. This process releases thermal energy that heats the core of the star and gives rise outward pressure gradient force that sustains layers of the star against collapse. This process is known as "hydrostatic equilibrium" or "hydrostatic balance". Since these stars have limited hydrogen in their cores, eventually, the helium will be exhausted, the nuclear burning cycle will continue, and thus, the fusion starts to slow down, source of heat that supports the core against gravity decreases, and so, the gravity causes the core of the star contract [2]. The contracting continues at the end of the He-burning stage, until the temperature becomes high enough to ignite He into C (He-burning/triple-alpha process), Ne and Mg (C-burning), O (Ne-burning) and Si-group elements (O-burning), Fe-group elements (Si-burning). Meanwhile, the pressure increases in the hydrogen layer surrounding the core. Consequently, the core of the star has a structure like "onion layers" (Figure 2.3) as increasingly heavier atomic nuclei build up at the centre. Iron-group core (mostly ^{56}Fe) is the end point of the fusion process, because it is the most stable form of nuclear matter, and there can be no longer generable nuclear energy by fusing it to any heavier element [11].

Figure 2.3 Schematic structure of nuclear reactions in the stellar core just before core collapse (not to scale) [20].

The matter is electron degenerate when density is high enough, temperature and pressure are low enough, then there is no source of heat to balance the gravity. Accumulated Fe in the central core is sustained by the degenerate pressure of electrons, and is at the Chandrasekhar mass limit.

Thereafter, two types instability occurs: i) Electron capturing by heavy atoms divest the core from main pressure source. The pressure is obtained by electrons but decreasing electrons cause to accelerate the collapsing. ii) Due to the substantially degenerated gas, the temperature increase is inevitable [20]. On the other hand, the mass of the core continuously increases as the Si layer burns into Fe, internal temperature increases to ~10^{10} K which causes to decay of ^{56}Fe,

$$^{56}\mathrm{Fe} + \gamma \rightarrow 13\,^{4}\mathrm{He} + 4\mathrm{n} - 124.4\ \mathrm{MeV} \tag{2.1}$$

and the energy to be absorbed, reducing the pressure. This is an endothermic reaction where 2 MeV energy is gained per nucleon. In connection with continuing contracting, the temperature re-increases. Also, the increasing is not enough to retain the collapsing. The contracting lasts until the photons split the He nuclei into protons and neutrons. As this reaction needs a larger energy absorption (~6 MeV per nucleon), the core contracts further. Density reaches a sufficient level for free electrons to capture free protons and turns them into neutrons [20],

$$\mathrm{p} + \mathrm{e} \rightarrow \mathrm{n} + \nu_e \tag{2.2}$$

This process not only absorbs energy; it also reduces the number of particles in the environment. Thus, the pressure drops further because of the disappearance of the core-supporting electrons and the contraction of the core continues. Finally, the neutron gas is degenerated. This occurs at a nuclear matter density of about 10^{15} g/cm^3 and provides the pressure to stop the collapse. Thus, the homogeneous neutron matter occurs which is supported by the nuclear force [6], [20]. Eventually, the core exceeds its equilibrium position and bounces. As the supersonically infalling matters bounce off the high density iron core, a shock wave is formed. The core pushes this shock wave outwards with energy ~10^{51} erg and the star has thrown out its outer layers in the form of an explosion. Finally, this process causes nuclear fused material to get ejected outwards. The collapsing core remains a proto-neutron star, and for the star has a mass >30$M_\odot$, remains a black hole (the stars with a mass > 40$M_\odot$ − 50$M_\odot$ are thought to collapse directly to black hole without mass loss) [21]. The explosion injects heavy elements into interstellar medium, and abundances created are affected by the mass of the collapsing star. Most part of the gravitational energy released (~10^{53} erg) is in the form of diffusing neutrinos [2].

Since the SN explosion is in an interstellar medium, the gas bumped by this explosion sweeps the gas in the atmosphere, and these two gases combine to cause the mass of the SNR to increase. The expanding matter ejected from the star during the explosion has often a kinetic energy ~10^{50} − 10^{51} erg. The bumped gas gives a portion of the kinetic energy swept. When expanding by ~1 pc, the mass of the swept gas is about 1$M_\odot$. This enlargement gas is called “supernova remnant” [2], [22].

When the Type I SN occurs, the interstellar mass thrown is <1$M_\odot$ and the velocity at the beginning of the gas (at SN observation) can be up to 15 – 20 × 10^3 km s^{-1}. In the case of Type II SN, mass up to 2 $M_\odot$ − 3$M_\odot$ can be thrown and the gas velocity is close to 5.000 − 10.000 km s^{-1} on average [20].

Type Ib/Ic SNe are differentiated from Type II SNe, since massive stars that have a mass ≥30 lose their hydrogen envelopes (and possibly part of their He envelopes) by stellar winds, or by mass transfer. They are also fainter than the SN Type Ia. Type Ib SN occurs in spiral galaxies, and star forming regions, and while hydrogen is absence, O lines dominate their spectra. Wolf-Rayet stars are possible progenitors of these types of SNe [2].

2.3 Review of Supernova Remnants

Understanding the evolution of an SNR provides information about its nucleosynthesis, nature, surrounding environment, and the physics behind.

The temperature of the gas in the shell of the SNR is more than a million degrees. For this reason, SNRs are X-ray sources. When the residue grows to an average of $2 - 5$ pc, the speed will be more than a few thousand km h^{-1}. The time to reach this radius depends on the density of the ISM, and the initial kinetic energy of the SN. It takes a few centuries to a thousand years for such an expansion [6].

As the age of the SNR increases, its mass increases, and reaches several thousand solar masses. The speed is reduced by several hundred km h^{-1}. The temperature decreases as it is directly dependent on the speed of the shock wave, but it is always close to a million degrees [22].

2.3.1 Classification of Supernova Remnants

There are four types of SNRs based on their radio morphology: Shell, composite, filled centre (or plerionic-type), and mixed-morphology. If the large part of the SNR radiation comes from its shell, it is shell-type. If the SNR has pulsar inside, and the radiation is coming from the pulse, it is plerionic-type. If radiation comes from both, it is composite type [22], [23]. If the emission arises mostly from swept-up interstellar material, and the X-ray emission is primarily thermal, then, it is mixed-morphology type [49]. Despite, they have similar morphology between radio and X-ray, they have different X-ray nature. Currently, 294 SNRs found in our Galaxy, 79% are of shell type; 12% are of composite type; 5% are of plerionic-type, and the remaining remnants are not clear from current observations, or they are not suitable into any of the conventional types [24]. The reasonable classification is as follows:

2.3.1.1 Shell-Type SNRs

Shell-type SNRs which are characterised by a limb-brightened morphology in radio and X-rays, result from the expansion of the shock wave of the SN explosion that sweeps through the interstellar medium, thus, a shell of shock heated plasma is created. This shell engulfs the gas and bounded by a bright limb at the edge [11], [31]. Typical examples of shell-type SNRs are Cassiopeia A (G111.7-2.1), Tycho's SNR

(G120.1+1.4), Kepler's SNR (G4.5+6.8) and also, these shell-type SNRs show synchrotron radiation in X-rays, which are SN 1006 (G327.6+14.6), and RX J1713.7−3946 (G347.3-00.5) (Figure 2.4).

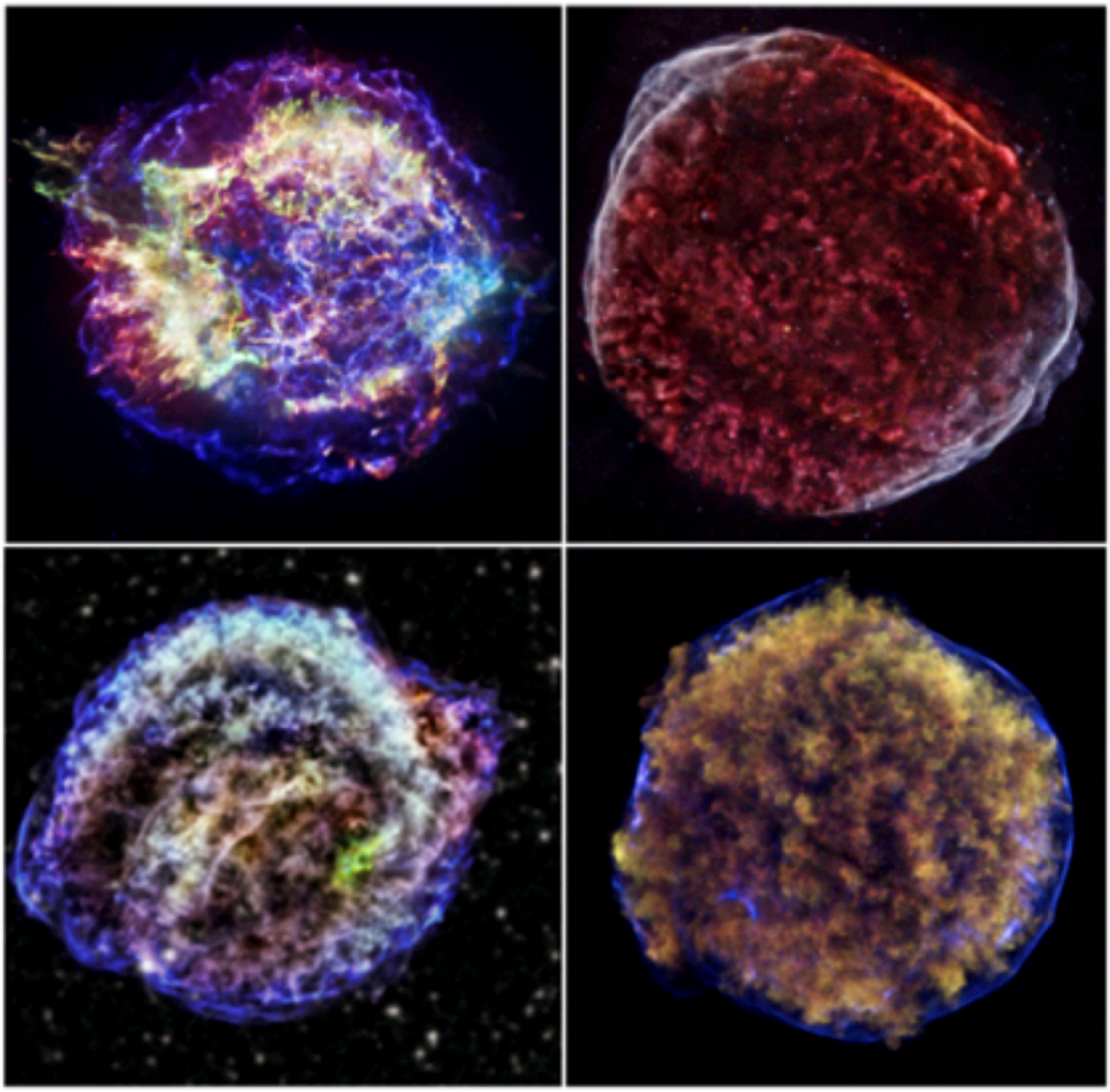

From top left to bottom right: Three colour X-ray image of Cassiopeia A, 8.91 arcmin across, colour codes are Red: 0.5 – 1.5 keV; Green: 1.5 – 2.5; Blue: 4.0 – 6.0 keV. Three colour X-ray image of SN 1006, 34 arcmin across. X-ray and optical composite image of Kepler's SNR, 12 arcmin across, colour codes are X-ray: Red, Green, Blue; Optical: Grayscale. Three colour X-ray image of Tycho's SNR, 10 arcmin across, X-ray colour codes are Red: 1.6 – 2.0 keV; Green: 2.2 – 2.6 keV; Blue: 4 – 6 keV.

Figure 2.4 Typical examples of shell-type SNRs. (Image credits: NASA/CXC)

The loss-limited process mechanism of the shell-type SNR, which is thought to be mainly synchrotron radiation with the hardest ones are in the X-ray energy band, suggests electron acceleration at the blast wave is caused by the ejection of SN [32]. Energy loss of these electrons through radiation,

$$\frac{dE}{dr} = -\frac{4}{3}\,\sigma_T c\,\left(\frac{E}{mc^2}\right)^2 \frac{B_\perp^2}{8\pi} \quad (2.3)$$

where σ_T and $B_\perp^2$ are the electron Thomson cross-section, and magnetic field perpendicular to the particle orbit, respectively. The synchrotron energy loss time (τ_{sync}) is can be described as,

$$\tau_{sync} = (1250\ \text{yr})\ (E_e/1\ \text{TeV})^{-1}\ (B/100\ \mu\text{G})^{-2} \quad (2.4)$$

The times longer than τ_{sync}, the high-energy electrons implied before, cannot radiate energy anymore, due to their limited emission around the shock regions [32].

2.3.1.2 Plerionic-Type SNRs

The name “plerion” originates from the ancient Greek word “pleres” (π λ η ρ η s) which means “filled”. Their name also typified by the Crab nebula (‘Crab-like SNRs’), since their non-thermal (NT) emission mostly originates from the neutron star associated with the remnant, as in the Crab nebula which is powered by the pulsar B0531+21 [11], [33]. Typical examples of plerionic-type SNRs except Crab are IGR J11014−6103, SXP 1062, and G292.0+1.8 (Figure 2.5). The pulsating neutron star may not be located at the centre or at the brightest part of the SNR [29].

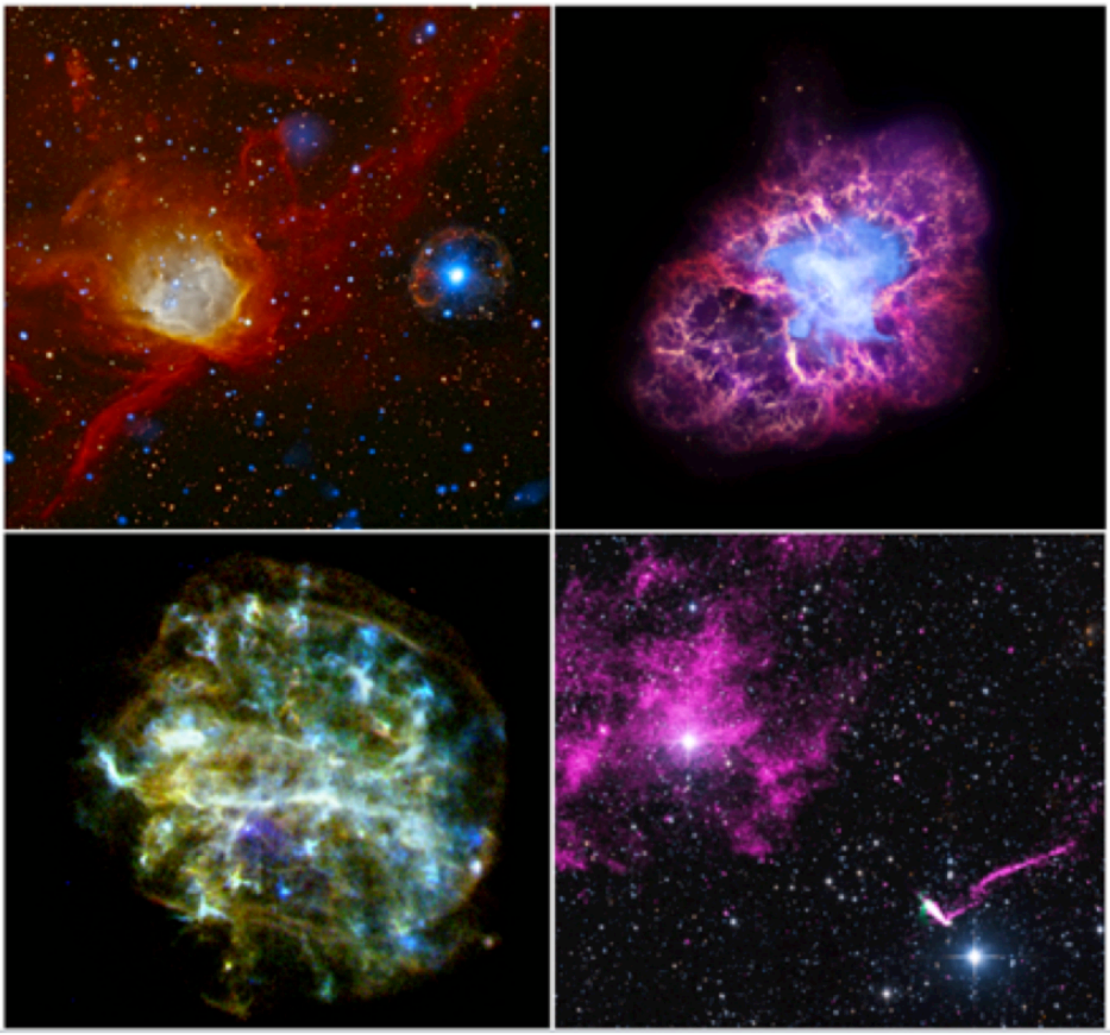

From top left to bottom right: X-ray and optical composite image of SXP 1062, 14 arcmin across, colour codes are X-ray: Blue; Optical: Red; Green. X-ray, infrared and optical composite image of the Crab Nebula, 5 arcmin across, colour codes are X-ray: Blue; Optical: Red-Yellow; Infrared: Purple. *Chandra* X-ray image of G292.0+1.8, 9 arcmin across, colour codes is intensity. X-ray, radio and optical composite image of IGR J11014-6103, 22 arcmin across, colour codes are X-ray: Pink; Radio: Green; Optical: Red, Green, Blue.

Figure 2.5 Typical examples of plerionic-type SNRs. (Image credits: NASA/CXC)

This significant “fraction of spin-down energy loss” converted by the pulsar, produces “a wind of relativistic electrons and positrons”, and thus, the NT emission which is a characteristic of a plerion [11], [29]. The kinetic energy of this wind at termination in a shock, is converted into relativistic hot plasma, where the electrons/positrons are accelerated to ultra-relativistic energies with a Lorentz factor of $\sim 10^5 - 10^6$ [11], [29]. Eventually, these accelerated particles emit synchrotron radiation as in a range between the radio and the soft γ-ray band, and inverse Compton (IC) scattering as in a range between soft γ-ray and the TeV band [11].

2.3.1.3 Composite-Type SNRs

Composite-type SNRs have characteristic features of both shell-type components correlated with the supernova blast wave (and/or ejecta), and plerionic-type SNR as a compact engine (a pulsar wind nebula surrounded by a shell) [11], [29] (Figure 2.6). The plerionic structure usually produces a small fraction of NT X-ray nebula nearly centred of the radio emission with an X-ray compact core [34].

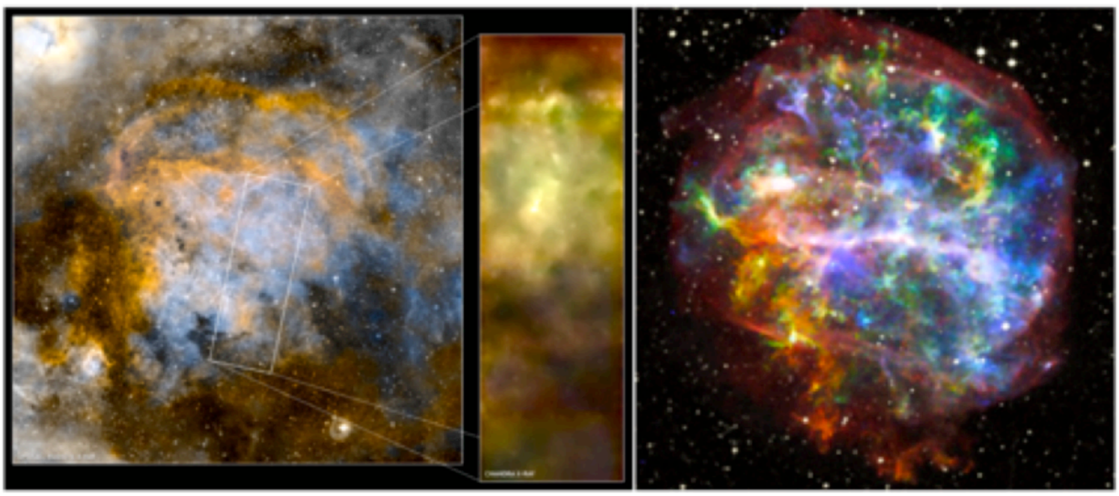

From top left to right: Optical, radio and X-ray composite image of W28, left panel: 54 arcmin across; *Chandra* inset: 24.7 arcmin across, colour codes are *Chandra*: Low-energy X-rays are red, Medium are green, High are blue; ROSAT X-ray: Blue; Optical: Grey; Radio: Orange”. X-ray and optical composite image of G292.0+1.8, 11.5 arcmin per side, colour codes are X-ray: Red (0.580 − 710 & 0.880-950 keV); Orange (0.980 − 1.100 keV), Green (1.280 − 1.430 keV), Blue (1.810 − 2.050 & 2.400 − 2.620 keV); Optical: White

Figure 2.6 Typical examples of composite-type SNRs. (Image credits: NASA/CXC)

Shell-type component has a thermal origin as expected from a shell-type SNRs, while the central plerionic component has two different origins as thermal and plerionic composites (NT) [10].

Thermal composite SNRs have prominent outer shell-like structure in the radio (synchrotron radiation), and thermal X-ray spectrum with diffuse X-ray emission in central regions, as depending on which part of the electromagnetic spectrum observed, and they are also called mixed-morphology SNRs [10], [35], [37]. Despite plerionic composites (they are also called NT composites) appear Crab-like at both radio and X-ray wavebands, they show shell like structures where X-ray spectral lines are observed nearby the shell [36].

2.3.1.4 Mixed-Morphology SNRs

Mixed-morphology SNRs, are relatively older SNRs (20,000 yr), and associated with the denser parts of the ISM, are characterized by centrally peaked thermal X-ray emission that not powered by a compact central source, but consisted of thermal emission from a hot plasma, whereas their radio morphology, filling the surface area within the radio boundary, is shell-like structure with little or no evidence for X-ray shells [11], [49].

According to the study of [49], this class of SNRs is distinguished from other classes by their similar morphological characteristics and physical properties, such as their X-ray emission, which is primarily thermal, and their emission originates mostly from not ejecta, arises from swept-up ISM.

Because of CR nuclei interacting with dense gas in the SNR shell, or from escaping CRs interacting with non-shocked parts of molecular clouds, several of mixed-morphology SNRs are also sources of GeV and even TeV γ-ray emission, and further to that the morphology of these SNRs is difficult to explain with standard SNR evolution models [11]. Typical examples of this type of SNRs are W28, W44 and IC 443.

2.3.2 Evolution of Supernova Remnants

2.3.2.1 Free Expansion Phase

The earliest phase of the SNR evolution is free expansion phase continues until deceleration effects of the interstellar gas becomes important, where the ejected stellar materials that preceded by the shock wave created by the explosion, expands outward (more or less homogeneous), sweeps-up ISM through the expansion velocity (~10^4 km/s), which is larger than the speed of sound in the ambient gas (~10 km/s) [1], [2], [30]. In this stage, mass of the ejected stellar materials is greater than the swept-up mass. The velocity for the ejecta (υf_{ree}), the radius (R_{free}) and the age of the SNR (t_{free}) at this stage are given by

$$R_{free} = (\frac{3M_o}{4\pi\rho_0})^{1/3} = 4.6\ (\frac{M_o}{10M_\odot})^{1/3}\ (\frac{n_o}{1cm^{-3}})^{-1/3}\ [pc] \tag{2.5}$$

$$T_{free} = \frac{\sqrt{2R_{free}}}{\upsilon_{free}} = 6.3 \times 10^{10}\ (\frac{E_o}{10^{51}erg})^{-1/2}\ (\frac{M_o}{10M_\odot})^{5/6}\ (\frac{n_o}{1cm^{-3}})^{-1/3}\ [s] \tag{2.6}$$

$$\upsilon f_{ree} = (\frac{2E_0}{M_0})^{1/2} = 3.2 \times 10^{10}\ (\frac{E_o}{10^{51}erg})^{0.5}(\frac{M_o}{10M_\odot})^{-0.5}\ [cm\ s^{-1}] \tag{2.7}$$

where ρ_0 [g/cm^3] and n_0 [cm^{-3}] are the ambient density, and E_0, M_0 and $M_\odot$ are the initial explosion energy, the mass of the ejecta, and the mass of Sun ($M_\odot = 1.9884 \times 10^{30}$ kg), respectively [2]. The mass of the ISM swept-up by the blast wave described as

$$M_{ISM} = 4/3\ \pi R_s^3 \mu m_H n_0 \tag{2.8}$$

where μ, m_H, and n_0 are mean atomic weight with chemical abundance of solar values, mass of hydrogen atom, and hydrogen number density of the ISM, respectively [1]. The temperature of the material in the shell is ~10^7 K, so hard X-rays observed from SNR are expected [30].

2.3.2.2 Adiabatic Expansion Phase (Sedov Phase)

As swept-up ambient mass (M_{ISM}) becomes much larger than the ejecta mass (M_{Ej}), SNR evolution proceed to next stage called adiabatic phase (Sedov phase) and characterised by a strong, non- radiative shock [1], [2], [3]. Then, the radiative cooling is still small compared with the original energy (the initial energy) of the outburst [30].

Because of $M_{ISM} \geq 10M_{Ej}$, the X-ray emission is dominated by the ISM. The reason of this phase so called Sedov Phase, is that this stage of the evolution can be explained as the result for self-similar solution derived by Sedov [25] which means that the structure of the SNR (the mass of the SNR) stays constant as a function of time - zero mass is released into a uniform medium at time t = 0 [3], [25], [30]. This approach means that deviations from these solutions are not expected to be large, where they predict the variations below with time:

$$R_s \propto t^{2/5} \tag{2.9}$$

$$V_s \propto t^{-3/5} \tag{2.10}$$

$$T_s \propto t^{-6/5} \tag{2.11}$$

where R_s, v_s, and T_s are the radius for the expanding shell, the velocity of the blast wave and the mean temperature behind the shock front, respectively [30]. The structural evolution of this phase can be described by using only the expansion energy (E_0), the ambient density (ρ_0) and the Sedov age (t_{sedov}). Thus, R_s, v_s and T_s are given by [1], [2]

$$R_s = 4 \times 10^{19} \left(\frac{t}{10^4\, yr}\right)^{2/5} \left(\frac{E_0}{10^{51}\, erg}\right)^{1/5} \text{[cm]} \tag{2.12}$$

$$T_s = 3 \times 10^{6} \left(\frac{t}{10^4\, yr}\right)^{-6/5} \left(\frac{E_0}{10^{51}\, erg}\right)^{2/5} \left(\frac{n_o}{1cm^{-3}}\right)^{-2/5} \text{[K]} \tag{2.13}$$

$$\upsilon f_{ree} = \left(\frac{dR_s}{dt}\right) = 5 \times 10^{7} \left(\frac{t}{10^4\, yr}\right)^{-3/5} \left(\frac{E_0}{10^{51}\, erg}\right)^{1/5} \left(\frac{n_o}{1cm^{-3}}\right)^{-1/5} \text{[cm]} \tag{2.14}$$

T_s and n_0 can be determined by X-ray spectrum of the SNR, and R_s can be determined observationally if the distance to the SNR is a known parameter. Also, the age of the SNR (t) and the explosion energy (E) can be derived according to the equations (2.12) and (2.13) [1].

This phase continues until it becomes invalid for the radiative cooling process, which lasts 10,000−20,000 yr. About 70% of the initial explosion energy is converted into thermal energy of the swept-up ISM, until the end of this phase [1], [2], [10]. The temperature of the material in the shell is now likely in the range $1 - 10 \times 10^6$ K [30].

2.3.2.3 Radiative Cooling Phase (Snow-plough Phase)

As the total energy contained in the SNR is no longer conserved, SNR enters radiative cooling phase of its evolution. At this moment, the shock velocity is decelerated down to ~200 kms^{-1} [2], [10], [26]. According to [50] and [51] the age (t_{cool}), radius (R_{cool}), and expansion velocity (V_{cool}) at the begging in this stage are given by [2]

$$T_{cool} = 2.7 \times 10^4 \left(\frac{E_0}{10^{51}\, erg}\right)^{0.34} \left(\frac{n_o}{1cm^{-3}}\right)^{-0.52} [\mathrm{yr}] \tag{2.15}$$

$$R_{cool} = 20 \left(\frac{E_0}{10^{51}\, erg}\right)^{0.295} [\mathrm{pc}] \tag{2.16}$$

$$\upsilon_{free} = 277 \left(\frac{E_0}{10^{51}\, erg}\right)^{0.0554} \left(\frac{n_o}{1cm^{-3}}\right)^{-0.111} [\mathrm{km\ s^{-1}}] \tag{2.17}$$

At this point, since the pressure in the shell becomes lower as the temperature decreases, the swept-up ambient medium is compressed further into a forming thin shell, and cool more rapidly. While the interior gas expands adiabatically, and is still hot, its pressure pushes the thin shell through the ambient medium, sweeps up the surrounding ISM like a snow-plough, according to PV^{γ} = constant (where P is the mean pressure, V is the volume of the internal gas, γ is the specific heat ratio = C_p/C_V, and the value of γ is 5/3 for the non-relativistic single atomic gas) [1], [2]. Then, the time-dependent parameters of the shell, which are radius (R_s) and the velocity (ν_s) are described as [27]

$$R_s \sim t^{2/7} \tag{2.18}$$

$$\upsilon_s \sim t^{-5/7} \tag{2.19}$$

At the last stage, which is called "momentum conservation" or "pressure-driven" snow-plough phase [28], "radiative energy losses" are important [11], the pressure in the interior is to be comparable to the pressure of the ISM as the interior cools [1], [3], [29]. There will be no force acting on the shell of the SNR − so momentum is conserved, and the cool shell continues to sweep up the interstellar gas with a constant radial momentum (where M_s is the mass of the shell, and ν_s is the time-dependent velocity) [1], [2], [3]

$$M_s\nu_s = 4\pi/3 R_s^3 \rho_0\, dR_S/dt = \text{constant} \tag{2.20}$$

with the time dependence of

$R_s \sim t^{1/4}$ (2.21)

2.3.2.4 Disappearance Phase

The phase where the SNR loses its identity and merges into the local ISM, called "disappearance phase" which starts when the expansion velocity becomes comparable to proper velocity of sound in the surrounding ISM (10 km/s) [30]. After SN explosion, the age of the remnant in this phase is larger than ~10^6 yr [1]. The merging SNR becomes indistinguishable from the ISM due to Rayleigh-Taylor instabilities between ejecta dominated and swept-up matter, and leaves a cavity behind with a higher temperature than the surroundings [10], [29].

2.4 Cosmic-Ray Acceleration Process in the Galactic SNRs

2.4.1 Cosmic-rays

CRs are among of the main components of the high energy particles (the others are Cosmic Microwave Background, far-infrared radiation from dust, stellar lights, thermal kinematic energy, turbulent kinematic energy, magnetic energy, and so on) [38]. They were discovered by Victor Hess in 1912. Their energy density is $\varepsilon \sim 1$ eV cm^{-3}. It is known that although they have an effect on the heating and the ionisation of the ISM, the topic that Galactic CRs acceleration (E < 3 × 10^{15} eV) still remains unclear. They are "charged" and "very energetic particles". They contain mainly protons, with ~10% of Helium, and 1% of electrons, and little amount of the ionised nuclei. This richness in heavy elements means acceleration site has rich metals, like SNRs [39]. They are significantly overabundant in Li, Be, F, Sc, Ti, V, Mn, and Ni. These elements are not produced in the stellar evolution. Thus, the idea is that they are produced by "the inelastic interaction" of the CRs with the interstellar matter [39].

The travel distance of CRs is estimated to be ~1000 kpc with a "ISM density" of 1 cm^{-3}. This value is longer than the size of our Galaxy. Hence, CRs are confined by the galactic magnetic field. Besides, supernova expansion energy of ~10^{51} ergs can be explain energy supply of CRs [39].

SNRs are considered to explain the CR production rate in the Milky Way, for a long time. CRs are the candidates for the acceleration site below the "knee" energy. The energy spectrum of CRs is almost power-law (PL) like and featureless. (Figure 2.7).

Two turn-over in the spectra can be seen clearly: one is E ~ 3 × 10^{15} eV ("knee") and the other is E ~ 3 × 10^{18} eV ("ankle"). The particles at the energy "ankle", are thought to be accelerated in the extragalactic sources, such as active galactic nuclei. Recently, their energy spectra is known to extend beyond 10^{20} eV. However, it is a big question that how CRs are accelerated, since nobody had any observational evidence.

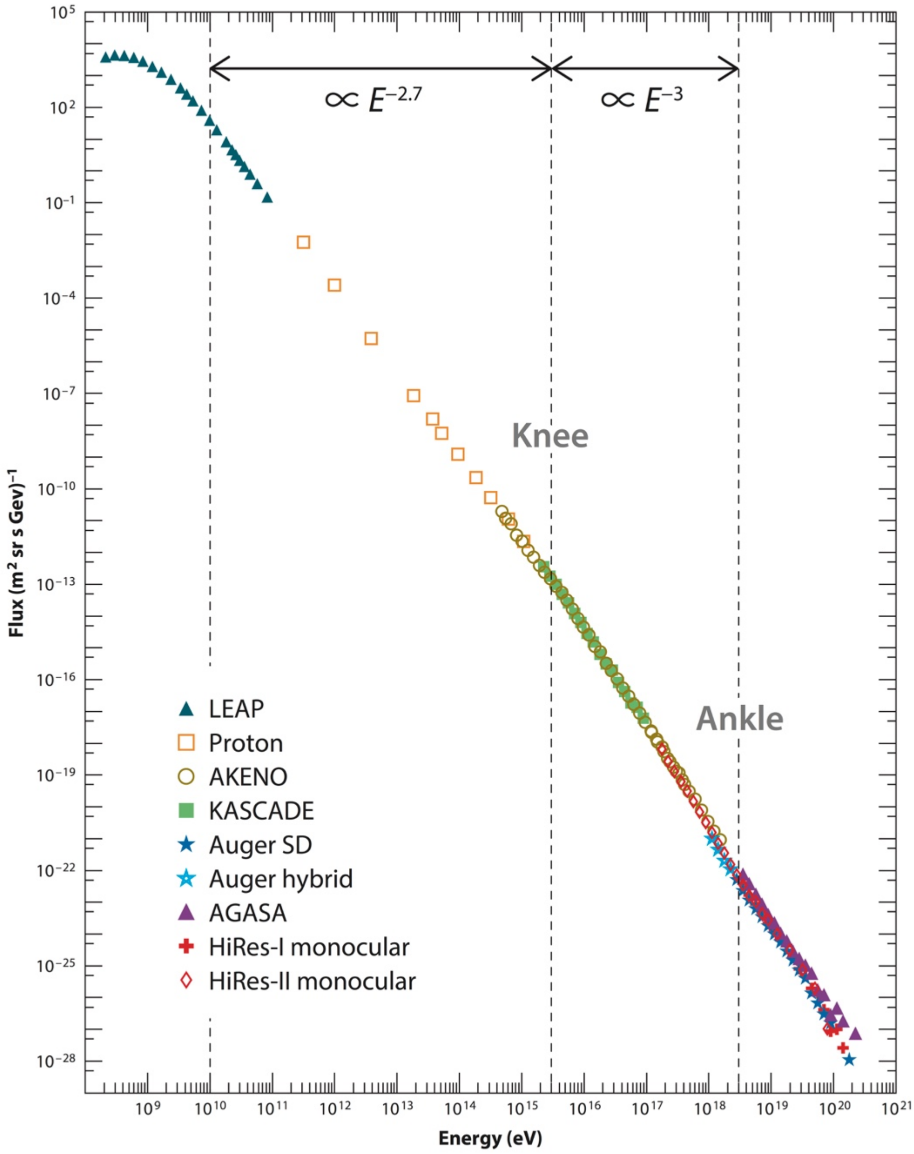

Figure 2.7 The energy spectrum of cosmic-rays [40].

2.4.2 Diffusive Shock Acceleration (DSA)

A huge amount of kinetic energy is essential to explain the acceleration of the CRs. Thus, the collision-less shock waves caused by supersonic plasma flows are satisfying this need [38]. DSA or the first order Fermi acceleration in the SNRs adapted at the shock wave is considered to explain the efficient particle acceleration and the CRs [39]. Because, it naturally anticipates the energy spectrum of the accelerated particles as a PL $\propto E^{-q}$, whose spectral index is $q = \frac{r+2}{r-1}$, depends on the compression ratio (r). In other words, the observed CR spectrum is expected as a PL shape with an index of a ~2($dN/dE \sim E^{-2}$) [39].

The turbulence of the magnetic field is a scattering substance, because, cosmic plasmas are generally quite thin, and also a collision rate of particles is few. Thus, while investigating the particle acceleration mechanism, collision-less shock wave must be considered [39].

CHAPTER 3

RADIATIVE PROCESS

3.1 Photoelectric Absorption

The photoelectric absorption process occurs when an atom absorbs a photon above the cut-off frequency, and an electron is ejected. In interstellar space, hydrogen ($Z = 1$) is the most abundant atom, and can be ionised by photons with energies above 13.6 eV (with the wavelength $\lambda = 91.2$ nm) [29], [41].

In the transition called the "K edge", for neutral hydrogen atoms, below 13.6 eV, the cross section for the photoelectric effect is zero, at 13.6 eV it moves up to a higher value. This situation refers the inner orbital K shell of electrons ($n = 1$) where they are ejected [41].

Photoelectric absorption cross-section for photons $E_\nu > E_I$ and $h\nu \ll m_e c^2$ is given by

$$\sigma_K = 4\sqrt{2}\sigma_T \alpha^4 Z^5 (m_0 c^2/\nu)^{7/2} \tag{3.1}$$

where E_I is the "electron binding energy", σ_T is the "Thomson cross-section" ($\sigma_T \sim 6.65 \times 10^{-29}$ m^2), and α is "the fine structure constant". Photoelectric absorption cross-section does not depend on Z^5 and $\nu^{-7/2}$.

The fraction of the flux lost due to the absorption of column density is given by

$$dF = -F n_z \sigma_z(E) dl \tag{3.2}$$

where n_z is "the number density of the absorbing element" (Z atomic number), $\sigma_z(E)$ is the cross section of element Z at energy E, and dl is the optical path length over which absorption takes place [29].

For the observed source flux F, in the presence of photoelectric absorption by integrating over the path length is given by

$$F = F_0 \exp(-\sigma_z(E) \int n_z dl) \tag{3.3}$$

Including all elements in the line of sight:

$$F = F_0 \exp\left(\sum_z [\sigma_T(E) \int n_z \frac{n_H}{n_H} dl]\right) \tag{3.4}$$

Hydrogen column density used in this thesis takes the account the effects of interstellar absorption due to Hydrogen is given by Gorenstein [42]

$$N_H = \int n_H dl \ [cm^{-2}] \tag{3.5}$$

where N_H is the number density of the hydrogen.

3.2 Thermal Emission

3.2.1 Collisional Ionisation

When a free electron has a higher kinetic energy (E) than the binding energy (E_I) of the atomic shell ($E > E_I$), and bombards the target electron bounded in an ion, the collisional ionisation occurs. The ionisation cross section is given by

$$\sigma_{c.ioni} = 4.5 \times 10^{-20} \ (N_e \ln(E/EI)/EI) \ [cm^2] \tag{3.6}$$

where N_e is the number of electrons bounded to the shell. According to this formula, when the electron energy is higher, the ionizing power is the less, and when E = I, the cross section at the ionisation threshold energy is zero [1]. Usually, the outer electrons are removed on energetic grounds [29].

Under the effects of the optically-thin, low-density, dust-free, and in steady-state or quasi-steady-state systems, any effect of the radiation field can be ignored, the density effects are negligible, the three-body collisions are irrelevant, and the ionisation balance of the gas is time-independent - only when the atoms are "ionised", and the ionisation and recombination rate are balanced. Hence, the ionisation state of the collisional plasma is called "collisional ionisation equilibrium" (CIE) or "coronal equilibrium" ($kT_z = kT_e'$, kT_z is ionisation temperature and kT_e' is electron temperature of CIE plasma) [29], [43]. When the ionisation rate exceeds the recombination rate where behind the shock front, the plasma "under ionised" because time for the ionisation of the shocked gas to reach the level corresponding to the post shock temperature, is finite, and the atoms are less ionised ($kT_z < kT_e'$) [29], [44]. This situation has been observable in the X-ray spectra of young SNRs [29]. If the atoms are highly ionised, the recombination rate exceeds the ionisation rate, where the recombination tends to fall behind with the cooling of the shocked gas, and thus, the plasma is "over-ionised" ($kT_z > kT_e'$) [29], [44]. This situation has not been observable in the X-ray emission spectrum of the SNRs [29].

3.2.2 Non-equilibrium Ionisation

The plasma system in young SNRs is expected to be in non-equilibrium ionisation (NEI), if it is disturbed by some process such as shock heating, or dynamic (adiabatic) cooling of electrons, the ionisation balance between the ion concentration and the electron temperature has not reached yet, where the characteristic timescale is $\sim 1.5 \times 10^{11} n_0 t_{kyr}$ (in units of s cm^3; n_0 is the Hydrogen ambient density (in units of cm^3), and t_{kyr} is the age of the SNR in units of 1000 yrs) [1], [29].

After the mentioned process, the initial ionisation state of the shocked material is considered to be nearly neutral by the ions losing electrons through collisions with free electrons, until their ionisation states are in equilibrium with the thermal electrons (collisional ionisation equilibrium) [3].

Strongest emission lines are expected from highly ionised ions with less electrons in the outer shells contained by NEI model [45].

3.2.3 Thermal Bremsstrahlung

Bremsstrahlung is to be considered as Compton scattering of the photons of the Coulomb fields of the particles, results from the acceleration of electrons of all energies in Coulomb collisions with other electrons, or with ions and nuclei in the scattering system, where thermal electrons provide the bulk of the thermal continuum ('thermal bremsstrahlung' or 'free-free' emission), and "the electrons with the energies above the shocked thermal energies" contribute the PL spectrum [29], [46], [47]. Measuring the spectrum of the thermal bremsstrahlung can be used in order to estimate the temperature of the gas [29].

The shape of this bremsstrahlung radiation emitted spectrum is given by a total continuum emission per unit time, volume, and frequency by single-speed electrons interacting with many ions as follows

$$P_{\nu}^{ff} = \frac{dW(T,\omega)}{d\omega dV dt} = \frac{2^5 \pi e^6}{3mc^2} \left(\frac{2\pi}{3mk}\right)^{1/2} T^{-1/2} Z^2\, n_e n_i e^{-h\nu/k_B T} \bar{g}_{ff}(T, \nu) \tag{3.7}$$

where m_e is the electron mass, T the plasma temperature, n_e the electron density, n_i the ion density, *Z* the ion charge and $\bar{g}_{ff}$ (T,ν) is the velocity-averaged Gaunt factor [29].

3.3 Radiative Processes of High Energy Cosmic-Rays

3.3.1 Synchrotron Radiation

Relativistic charged particles moving through the trajectories under the effect of the magnetic field, emit electromagnetic radiation in the direction of the motion, with peculiar characteristics, known as "synchrotron radiation" [48]. The indication of this synchrotron nature of radiation, which produces photons up to a few tens of keV, is its NT spectrum [48], [46]. Due to the synchrotron radiation energy losses, the conditions of these charged particles is turned into a PL distribution of the emitted radiation. Polarization is another feature of synchrotron radiation; it has been discovered in the optical spectrum of Crab nebula [48].

It is thought to be that, while the relativistic electrons and magnetic field for plerionic-type SNRs are provided by the powering pulsar, for shell-type SNRs, they are originated from the shocked ISM [29].

The rate of the synchrotron radiation that an electron loses its energy is

$$-\dot{E} = 2\sigma_T c\gamma^2\beta^2 \sin^2\theta (B^2/8\pi) = 1.57 \times 10^{-3} E^2 B^2 \tag{3.8}$$

where $\gamma = E/m_e c^2$ (c is the speed of the light, and m_e is mass of the electron), $\beta = 1-1/\gamma^2$, σ_T is the Thomson cross section, and θ is the electron pitch angle [46].

The approach for numerical form of equation 1.21 is assuming β~1, and averaging over electron pitch angles. The equation (3.8) can be integrated to find the energy (E) of an electron with an initial energy (E_0) radiating in a constant magnetic field for time (t) [46]:

$$E = (E_0^{-1} + 1.57 \times 10^{-3}\, B^2 t)^{-1} \tag{3.9}$$

3.3.2 Inverse Compton Scattering

Relativistic CR electrons scatter low-energy photons or seed photons, such as cosmic microwave background, up to the higher energies via Compton scattering. This process is called "inverse Compton scattering" [38]. The energy of scattered interstellar photon $\varepsilon' = h\nu'$ is

$$\varepsilon' = 4/3\, \gamma^2 \varepsilon_0 \tag{3.10}$$

where $\varepsilon_0 = h\nu$ is the initial energy of the interstellar photon, and γ is the Lorentz factor.

The total power emitted by a single electron via IC scattering is

$$P_{IC} = 4/3\, \sigma_T c \beta^2 \gamma^2 U_{photon} \tag{3.11}$$

where U_{photon} ($= n_{photon}\varepsilon_0$) is the energy density of the seed photons.

3.3.3 π^0-Decay Emission

Photons are main component of CRs. As they collide with other protons in interstellar matter, the high energy protons emit γ-rays via π^0-decay. The decay can be described as:

$$p(CR) + p(ISM) \rightarrow p + p + \pi^0 \tag{3.12}$$

$$\pi^0 \rightarrow 2\gamma \tag{3.13}$$

where p(ISM) and p(CR) are interstellar proton and accelerated CR proton, respectively. Each photon has 67.5 MeV energy and opposite directions each other. On the other hand, energy of photons increases because of π^0 obtain a part of the kinetic energy of CR protons. That mechanism is called "hadronic process" [38].

CHAPTER 4

X-RAY OBSERVATORIES

Currently active X-Ray Observatories, lead us to enter a new era of studying X-ray astrophysics. Brief introduction to these observatories is given, which all the relevant data in this thesis are obtained.

4.1 Chandra Observatory[1]

4.1.1 General Information

Chandra X-ray Observatory (CXO) was launched on 1999. Outline drawing of the observatory is shown in Figure 4.1. It consists of a spacecraft and X-ray telescopes. The spacecraft carries the 'X-ray CCD cameras' (ACIS-I and ACIS-S) on the focal plane of the X-ray telescopes [49].

[1] http://chandra.harvard.edu/about/hardware.html

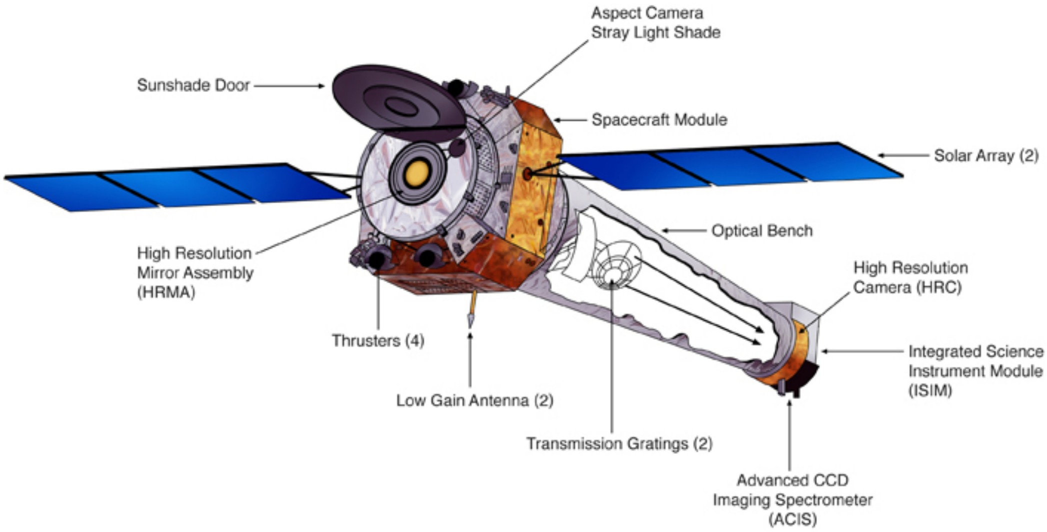

Figure 4.1 *Chandra* interactive features. (Image credit: NGST & NASA/CXC)

Chandra has three major parts:

i) The X-ray telescope.

ii) The science instruments.

iii) The spacecraft.

4.1.2 Technical Description

Chandra has four science instruments to capture the X-rays from astronomical sources. The X-rays are focused by the mirrors to a spot on the focal plane. These instruments capture information about the X-ray emission: time of arrival, energy, position, and number.

X-ray photons penetrate into mirrors because of their high energy. The mirrors have to be aligned nearly parallel to incoming X-rays (Figure 4.2). HRMA allows spatial resolution of better than 0.5″.

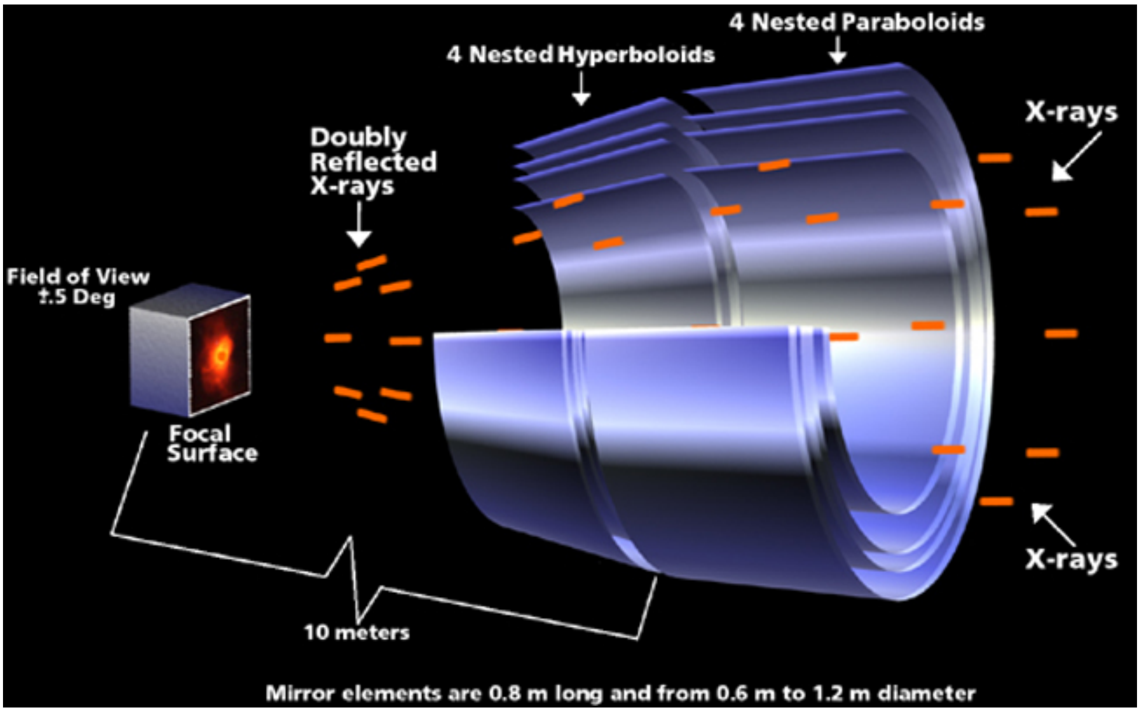

Figure 4.2 The *Chandra* telescope system. (Image Credit: NASA/CXC/D.Berry)

4.1.3 Instruments

The incoming X-ray photons are focused by the mirrors to a spot on the focal plane instruments, which are ACIS and HRC.

The LETG and HETG spectrometers provide detailed information about the X-ray energy. The X-ray emission position is measured by HRC or ACIS, and so the energy can be determined.

4.1.3.1 High Resolution Camera (HRC)

HRC detects X-ray photons reflected from eight mirrors. It can make detailed images as small as one-half an arc second.

HRC has two Micro-Channel Plates (MCP). They each consist of a 10 cm square cluster of 69 million tiny lead-oxide glass tubes. Illustration of HRC can be seen in Figure 4.3.

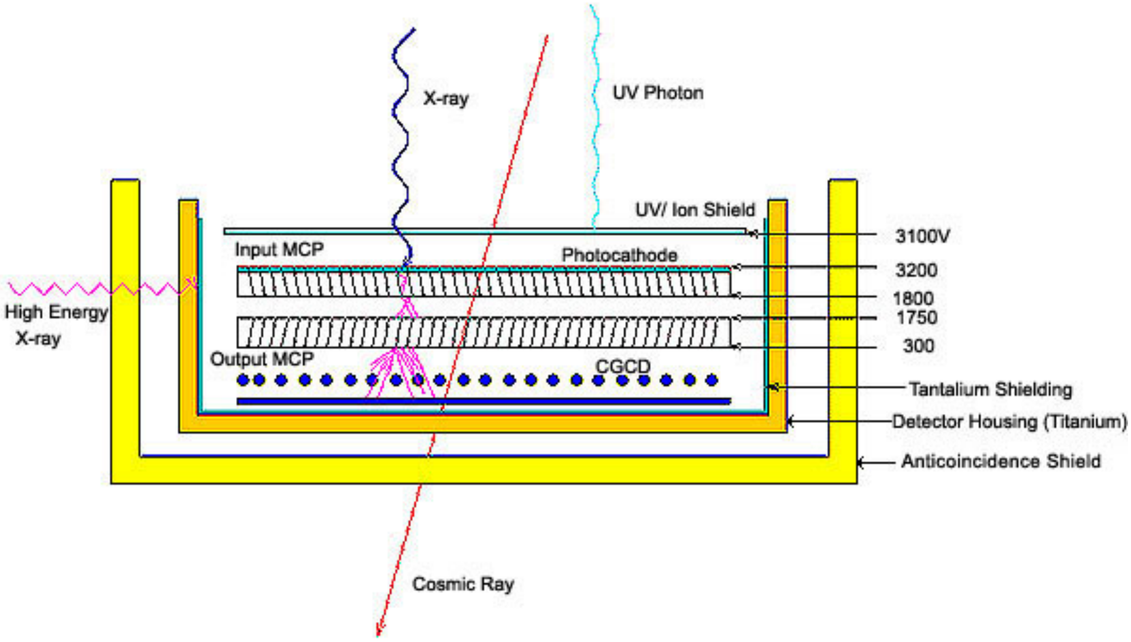

Figure 4.3 High Resolution Camera (HRC) illustration. (Image credit: NASA/CXC)

4.1.3.2 Advanced CCD Imaging Spectrometer (ACIS)

ACIS is one of two focal plane instruments. ACIS consists of ten individual charged coupled devices (CCDs), each of 1024 × 1024 pixels, arranged in two separate arrays. The schematic view of ACIS at the focal plane are shown in Figure 4.4 and 4.5.

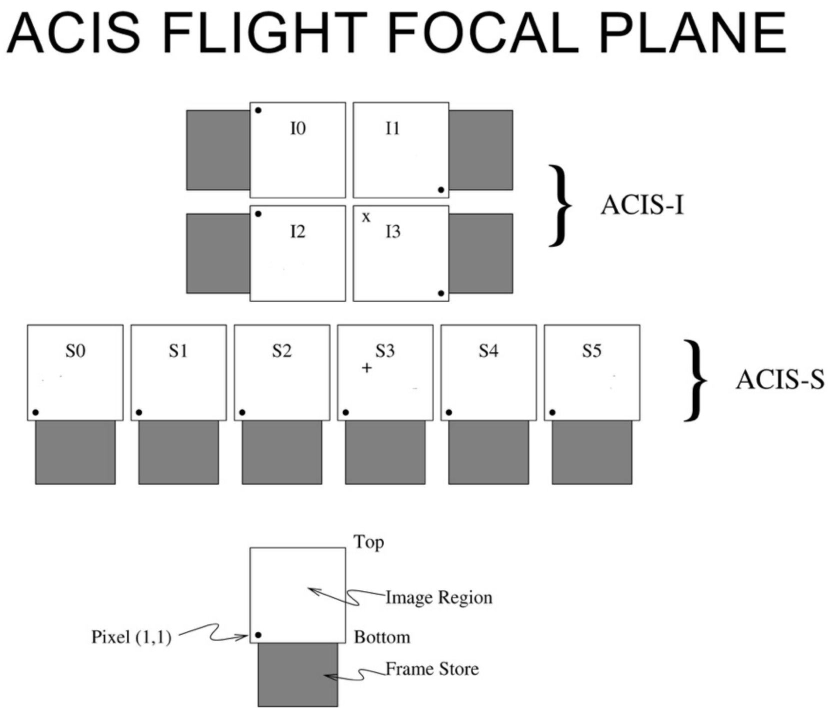

Figure 4.4 Advanced CCD Imaging Spectrometer (ACIS). (Image credit: NASA/CXC)

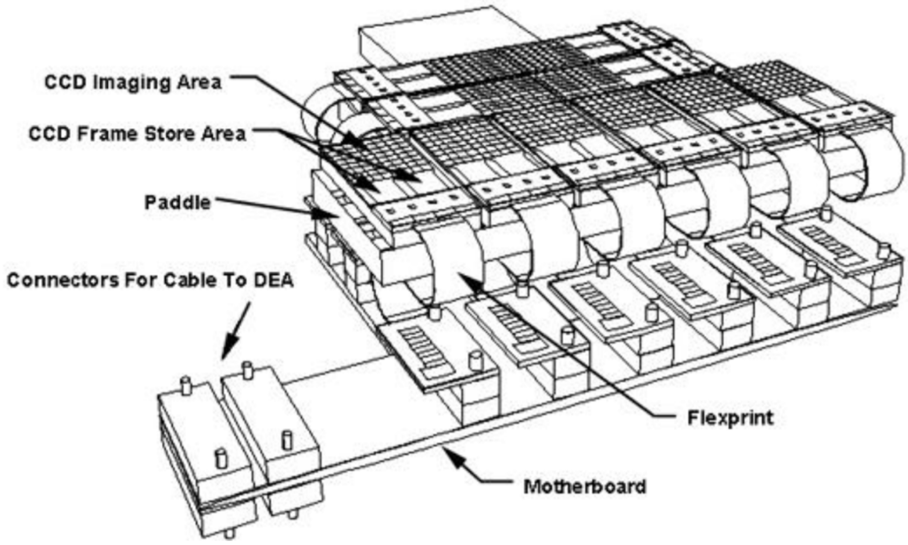

Figure 4.5 CCD imaging spectrometer (ACIS) illustration. (Image credit: NASA/CXC)

Four of the chips were placed in a 2×2 array (ACIS-I) with a $17' \times 17'$ FoV. The other six chips were arranged in a 1×6 array (ACIS-S). The CCDs have been optimized for high detection efficiency, and spatial resolution ($0.5''$ when combined with the HRMA) in the $0.2 - 12$ keV band.

4.1.3.3 The High Resolution Spectrometers

There are two instruments for high resolution spectroscopy: "The High Energy Transmission Grating Spectrometer" (HETGS), and "the Low Energy Transmission Grating Spectrometer" (LETGS).

The LETGS is made of fine wires or bars with a regular spacing of 1 μm. The gratings are mounted onto a toroidal ring structure matched to the *Chandra* mirrors. LETGS covers an energy range of 0.08 − 2 keV.

The HETGS has a period of 0.2 μm for the high-energy gratings; and 0.4 μm for the medium energy gratings. The HETGSs cover an energy range of 0.4 to 10 keV.

4.2 XMM-Newton Observatory[1]

4.2.1 General Information

XMM-Newton is launched by the European Space Agency (ESA). It is composed of four main parts: 'The Focal Plane Assembly' (FPA), 'the Telescope Tube' (TT), 'the Mirror Support Platform' (MSP), 'the Service Module' (SVM) (Figure 4.6).

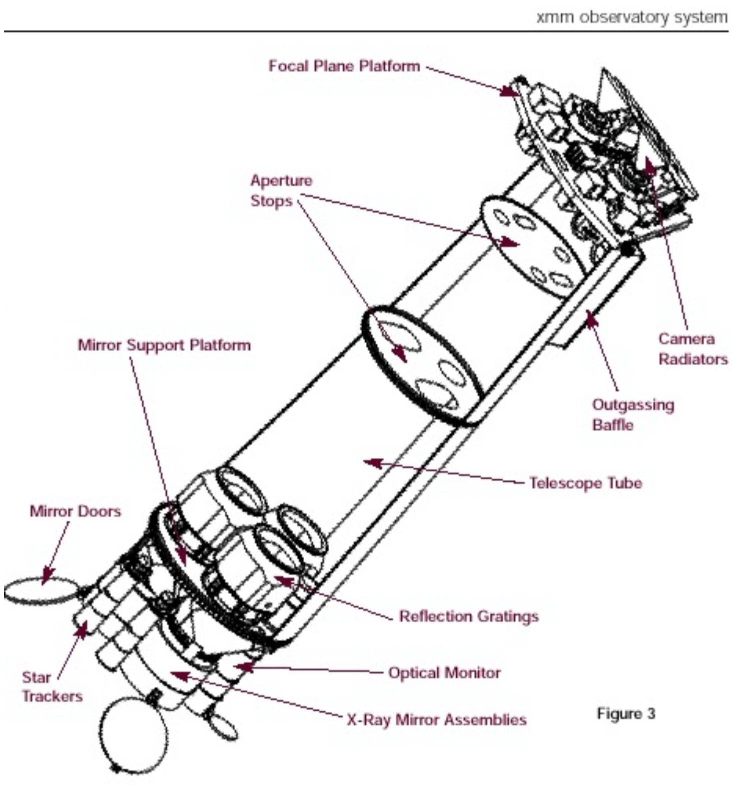

Figure 4.6 *XMM-Newton* observatory system. (Image credit: ESA/XMM-Newton)

[1] https://www.cosmos.esa.int/web/xmm-newton/technical-details-spacecraft

4.2.2 Technical Description

FPA carries the focal-plane instruments: two 'Reflection Grating Spectrometers (RGSs) readout cameras', an EPIC PN and two EPIC MOS detectors, and the data handling and power distribution units for the cameras.

TT provides the relative position between the FPA and the MSP.

MSP, consists of the platform itself, and carries the three mirrors assemblies (mirror modules + entrance and exit baffles + doors + two RGS grating boxes), the Optical Monitor (OM) and the two star-trackers.

SVM carries the spacecraft subsystems.

Each of *XMM-Newton* telescopes consists of the mirror assembly door, the entrance baffle, the X-ray baffle, the Mirror Module, an electron deflector, in two of the telescopes, the Reflection Grating Array, and the exit baffle (Figure 4.7).

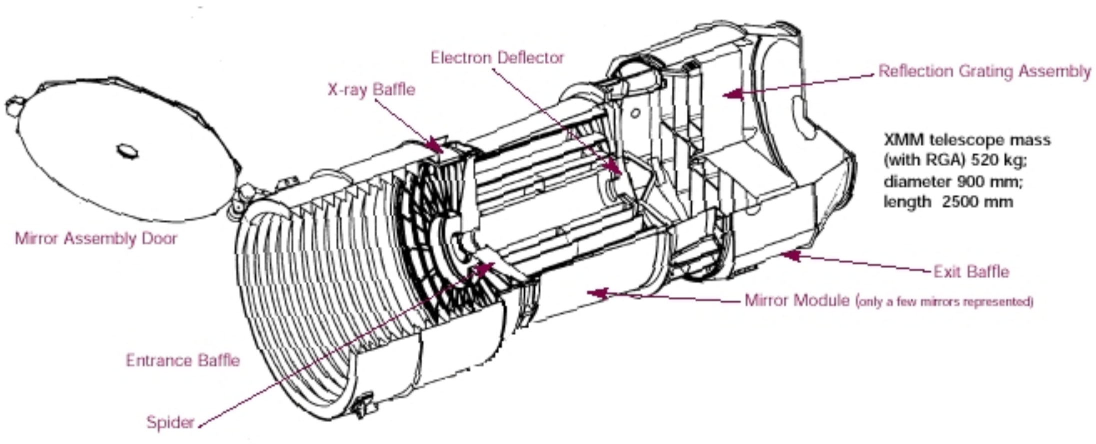

Figure 4.7 *XMM-Newton* telescope configuration. (Image credit: ESA/XMM-Newton)

4.2.3 Instruments

XMM-Newton spacecraft carries a set of three X-ray CCD cameras - European Photon Imaging Camera (EPIC). Two of them are MOS (Metal Oxide Semi-conductor) CCD arrays. They are equipped with the gratings of the Reflection Grating Spectrometers (RGS). The third X-ray telescope has the EPIC instrument at the focus of the telescope uses pn CCDs. They all operate in photon counting mode.

Another module on board of *XMM-Newton* is the EPIC Radiation Monitor (ERM). The function of the ERM is the detection of the particle environment information for the correct operation of the CCDs.

4.2.3.1 MOS CCDs

There are seven front-illuminated CCDs in the focal plane of each MOS camera (Figure 4.8). The imaging area is ~ 2.5 × 2.5 cm, so that a mosaic of seven covers the focal plane equivalent to 28.4 arcmin. The imaging section has 40 micron square, pixels; one pixel covers 1.1 × 1.1 arcsec on the FoV.

The MOS has a useful quantum efficiency in the energy range 0.2 − 10 keV. For MOS, one of the three electrodes has been enlarged to occupy a greater fraction of each pixel. High energy efficiency is defined by the resistivity of the epitaxial silicon (around 400 Ohm cm). The actual mean depletion of the flight CCDs is between 35 to 40 microns.

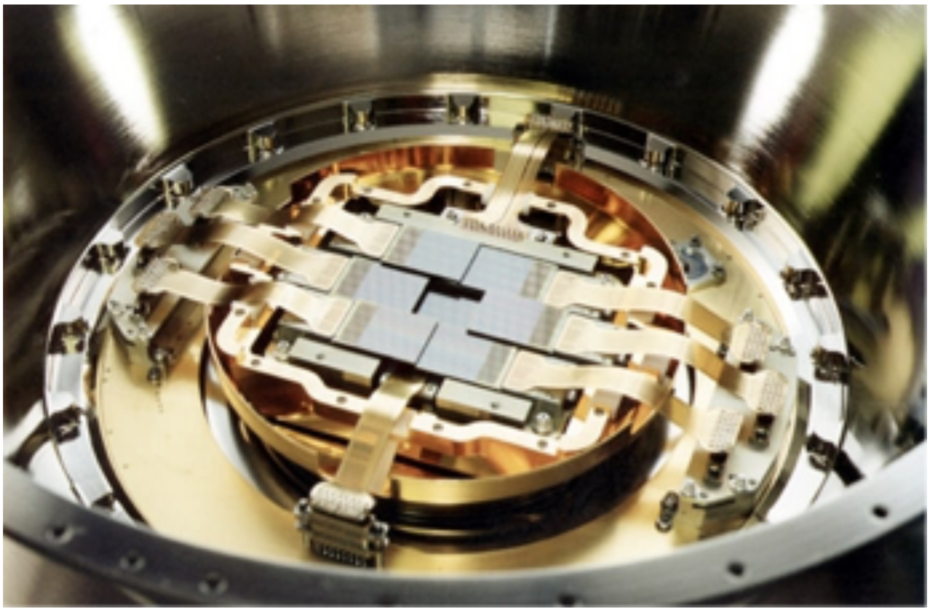

Figure 4.8 The CCDs of one of the MOS cameras in the cryostat. (Image credit: ESA/XMM-Newton)

4.2.3.2 PN CCDs

In the pn camera, FoV is realized by the monolithic fabrication of twelve 3 × 1 cm pn-CCDs (Figure 4.9). The pn array was designed with a pixel size of 150 × 150 microns (4.1 arcsec) with a position resolution of 120 microns. The schematic view (Figure 4.10) shows the concept: X-ray photons hit the detector from the rear side. As X-rays interact with the Si atoms, electrons and holes are generated in numbers proportional to the energy of the incident photon. The positively charged holes move to the negatively biased back side, where they are absorbed. The electrons, captured in the potential wells can be transferred towards the readout nodes upon command.

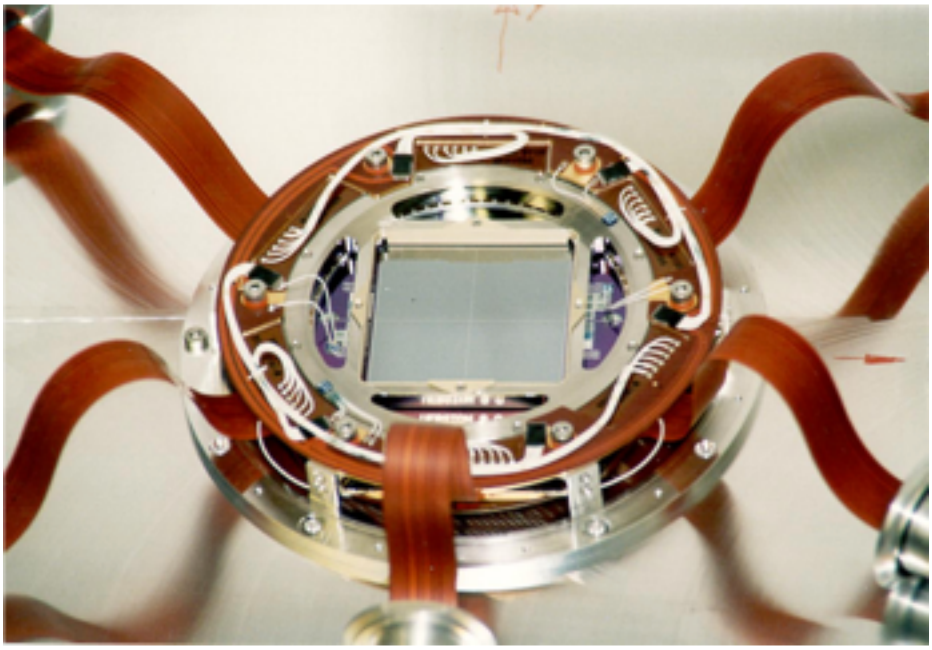

Figure 4.9 The CCDs of the pn camera. (Image Credit: ESA/XMM-Newton)

4.2.3.3 The Reflection Grating Spectrometer (RGS)

The RGS is an array of reflection gratings, deflects X-ray light to a strip of CCD detectors offset from the telescope focal plane. The un-deflected light passes through, and is intercepted by EPIC-MOS. For each X-ray photon, the energy and the position is measured.

4.2.3.4 The Optical/UV Monitor Telescope (XMM-OM)

The XMM-OM (Figure 4.10) is mounted on the mirror support platform the telescope. It provides coverage between 170 nm and 650 nm of 17 arcmin^2 region of the FoV, targets in the X-ray and ultraviolet/optical bands.

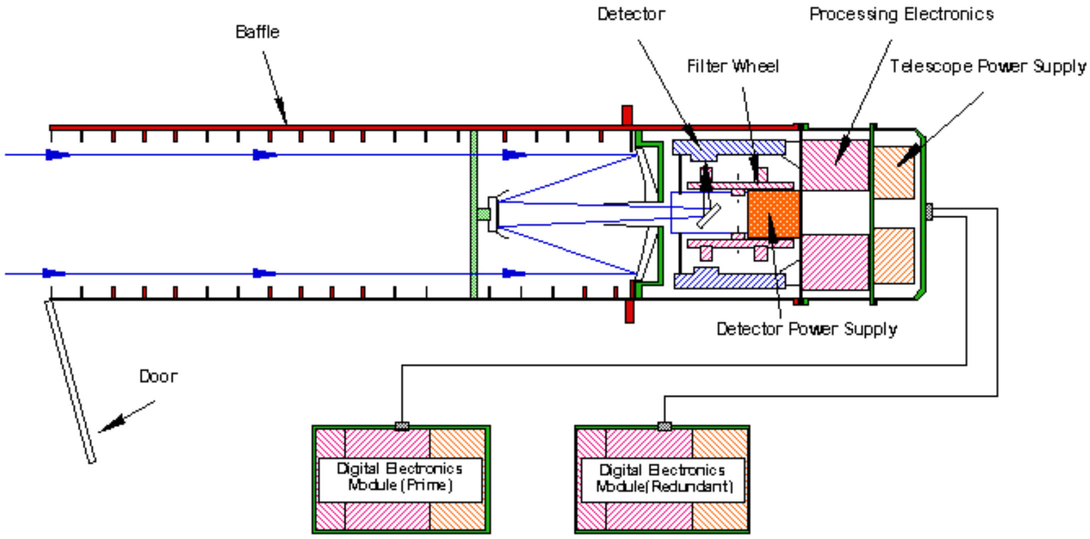

Figure 4.10 A schematic of the XMM-OM. (Image credit: ESA/XMM-Newton)

OM main characteristics are: Two (redundant) Digital Electronics Module, , total coverage between 170 nm and 650 nm of a 17 arcmin square FoV, 2 m long telescope tube, two filter wheels with 11 apertures, one magnifier and two prisms (optical and UV), two (redundant) detectors, 30 cm Ritchey-Chretien telescope, a primary mirror of 0.3 m and a hyperboloid secondary mirror.

CHAPTER 5

ANALYSIS OF THE SNRS

5.1 X-ray Background

Cosmic X-ray Background (CXB): Method of [50] is the most used method for modelling the CXB spectrum which dominates the hard X-ray surface brightness. They obtained a photon index of ~1.41 and surface brightness value 5.41×10^{-15} erg s^{-1} cm^{-2} $arcmin^{-2}$ for 2−10 keV hard band emission (PL) component.

Galactic Ridge X-ray Emission (GRXE): Most of the GRXE has a diffuse origin [51], [52]. GRXE spectrum is hard, contains many emission lines from highly ionised ions of the abundant elements [53]. Since an SNR is located near the Galactic disk, the background is dominated by GRXE. Thus, emission lines are expected from the background spectra with a hard continuum [54]. Generally, GRXE spectra is represented by sum of the high temperature and low-temperature plasmas by CIE model (*APEC* in XSPEC) with a free absorption parameter. The flux of the GRXE depends on the Galactic latitude [54], [55]. Also, it could be called as "Galactic X-ray background emission".

Local Hot Bubble (LHB): An irregular local cavity filled with hot gas (10^6 K) at a reasonable pressure could produce observed "local" X-rays, and shows no absorption by cool interstellar gas, is in CIE and can be modelled by an unabsorbed thermal component (*APEC* in XSPEC) [56].

Galactic Halo (GH): The halo plasma is assumed that it is in CIE, so *APEC* model in XSPEC is used. According to the 0.1–1 keV diffuse soft X-ray background observations, it is a (1–3) × 10^6 K plasma in the halo of the Galaxy [57]. Although the origin of the GH is uncertain, there are two assumptions for the main process: SNdriven outflows from the Galactic disk, and accretion of material from the intergalactic medium (see references in [57]).

Foreground Emission (FE): A low energy emission (≤2 keV) indicates small or no absorption, unrelated to Galactic Center region. Its origin is unknown but thought to be a local Galactic plasma or unresolved dM stars [58]. FE is generally represented by CIE model (*APEC* in XSPEC) with neglected absorption parameter.

In thesis, background components described above are used for the spectral analysis with taking into account the location of the SNRs in the Galactic plane, spectral shapes and emission lines (Table 5.1). Under these circumstances, all spectral parameters can be examined reliably with background modelling method, which is suitable for the purpose of determining the thermal or NT characteristics of the SNRs.

Table 5.1 Log of archival observations used in the study for each SNR and the components of the background emission.

SNR	Galactic Coordinates (*l*, *b*)	Observatory	Obs. Id.	Exp. (ks)	Background Components
Cas A	$111\overset{\circ}{.}7347$, $-02\overset{\circ}{.}1296$	*Chandra*	4639	80	CXB GH FE
RCW 86	$315\overset{\circ}{.}0927$, $-02\overset{\circ}{.}3765$	*XMM-Newton*	0504810401	73	CXB FE
RX J1713.7−3946	$347\overset{\circ}{.}2695$, $-00\overset{\circ}{.}2569$	*Chandra*	5561 12671	29 91	CXB GRXE FE
SN 1006	$327\overset{\circ}{.}4109$, $+14\overset{\circ}{.}4674$	*Chandra*	13737 13742 13741 13739 13738	74 80 88 99 101	CXB LHB
Vela Jr.	$266\overset{\circ}{.}2591$, $-01\overset{\circ}{.}2199$	*Chandra*	3846 9123 4414	35 39 40	CXB FE

Under XSPEC, there are several spectral models to employ according to the data and the area of utilisation. There are thermal and NT models in analysis of supernova remnants (e.g., NEI, VNEI, VVNEI, APEC, VAPEC, MEKAL, VMEKAL *(thermal models)*; POWERLAW (PL), PEGPWRLW, BKNPOW, CUT-OFFPL, SRCUT *(NT models)*).

5.2 X-ray Spectral Analysis

In each analysis Heasoft 6.20, CALDB 4.7.2, CIAO 4.9, XMM-SAS 16.0.0, XSPEC 12.9.1, SAOImage DS9 7.5, AtomDB 3.0.9, and the up-to-date versions of the current calibration files (CCFs) were used.

As in the standard procedure by *Chandra* X-ray Center, event list *Chandra* files are gathered by ACIS-S and ACIS-I, reprocessed by using the script *CHANDRA_REPRO* and for restricting the energy ranges and creating the images *DMCOPY* script is used on the event files, respectively. Response Matrix Files (RMFs) and Ancillary Response Files (ARFs) are generated with *SPECEXTRACT* script in CIAO.

For *XMM-Newton* analysis, EPIC-MOS data were used. X-ray photon events corresponding to patterns 0−12 and flag = 0 for MOS1/2, 0−4 and flag = 0 for pn were selected, respectively. *MOS-FILTER* and *PN-FILTER* tasks that included in ESAS package integrated into SAS, were used to identify good time intervals, filter and create new clean event files. After this process, SAS task *EVIGWEIGHT* was used for vignetting-weighted event lists for the EPIC instruments to correct for the effective area variation across the SNR [59]. Spectrum and background files were created with *EVSELECT* task, ARFs with *ARFGEN* task and RMFs with *RMFGEN* task in SAS. The MOS1 CCD6 was damaged by micro meteorite events, thus, it was no longer recording observations, this is where some of the SNR area falls on this CCD[1].

In the spectral analysis with XSPEC, the solar abundances of Wilms et. al (2000) [60] was adopted. All errors were represented by 90% confidence levels.

For all the rims of SNRs, the spectra of the selected sources were fitted with subtracting the non-modelled background spectra (BGD-1). In the next step, the background spectra of the sources were modelled with subtracting the modelled background spectra (BGD-2) for a comparable approach.

Note that, the abbreviations N, S, NW, SE, SW and W represents North, South, North-West, South-East, South-West and West that used for naming the rims.

[1] https://www.cosmos.esa.int/web/xmm-newton/mos1-ccd6

5.2.1 Cassiopeia A

5.2.1.1 Literature

In the *ROSAT* and *Einstein* study of Vink et al. (1998) [61], the overall expansion timescale of Cas A is found to be 501 ± 15 yr, and the results indicate that the SNR is not anymore in the free expansion phase.

Using *Chandra* Observatory, Hughes et al. (2000) [62] mentioned in other studies that high surface brightness knots of the Cas A are compact and they enriched in Si and S.

Utilizing the observation data obtained by *Chandra*, Berendse et al. (2001) [63] concluded that the forward shock (FS) of Cas A appears to be dominated in the continuum above 3 keV by NT emission. They also concluded that the spectrum is dominated by X-ray synchrotron radiation from electrons accelerated by the forward shock.

Utilizing the data obtained by the *Chandra*, Gotthelf et al. (2001) [64] suggested in their study that Cas A is entering the Sedov phase.

Using *BeppoSAX,* observational data Vink et. al (2001) [65] reported detection of the ^{44}Sc nuclear decay lines, associated with the nuclear decay ^{44}Ti. They assumed that 12 – 300 keV continuum is adequately represented by a single power-law, and detected the line emission. They suggested initial ^{44}Ti mass of (0.8 - 2.5) × 10^{-4} $M_{\odot}$ together with the Compton Gamma Ray Observatory/COMPTEL measurement of the ^{44}Ca line.

Utilizing *XMM-Newton* observation, and using NEI model, Willingale et al. (2002) [66] suggest in their study that original explosion of Cas A has possibly axial symmetry due to the largely bi-polar distribution of the Fe-K emission and, to some degree, the Si-K and S-K emission. They found a strong evidence for the nucleosynthesis of Si, S, Ar, Ca elements by explosive Si-burning, and incomplete explosive O-burning. This nucleosynthesis process is caused by the shock heating of these layers in the CC SN, as mentioned in the study. They suggested that because of the CC throwing off material in two opposing clumps, the bulk of the Fe-K emission may arise in two regions. Via analysing of the abundances, they showed that the matter responsible for the line emission is ejecta, caused by the ablating of bullets, not swept up by the shock. They explained the heating mechanism is likely caused by dense bullets with the material pre-heated by the primary shock.

The study of DeLaney, and Rudnick (2003) [67] using *Chandra* data, shows the continuum dominated X-ray filaments located around the edge of the SNR show expansion rates 0.02% − 0.33% yr^{-1}, and they are associated with the FS.

Rothschild and Lingenfelter (2003) [68] suggest in their study that Cas A is possibly in the stage, which the pushback disk has yet to form. They found that the ^{44}Ti yield from the Cas A supernova should be $(1.5 \pm 0.3) \times 10^{-4}$ $M_{\odot}$, assuming a ^{44}Ti half-life of 59.2 ± 0.6 yr, an age of 317 yr, and a distance of 3.4 kpc.

According to the X-ray, optical and radio study of DeLaney et al. (2004) [69] using *Chandra* X-ray Observatory, Hubble Space Telescope, and Very Large Array, X-ray emission from Cas A can be separated into shocked CSM (circumstellar medium) and shocked ejecta. On the other hand, the shocked CSM can be separated into clumpy and diffuse component, too. The shocked ejecta component consists of both Fe- and Si-dominated emission populations associated with optical fast-moving knot (FMK) emission. The clumpy CSM component consists of slow-moving, low energy-enhanced emission, and is analogous to optical quasi-stationary flocculi (QSF) emission. They suggest that the diffuse CSM may be correlated with the continuum-dominated emission from material that swept up by the forward shock. The interior continuum-dominated filaments have chaotic motions which may be explained by an interaction with the absorbing CSM in that region.

In the radioactivity from the decay of ^{44}Ti, study of Motizuki and Kumagai (2004) [70] found that, relatively outer region in the remnant is remarkably affected by the ionisation. In this region, X-ray flux of Fe-K is observed from highly ionised Fe. Since ^{44}Ti is most likely accompanied by this element, Motizuki and Kumagai regard the observed region of X-rays of Fe-K as the region, where ^{44}Ti exists in the SNR.

Using X-ray observations obtained with *Chandra* and *XMM-Newton,* study of Decourchelle (2004) [71] indicated that in the CC SN of Cas A, the FS is located in the front of the contact discontinuity (CD). In the SE section, fingers of ejecta are getting closer to the FS. For Cas A, *Chandra* and *XMM-Newton* data show indications of asymmetry in the explosion of the SN.

A million-second observation of Cas A with *Chandra*, Hwang et al. (2004) [63] showed that the ejecta of the SNR has a bipolar structure. They suggested that this implies the jets were formed by the explosion.

In X-ray proper-motion (PM) measurements of Cas A, using *Chandra* study of DeLaney et al. (2004) [73], revealed that the X-ray emission by the high-resolution PM measurements with the spectral classes, can be separated into three components: i) ejecta component, ii) diffuse CSM component, and iii) clumpy CSM component. The ejecta component it is associated with optical FMK emission, and consists of both Fe- and Si-dominated emission. The clumpy CSM component is represented by the slow-moving LowE-enhanced emission that may be related to optical QSF emission. The diffuse CSM component may be related with the continuum-dominated emission from the material swept up by the FS. Also, they showed that low-density ejecta experience more deceleration, and high-density ejecta experience very little deceleration.

Utilizing *Chandra* HETGS instrument, the derived electron density of X-ray emitting ejecta is found varied 20 − 200 cm^{-3} by Lazendic et al. (2006) [74]. Also, they found that the abundances of Mg, Si, S, and Ca are consistent with O, which is the dominant element in the plasma of Cas A. By derived unambiguous Doppler shifts, they showed that the NW region of the remnant shows having extreme red-shifted values with up to 4000 km s^{-1}, and the SE region shows blue-shifted values reaching up to 2500 km s^{-1}. The most of their selected regions have temperatures ~1 keV through plasma diagnostics, using resolved Si H-like line and Si He-like triplet lines, and this is consistent with reverse-shocked ejecta.

According to the *Chandra* study of Yang et al. (2008) [75], the positive correlations of Si, S and Ca abundances come from explosive O-burning and incomplete Si-burning. Also, positive correlation of Ne and Mg abundances means that they should be the ashes of explosive C/Ne burning. As Si abundance is lower than 3 solar value, the Fe abundance is positively correlated with it. Yang et al. (2008) [75] suggests that the highly Si-enriched ejecta concentrated in the jet and the bright shell are probably a mixture of the explosive O-burning and the incomplete Si-burning products. The rest part might be dominated by the shocked CSM. On the other hand, as another characteristic, Cas A shows rapidly moving oxygen-rich material outside the nominal boundary and this is evidence for two oppositely directed jets. They fitted the spectra with an absorbed two component non-equilibrium ionisation (NEI) model.

Using the *Chandra* observations of the Cas A to localize, characterize, and quantify the NT X-ray emission, it is discussed to be synchrotron radiation in the study of Helder and Vink (2008) [76]. As they mentioned, the NT emission accounts for about 54% of the overall continuum emission in the 4 − 6 keV band. They also concluded that most of the X-ray synchrotron emission comes from the RS in the western part of the SNR, which is the result of a locally higher RS velocity of $v_s \sim 6000$ km s^{-1} than in the eastern part ($v_s \sim 1900$ km s^{-1}).

Using *Chandra* data in their analysis Hwang and Lamin (2009) [77] concluded that Cas A evolved into a small circumstellar bubble with a radius of ~0.2 – 0.3 pc located inside the circumstellar wind. They suggested that diffuse presence of Fe-enriched plasma was probably formed by the complete Si-burning during the explosion, and this situation is likely via alpha-rich freeze-out.

Maeda et al. (2009) [78] found in their *Suzaku* analysis that the X-ray continuum in the 3.4 − 40 keV band is dominated by the NT emission, and they reported the detection of Cr-K_α line at 5.61 keV.

Using the data obtained from *Chandra* observation, Araya et al. (2010) [79] fitted the spectra of the NT filaments in the SNR with PL, and used a model that includes advection, radiative cooling and diffusion of accelerated particles behind the shock. They concluded that "the emission from the inner regions is consistently softer by about 10%, than that from the outer regions". Their analysed data showed that the outer and inner photon indices are the same in all filaments. Their results implied that there is a high level of magnetic turbulence (of the order of tens of μG) in the NT filaments, associated with the FS of the remnant as well as magnetic field amplification. They concluded that this magnetic field varies between the filaments, and is nearly perpendicular to the shock front. They discussed in their study that, these conditions are essential to accelerate CRs, as well. Their analysis of these NT filaments implies that the obliquities are close to 90°, and this result is persistent with the expansion of the remnant in the wind environment produced by the progenitor.

DeLaney et al. (2010) [80] used *Chandra* X-ray Doppler velocity measurements and *Spitzer* Space Telescope's Infrared Spectrograph, and constructed a three-dimensional model of the SNR. According to their findings via ejecta pistons in the plane of the thick disk, a tilted thick disk, and a spherical component to the explosion, they concluded that the morphology of the remnant must be shaped by the SN rather than a CSM interaction. They showed that the Ne/O, and Si-illuminated pistons are bipolar and the Fe-illuminated pistons are not. They argued that the SE Fe ejecta knots are old compared to the the west and north Fe-rich ejecta, which may be a result of an interaction with the CSM structures.

Hainke and Ho (2010) [81] fitted nine years of archival *Chandra* ACIS spectral data with their non-magnetic carbon atmosphere model. They showed that after formation the north shell became thermally relaxed early ~20 yr and ~100 yr, and became isothermal sometime between 1965 and 1980.

Elshamouty et al. (2013) [82] tested decay in the surface temperature of the Cas A. They tested for systematic effects due to the nearby filaments of the SNR, and measured the temperature changes from each detector separately. They concluded of fast cooling of the north shell that can be set by super fluidity of nucleons in the stellar core.

In their *Chandra* study of Cas A, Hwang and Laming (2012) [83] found ^{44}Ti and its decay products are not located in the centre of the SNR, but they have been ejected out into the ejecta via the hydrodynamic instabilities during the SN. Also, they mentioned that north shell of Cas A formed in the explosion, it is likely perpendicular to the NE - SW “jet axis”.

The result of the *Suzaku* study of Maeda et al. (2014) [84] is that the Cr and Fe-K lines appears at the similar band between 5 – 7 keV, which suggest the co-location of these elements in ejecta were heated with the RS.

Utilizing the *Chandra* data, the results of Lee et al. (2014) [85] concluded that the progenitor of Cas A had an initial mass of ~16$M_{\odot}$, and its mass before the explosion was ~5$M_{\odot}$, and the mass lost from the progenitor star is ~11$M_{\odot}$, and a significant amount of the lost via swept-up mass of the RSG wind is ~6$M_{\odot}$, which indicates that the progenitor of the remnant may lost its mass via the RSG wind.

By using *NuSTAR* archival data of Cas A, Grefenstette et al. (2015) [86] showed that the hard X-ray emission from the SNR up to 50 keV can be investigated in two main categories: bright central knots and fainter outer filaments. These categories show different unbroken PL spectra over the 15 – 50 keV. They implied that it is an evidence for two distinct populations of electrons responsible for the central and exterior emission, and argued that the central knots are located in the interior of the remnant. On the other hand, they concluded that there may be both hadronic and leptonic emission mechanisms in the SNR.

5.2.1.2 Background Estimation

The background region data for *Chandra* analysis, extracted from a rectangular source free area of 39.53 arcmin^2 (Figure 5.1) in the same FoV, where the whole SNR source region data a circular area of 28.27 arcmin^2 is excluded from.

Since, a precise background modelling is a critical process to estimate the reliable values of spectral parameters, analysing of the background spectrum is critical due to the characterize the source spectrum. Thus, comparing the results of modelled and non-modelled background subtracted spectra might be a good approach for the goodness of future works. Hence, in this study, for all the spectral analysis, two background estimation methods were used: a background region selected from the same FoV with the spectra was used without modelling method, or the same background region was modelled due to SNR's Galactic location and with the parameters described in the literature.

Cas A is above the Galactic plane ($l = 111^{\circ}.7347$, $b = -02^{\circ}.1296$). Thus, the possible contamination of the GRXE is negligible [87].

The background spectrum of *Chandra* observation of Cas A consists of the CXB, FE, GH_{hot} and GH_{cold} components. The spectrum was fitted with a model of [$Abs_{(CXB)} \times PL_{(CXB)} + apec_{(FE)} + Abs_{(GH)} \times (apec_{(GHhot)} + apec_{(GHcold)})$, where the CXB component parameters were fixed with a (PL) shape at a photon index of 1.41 and a surface brightness of 5.41×10^{-15} erg s^{-1} cm^{-2} arcmin^{-2} as those in [50], and the *APEC* is a CIE plasma model in XSPEC. The second term is FE component which is represented with *APEC*. The third term is with an absorbed 2-CIE model is GH_{hot} and GH_{cold} component. To calculate the absorption parameter, *TBABS* model was used [121], and the hydrogen column density parameter of CXB component was fixed to 0.394×10^{22} cm^{-2} as in the study of [123]. This value was taken from study of [124] and the absorption of GH component is free parameter. The background spectrum is simulated with using the *FAKEIT* command in XSPEC, and subtracted from the source spectra. The best-fit parameters and spectrum of the background are given in the Table 5.2 and Figure 5.2, respectively.

5.2.1.3 Spectral Fitting

Figure 5.1 shows *Chandra* X-ray RGB image of Cas A in the mentioned energy bands in the caption. *Chandra* images are binned with 4″ × 4″, smoothed with a Gaussian kernel of $\sigma = 1''$.

In order to characterize the emission of specific regions, three spectral source regions were extracted from the edge of the SNR (Figure 5.1) with the area of 4.38×10^{-2} arcmin^2, 5.83×10^{-2} arcmin^2 and 5.34×10^{-2} arcmin^2 were selected. They were grouped with a minimum of 75 counts bin^{-1}. The X-ray spectra of selected regions are well represented by the absorbed NT models (*PL* and *SRCUT*) and Gaussian emission lines. The Gaussian line width parameter was fixed to 0 eV. Fitting spectra with *VNEI*, *VVNEI* or any thermal model did not give physically and statistically acceptable values of kT_e and reduced χ^2 values ($\gtrsim$2). Absorbed *PL* model fitting gives three parameters: Absorbing column density N_H, the photon index Γ, and also absorption-corrected X-ray flux $F_{0.5-7keV}$ which is used for adjusting the normalization parameter while fitting with the *SRCUT* model. N_H, Γ and the normalization were set as free parameters. While with the *SRCUT* model, a synchrotron origin for the hard X-ray emission observed from the SNR were assumed, and spectral index (α) value was employed as ~0.77 [29]. Region#1 could not be fitted with the *SRCUT* due to the high reduced chi-square value. Typical X-ray spectra are shown in Figure 5.3, 5.4 and 5.5 and the best-fit parameters for both NT models are shown in Table 5.3 and Table 5.4 for BGD-1 and BGD-2 subtracted spectra, respectively.

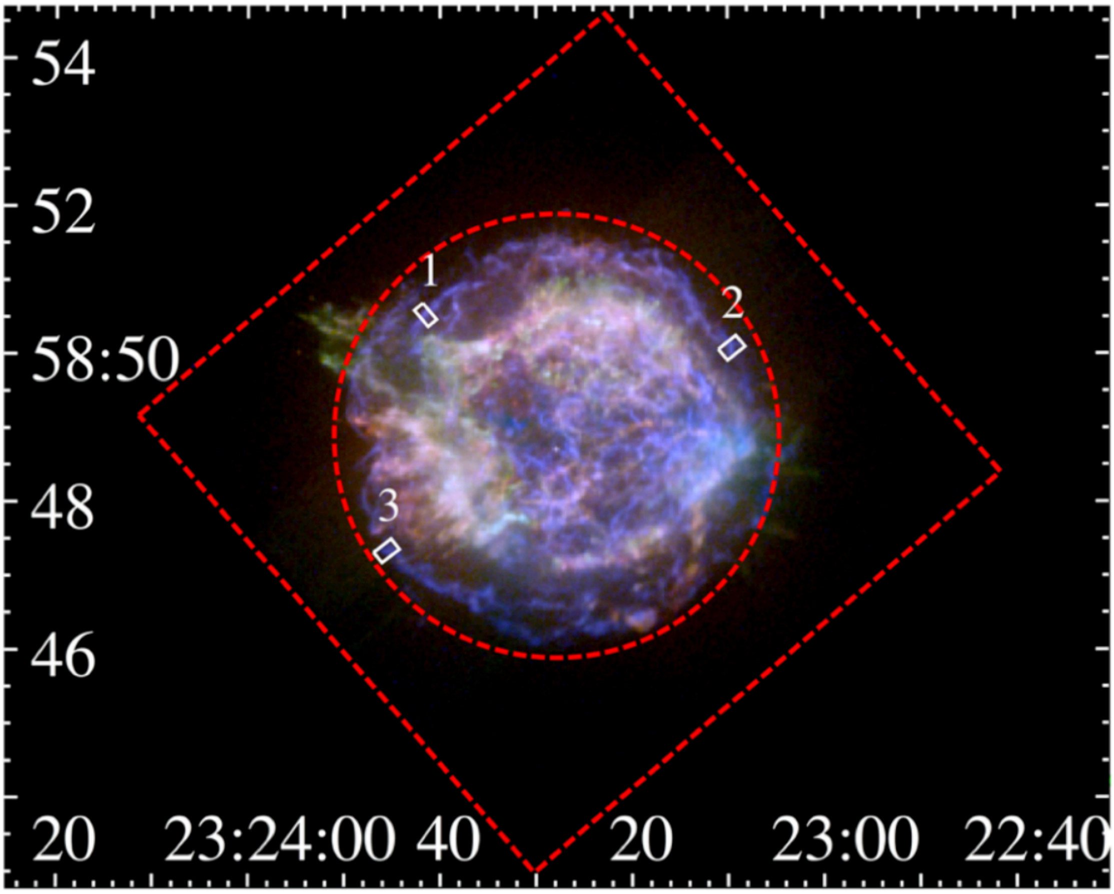

The source regions are given in numbered white solid rectangular areas and the background region is chosen with the dashed lines, the whole SNR is excluded from the background region.

Figure 5.1 RGB image of Cas A with the source and background regions.

5.2.1.3 Spectral Analysis Results of Cas A

Cas A is an X-ray synchrotron emitting SNR [64], [68]. Due to obtain roll-off frequency to calculate maximum energy of electrons ($E_{max,e}$) with using the analysis methods described in previous section, background analysis was also aimed for a comparative approach to get sensitive values about synchrotron spectrum parameters. In accordance with these purposes, the background region was modelled, and the best-fit parameters are given in Table 5.2 and the spectrum is in Figure 5.2. Also, the spectra of selected source regions are shown in Figure 5.3, 5.4 and 5.5 and the best-fit parameters for both NT models can be seen in Table 5.3 and Table 5.4 for BGD-1 and BGD-2 subtracted spectra, respectively.

Table 5.2 Best-fit parameters for the background spectrum of Cas A.

Components	Parameters	Values
CXB	N_H (10^{22} cm^{-2}) ‡	0.394 (fixed)
	Photon Index †	1.412 (fixed)
	S. B. (erg s^{-1} cm^{-2} arcmin^{-2}) †	5.410×10^{-15} (fixed)
FE	kT (keV)	$1.074^{+0.004}_{-0.004}$
	norm (10^{-2} photons cm^{-2} s^{-1})	$0.325^{+0.006}_{-0.006}$
GH_{hot} & GH_{cold}	N_H (10^{22} cm^{-2})	$2.115^{+0.007}_{-0.007}$
	kT_e (keV) ‖	0.658(fixed)
	norm (photons cm^{-2} s^{-1})	$0.373^{+0.003}_{-0.003}$
	kT_e (keV) ‖	1.500 (fixed)
	norm (10^{-2} photons cm^{-2} s^{-1})	$4.964^{+0.007}_{-0.007}$
	χ^2 / dof	434.23 / 439

†: [50] (S. B.: Surface Brightness in the 2 – 10 keV band), ‡: [88], ‖: [89].

Table 5.3 Best-fit parameters for BGD-1 subtracted spectrum of selected emission regions on Cas A (0.5 − 7 keV).

Components	**Parameters**		**Values**	
		Source#1	Source#2	Source#3
Absorption	N_H (10^{22} cm^{-2})	$1.07^{+0.04}_{-0.06}$	$1.75^{+0.11}_{-0.10}$	$1.36^{+0.12}_{-0.11}$
Line#1	(keV)	$2.00^{+0.02}_{-0.02}$	$4.33^{+0.05}_{-0.05}$	$3.03^{+0.11}_{-0.10}$
	norm (10^{-6} photons cm^{-2}s^{-1})	$5.85^{+1.65}_{-1.72}$	$1.41^{+0.92}_{-0.92}$	$0.92^{+0.90}_{-0.89}$
Line#2	(keV)	$1.83^{+0.01}_{-0.01}$	$1.88^{+0.01}_{-0.01}$	$1.90^{+0.01}_{-0.02}$
	norm (10^{-6} photons cm^{-2}s^{-1})	$14.15^{+0.22}_{-0.21}$	$14.51^{+3.19}_{-3.20}$	$13.40^{+2.45}_{-2.38}$
Line#3	(keV)	$2.45^{+0.02}_{-0.01}$	$2.43^{+0.03}_{-0.03}$	$2.47^{+0.06}_{-0.05}$
	norm (10^{-6} photons cm^{-2}s^{-1})	$9.69^{+1.84}_{-1.85}$	$4.30^{+2.12}_{-2.12}$	$4.73^{+1.58}_{-1.58}$
Line#4	(keV)	$2.27^{+0.04}_{-0.05}$	$1.48^{+0.04}_{-0.05}$	$3.24^{+0.16}_{-0.15}$
	norm (10^{-6} photons cm^{-2}s^{-1})	$2.40^{+1.79}_{-1.87}$	$4.20^{+1.27}_{-1.27}$	$1.38^{+1.12}_{-1.16}$
Line#5	(keV)	$1.03^{+0.90}_{-0.83}$	$1.07^{+0.05}_{-0.05}$	$1.10^{+0.02}_{-0.02}$
	norm (10^{-6} photons cm^{-2}s^{-1})	$1.03^{+0.90}_{-0.83}$	$23.74^{+1.21}_{-1.24}$	$19.24^{+8.26}_{-8.30}$
Line#6	(keV)	$0.86^{+0.04}_{-0.04}$	$0.99^{+0.02}_{-0.03}$	
	norm (10^{-6} photons cm^{-2}s^{-1})	$1.96^{+1.09}_{-1.15}$	$2.82^{+1.22}_{-1.38}$	
POWER-LAW	Photon Index	$2.29^{+0.04}_{-0.07}$	$2.58^{+0.09}_{-0.09}$	$2.18^{+0.11}_{-0.11}$
	norm (10^{-6} photons cm^{-2}s^{-1})	$0.63^{+0.03}_{-0.05}$	$1.19^{+0.11}_{-0.13}$	$0.41^{+0.05}_{-0.06}$
	χ^2 / d.o.f.	187.85 / 140	129.64 / 140	86.08 / 105
SRCUT	Spectral Index (α)		0.77 (fixed)	0.77 (fixed)
	$\nu_{\text{roll-off}}$ (10^{16} Hz)		$33.29^{+1.22}_{-1.17}$	$170.13^{+15.17}_{-18.77}$
	Flux (10^{-12} ergs cm^{-2} s^{-1}) ‡		$1.34^{+0.01}_{-0.01}$	$0.81^{+0.01}_{-0.01}$
	χ^2 / d.o.f.		144.47 / 145	85.24 / 106

‡ Flux in 0.5 − 7 keV band.

Table 5.4 Best-fit parameters for BGD-2 subtracted spectrum of selected emission region on Cas A (0.5 − 7 keV).

Components	**Parameters**		**Values**	
		Source#1	Source#2	Source#3
Absorption	N_H (10^{22} cm^{-2})	$1.04^{+0.03}_{-0.07}$	$1.04^{+0.03}_{-0.06}$	$1.30^{+0.12}_{-0.11}$
Line#1	(keV)	$2.00^{+0.03}_{-0.02}$	$2.00^{+0.03}_{-0.02}$	$2.37^{+0.09}_{-0.08}$
	norm (10^{-6} photons cm^{-2}s^{-1})	$6.22^{+1.73}_{-1.70}$	$6.21^{+1.73}_{-1.70}$	$2.68^{+1.32}_{-1.33}$
Line#2		$1.83^{+0.01}_{-0.01}$	$1.83^{+0.01}_{-0.01}$	$1.89^{+0.01}_{-0.01}$
	norm (10^{-6} photons cm^{-2}s^{-1})	$15.67^{+5.34}_{-2.16}$	$15.67^{+5.33}_{-215}$	$16.34^{+2.44}_{-2.51}$
Line#3		$2.44^{+0.01}_{-0.01}$	$2.45^{+0.01}_{-0.01}$	$2.49^{+0.05}_{-0.04}$
	norm (10^{-6} photons cm^{-2}s^{-1})	$10.10^{+1.85}_{-1.82}$	$10.10^{+1.85}_{-1.82}$	$4.22^{+2.04}_{-2.03}$
Line#4		$2.27^{+0.04}_{-0.05}$	$2.27^{+0.04}_{-0.05}$	$3.20^{+0.11}_{-0.15}$
	norm (10^{-6} photons cm^{-2}s^{-1})	$2.49^{+1.82}_{-1.82}$	$2.49^{+1.82}_{-1.82}$	$1.53^{+1.11}_{-1.11}$
Line#5		$1.03^{+0.02}_{-0.02}$	$1.03^{+0.02}_{-0.02}$	$1.09^{+0.02}_{-0.02}$
	norm (10^{-6} photons cm^{-2}s^{-1})	$2.68^{+0.66}_{-0.71}$	$26.81^{+6.57}_{-7.10}$	$22.44^{+1.12}_{-8.68}$
Line#6		$0.87^{+0.06}_{-0.05}$	$0.87^{+0.06}_{-0.05}$	-
	norm (10^{-6} photons cm^{-2}s^{-1})	$1.70^{+1.11}_{-1.08}$	$1.70^{+1.10}_{-1.08}$	-
POWER-LAW	Photon Index	$2.25^{+0.04}_{-0.04}$	$2.25^{+0.04}_{-0.04}$	$2.10^{+0.12}_{-0.11}$
	norm (10^{-3} photons cm^{-2}s^{-1})	$0.60^{+0.01}_{-0.01}$	$0.60^{+0.02}_{-0.03}$	$0.37^{+0.05}_{-0.05}$
	χ^2 / d.o.f.	189.59 / 140	135.54 / 142	87.92 / 105
SRCUT	Spectral Index (α)	-	0.77 (fixed)	0.77 (fixed)
	$\nu_{roll\text{-}off}$ (10^{16} Hz)	-	$33.24^{+1.21}_{-1.19}$	$315.44^{+40.26}_{-36.88}$
	Flux (10^{-12} ergs cm^{-2} s^{-1}) ‡	-	$1.35^{+0.01}_{-0.02}$	$0.82^{+0.01}_{-0.01}$
	χ^2 / d.o.f.	-	144.42 / 145	88.20 / 106

‡ Flux in 0.5 − 7 keV band.

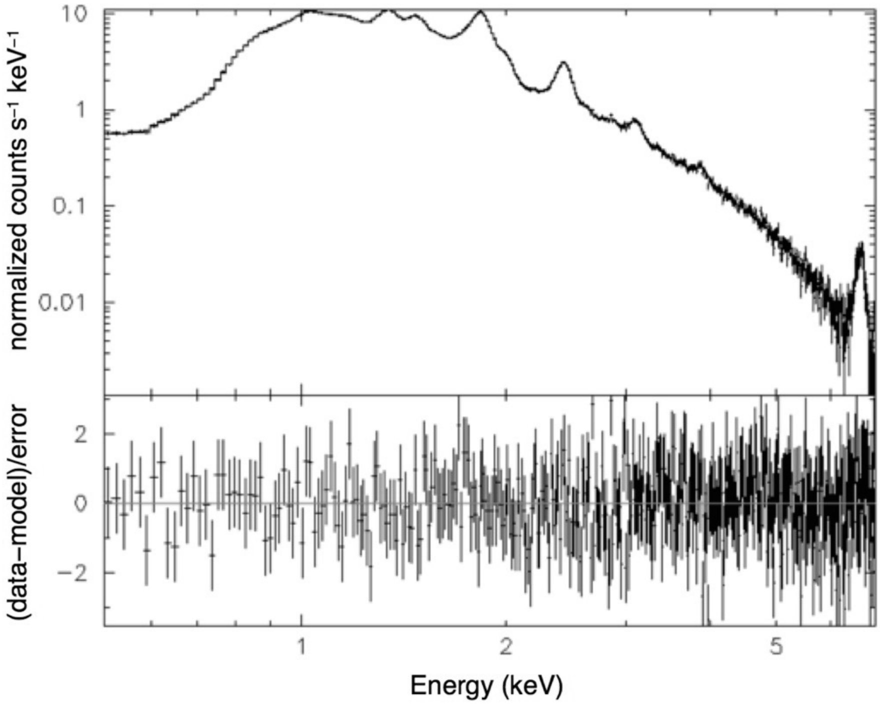

Figure 5.2 Modelled background spectrum of the selected region of Cas A.

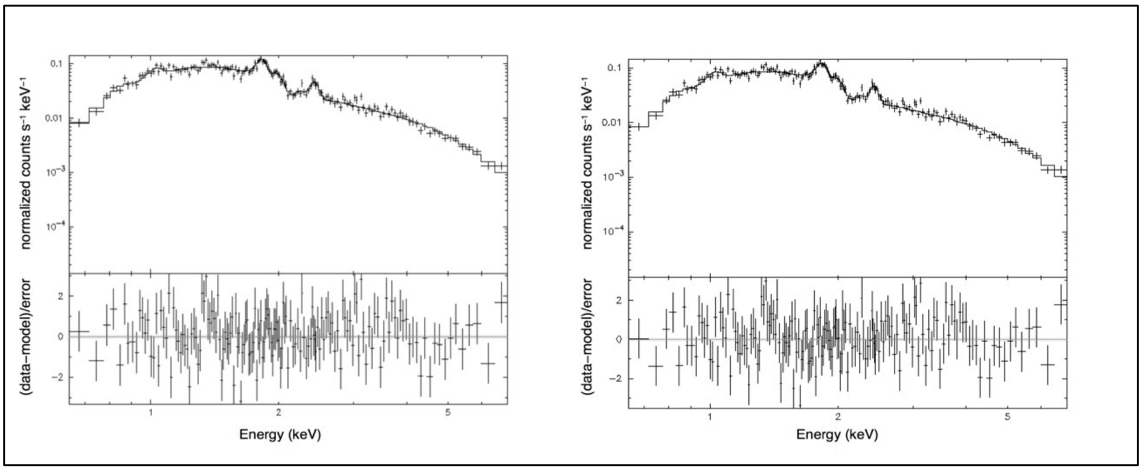

Figure 5.3 BGD-1 (left) and BGD-2 (right) subtracted spectra of the region#1.

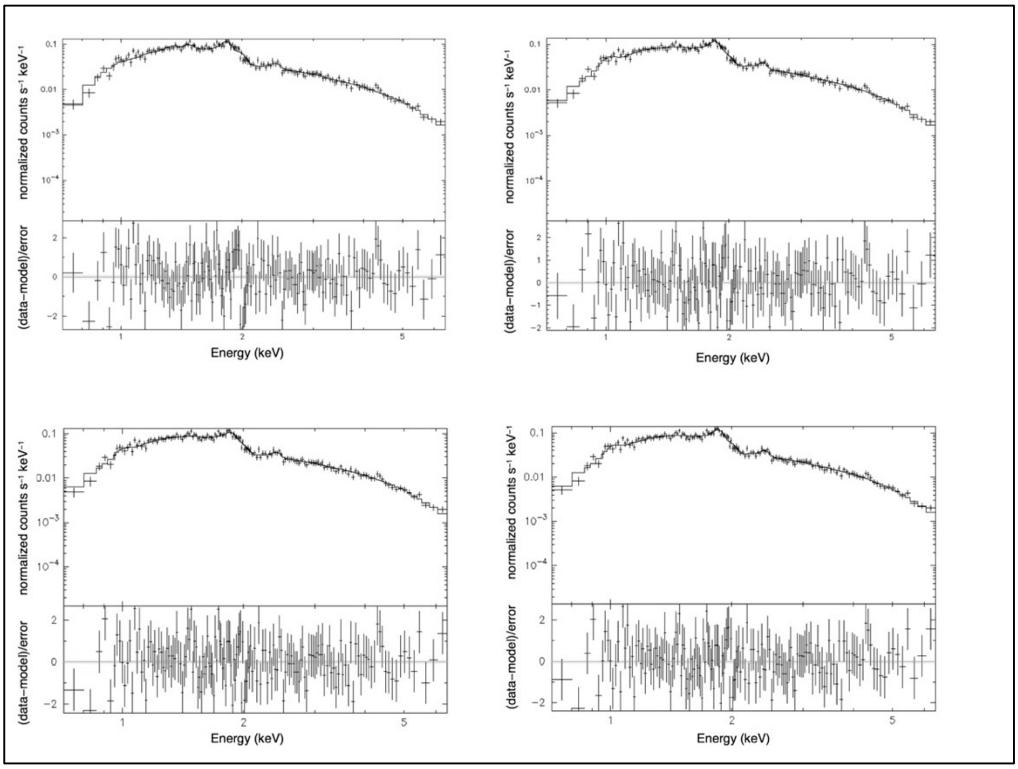

Figure 5.4 BGD-1 (left) and BGD-2 (right) subtracted spectra of the region#2.

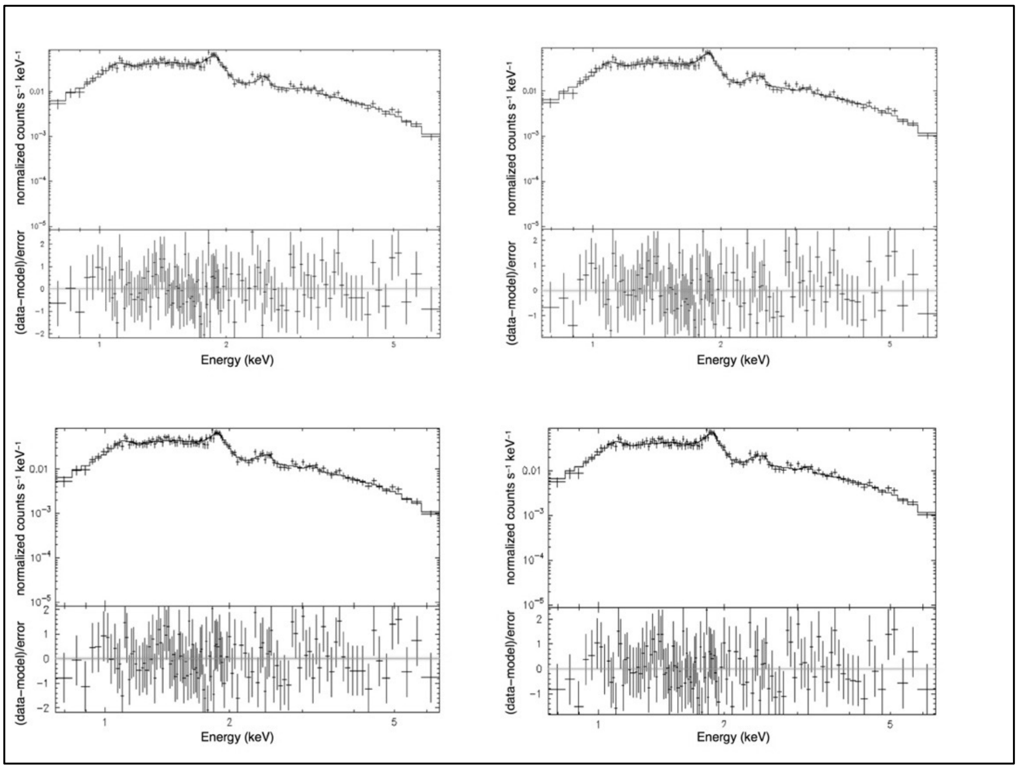

Figure 5.5 BGD-1 (left) and BGD-2 (right) subtracted spectra of the region#3.

5.2.2 RCW 86

5.2.2.1 Literature

According to the abundances of O, Ne, Mg and Si are significantly higher than that of Fe, Bamba et al. (2000) [90] suggested in their *ASCA* study that RCW 86 is a Type II SN. This result is consistent with RCW 86 is in an OB star association. They also found that RCW 86 have three components: i) a high-temperature plasma, ii) a low-temperature plasma, iii) a PL emission (NT component).

In their study, Vink et al. (2000) [91] discussed that the remnant is not circularly symmetric. The northeast and southwest of the remnant have contrast in emission between them. They suggest the in southwest the shock wave is encountering a denser medium, and this could mean that the actual explosion centre was more to the southwest of the geometrical centre, and closer to the unresolved source.

In their *XMM-Newton* study Vink et al. (2002) [92] suggested that the hard X-ray emission in RCW 86 is originated from two distinct components: ultra-relativistic electrons and a hot plasma, and argued that the hard X-ray emission from RCW 86 is bremsstrahlung rather than synchrotron emission.

Using *Chandra* observations, Rho et al. (2002) [93] concluded that the morphology of hard and soft X-rays in RCW 86 supports the hypothesis of different origins. Their spectral analysis confirmed that the hard X-rays from the SNR are best characterised by a synchrotron continuum with Fe-K_α line emission. With this result, they implied that some of the original SN ejecta are still unmixed after $\sim 10^4$ yr, and the RS into those ejecta can also accelerate electrons to X-ray synchrotron-emitting energies of order 50 TeV.

In the study of the NE shell of RCW 86, which is observed by *Suzaku*, Yamaguchi et al. (2008) [94] found that the high-temperature plasma includes an over-solar abundant iron, and has an extremely low plasma age of $\tau \sim 2.3 \times 10^9$ cm^{-3} s, and suggested this component may be Fe-rich ejecta, very recently heated by RS. On the other hand, they found the low-temperature plasma has sub-solar metal abundances, and suggested that the origin of this component could be a blast-shocked ISM. Furthermore, they suggest that the blast wave at the NE part of the SNR may still be expanding in a nebulous region, which provides a high shock velocity for the particle acceleration mechanism.

They fitted well the eastern region (Fe-K_{α} enhanced region and soft X-rays) of the remnant, with two thin-thermal plasmas, which have temperatures of ~0.3 keV and ~1.8 keV, and one PL model with a photon index of ~2.9. They extracted spectra from the hard X-ray filament (the NE region), which is represented by a low-temperature plasma with a PL that the brightest in this region, and can be marked as synchrotron radiation.

Yamaguchi et al. (2012) [95] studied newly-discovered Fe-rich ejecta of RCW 86 observed by *Suzaku*, and concluded that the low-temperature component originates from the forward shocked ISM, and estimated a total Fe mass of about $1M_{\odot}$. They suggested that the SNR originates from a Type Ia SN explosion rather than a CC that considered previously studies, based on the derived radii of the FS and RS (14 pc and 8 pc, respectively), an ambient density of 0.075 cm^{-3}, and the total ejecta mass of 1 $M_{\odot}$ – $2M_{\odot}$. They represented the spectra of each region by a three-component model consisting of low- and high-temperature thermal plasmas and a NT emission.

Castro et al. (2013) [96] used *Chandra* archival data to characterize the synchrotron emission on the NW region of the SNR RCW 86. They fitted spectra from several different regions: diffuse and filamentary alike. The width of these filaments (l ~ $10''$ – $30''$) constricts the minimum magnetic field strength at the post-shock (PS) region (B ~ 80 μG). They estimated the velocity of the shock at the main NW rim of the SNR is to be $V_S = 650 \pm 120$ km s^{-1}. They also found that RCW 86 has a peculiar shape with X-ray synchrotron filaments due to its low shock velocities and irregular morphology.

According to the *XMM-Newton* RGS data and hydro-dynamical simulations, Broersen et al. (2014) [97] showed that RCW 86 may be the remnant of SN 185 A.D. SN of RCW 86 is the likely result of a Type Ia explosion of single degenerate origin. The supernova exploding in a wind-blown cavity explained by the large differences in ionisation ages between the shocked ISM and shocked ejecta. They fitted the spectra with two non-equilibrium ionisation models, and also performed principal component analysis. They also showed that Si and Fe-K line emitting shocked ejecta constrained to a shell of ~2 pc.

Utilizing *Chandra* archival data, Yamaguchi et al. (2016) [98] found that the velocity of the NT filaments in the X-ray proper motion in the RCW 86 NW rim is derived at the distance of 2.5 kpc to be 1800 – 3000 km s^{-1}.

Tsubone et al. (2017) [99] presented he *Suzaku* archival data analysis of the spatially resolved spectroscopy of the whole SNR. They fitted the spectra with a combination of a PL for synchrotron emission, and two-component optically thin-thermal plasma for shocked ISM (~0.3 keV), and Fe-dominated ejecta (~2 keV). They discovered systematic trends of the synchrotron X-rays, which become more predominant, and the photon indices become flatter with decreasing the emission measure of the shocked ISM. According to these results, they suggested that CRs are accelerated in the low-density regions, more efficiently.

5.2.2.2 Background Estimation

The background region data for *XMM-Newton* analysis, extracted from a circular source free area of 58.63 arcmin^2 (Figure 5.6) in the same FoV.

RCW 86 is above the Galactic plane (l = $315\overset{\circ}{.}0927$, b = $-02\overset{\circ}{.}3765$). Thus, the possible contamination of the GRXE is negligible [87].

The background spectrum of RCW 86 *XMM-Newton* observation consists of the CXB and FE components. The spectrum was fitted with a model of [$\mathrm{Abs}_{(\mathrm{CXB})} \times \mathrm{PL}_{(\mathrm{CXB})}$ + APEC] where the CXB component parameters were fixed with the parameters mentioned before in the background analysis method of Cas A. The second term is FE component which is represented with *APEC*. To calculate the absorption parameter, *TBABS* model was used [60], and the hydrogen column density parameter of CXB component was fixed to 0.723×10^{22} cm^{-2} as in the study of [100]. This value was taken from study of [88]. The background spectrum is simulated with using the *FAKEIT* command, and subtracted from the source spectra. The best-fit parameters and spectrum of the background are given in the Table 5.5 and Figure 5.7, respectively.

5.2.2.3 Spectral Fitting

Figure 5.6 shows XMM-Newton MOS1/2 and pn merged X-ray RGB image of RCW 86 in the mentioned energy bands in the caption. Images of MOS1/2 are binned with 22″ × 22″, and pn image is binned with 82″ × 82″.

Images and spectra were created by selecting single and double pixel with PATTERN = 0 − 4 for the EPIC-pn, and single to quadruple-pixel events with PATTERN = 0 − 12 for the EPIC-MOS1/2. Images of the edge of the remnant were produced by superposing the MOS1/2 and pn images with the task *EMOSAIC*. All the images were adaptively smoothed with the task *ASMOOTH*.

Three spectral source regions were extracted (Figure 5.6). For spectral analysis, they were grouped with a minimum of 25 counts bin^{-1}. The X-ray spectra of selected regions are well represented by the absorbed NT models *PL* or *SRCUT*, and non-equilibrium ionisation collisional plasma model (*VNEI*) with Gaussian emission lines. The Gaussian line width parameter was fixed to 0 eV. Absorbed *PL* model fitting gives three parameters: Absorbing column density N_H, the photon index Γ, and also absorption-corrected X-ray flux $F_{0.5-7keV}$ which is used for adjusting the normalization parameter while fitting with the *SRCUT* model. The X-ray spectra are shown in Figure 5.8, 5.9 and 5.10, and the best-fit parameters for both NT models can be seen in Table 5.6 and Table 5.7 for BGD-1 and BGD-2 subtracted spectra, respectively.

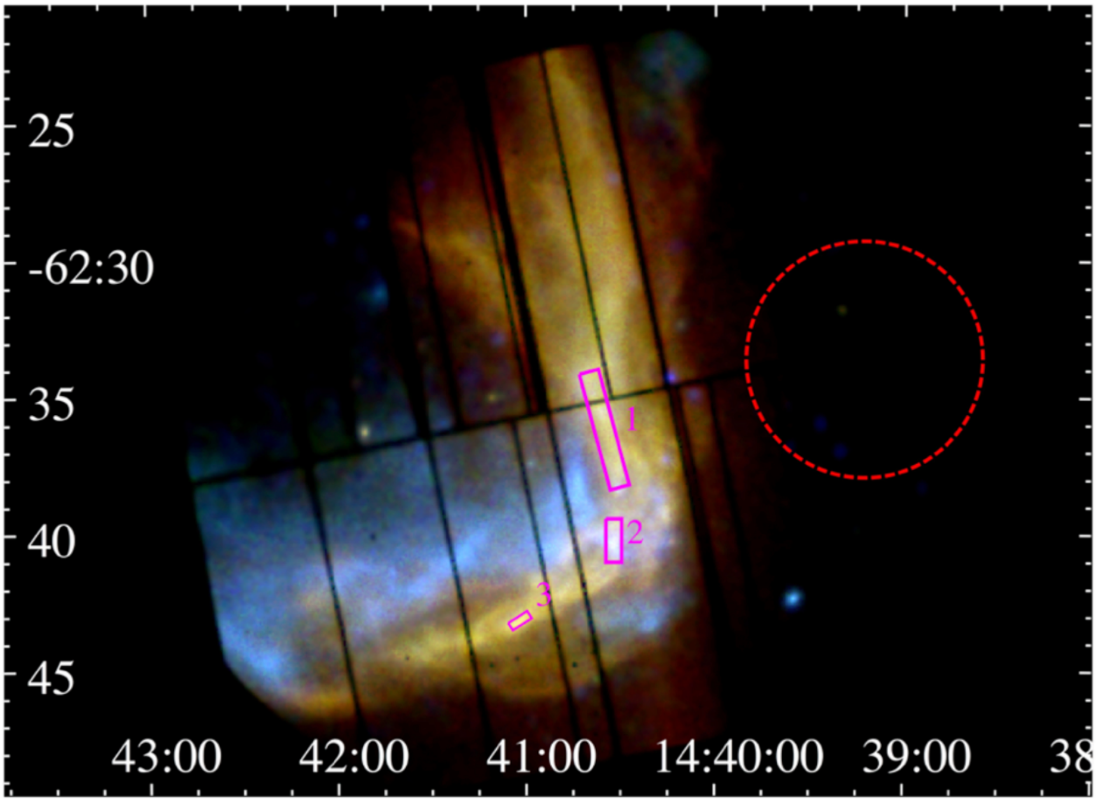

The source regions are given in numbered magenta solid rectangular areas and the background region is chosen with the dashed circular region.

Figure 5.6 RGB image of RCW 86 with the source and background regions.

5.2.2.4 Spectral Analysis Results of RCW 86

RCW 86 is an X-ray synchrotron emitting SNR [97], [99]. Due to obtain roll-off frequency to calculate maximum energy of electrons ($E_{max,e}$) with using the analysis methods described in previous section, background analysis was also aimed for a comparative approach to get sensitive values about synchrotron spectrum parameters. In accordance with these purposes, the background region was modelled and it is best-fit parameters are given in Table 5.2 and the spectrum is in Figure 5.7. Also, the spectra of selected source regions are shown in Figure 5.8, 5.9 and 5.10 and the best-fit parameters for both NT models are shown in Table 5.6 and Table 5.7 for BGD-1 and BGD-2 subtracted spectra, respectively. All errors indicate 90% confidence intervals.

Table 5.5 Best-fit parameters for the background spectrum of RCW 86.

Components	**Parameters**	**Values**
CXB	N_H (10^{22} cm^{-2}) ‡	0.723 (fixed)
	Photon Index †	1.412 (fixed)
	S. B. (erg s^{-1} cm^{-2} arcmin^{-2}) †	5.410×10^{-15} (fixed)
FE	kT_e (keV)	$0.703^{+0.014}_{-0.014}$
	norm (10^{-2} photons cm^{-2} s^{-1})	$0.037^{+0.010}_{-0.010}$
	χ^2 / d.o.f.	256.89 / 258

†: [50] (S. B.: Surface Brightness in the 2 – 10 keV band). ‡: [88]

Table 5.6 Best-fit parameters for BGD-1 subtracted spectrum of selected emission region on the W rim of RCW 86. The energy ranges are 0.5 − 7 keV for Source#1-2, and 0.6 − 2 keV for Source#3.

Components	**Parameters**		**Values**	
		Source#1	Source#2	Source#3
Absorption	N_H (10^{21} cm^{-2})	$6.32^{+0.02}_{-0.03}$	$6.45^{+0.02}_{-0.01}$	$6.44^{+0.38}_{-0.41}$
VNEI (Ejecta#1)	kT_e (keV)	$0.19^{+0.01}_{-0.01}$	$0.19^{+0.01}_{-0.01}$	$0.20^{+0.01}_{-0.01}$
	τ (10^{11} cm^{-3} s)	$2.91^{+0.47}_{-0.16}$	$2.85^{+0.19}_{-0.38}$	$2.96^{+0.82}_{-0.58}$
	norm (10^{-2} photons cm^{-2}s^{-1})	$20.00^{+0.40}_{-0.30}$	$10.85^{+2.23}_{-0.81}$	$5.18^{+0.01}_{-0.01}$
VNEI (Ejecta#2)	kT_e (keV)	$0.62^{+0.10}_{-0.04}$	$0.66^{+0.41}_{-0.18}$	$0.74^{+0.35}_{-0.14}$
	Ne	$2.09^{+0.20}_{-0.55}$	$1.92^{+0.28}_{-0.27}$	$2.19^{+0.64}_{-0.43}$
	Mg	$1.22^{+0.08}_{-0.15}$		
	Si	$2.15^{+0.23}_{-0.25}$	$2.09^{+0.22}_{-0.27}$	$1.73^{+0.41}_{-0.32}$
	S	$2.93^{+0.45}_{-0.67}$		
	τ (10^{10} cm^{-3} s)	$3.01^{+0.11}_{-0.36}$	$2.32^{+0.44}_{-0.49}$	$3.42^{+1.72}_{-1.41}$
	norm (10^{-2} photons cm^{-2}s^{-1})	$0.67^{+0.02}_{-0.02}$	$0.25^{+0.01}_{-0.01}$	$0.13^{+0.01}_{-0.01}$
Line#1	Uncertainty of the Fe L-shell data in the VNEI code	1.21 (fixed)	1.21 (fixed)	-
Line#2	Fe Kα energy centroid (eV)	6.45 (fixed)	6.45 (fixed)	-
POWER-LAW	Photon Index	$3.01^{+0.09}_{-0.09}$	$2.84^{+0.08}_{-0.09}$	-
	norm (10^{-3} photons cm^{-2}s^{-1})	$1.49^{+0.01}_{-0.09}$	$1.19^{+0.11}_{-0.13}$	-
	χ^2 / d.o.f.	551.72 / 479	486.13 / 395	-
SRCUT	Spectral Index (α)	0.60 (fixed)	0.60 (fixed)	-
	$\nu_{roll\text{-}off}$ (10^{16} Hz)	$4.75^{+0.23}_{-0.22}$	$8.16^{+0.27}_{-0.33}$	-
	Flux (10^{-12} ergs cm^{-2} s^{-1}) ‡	$19.37^{+0.01}_{-0.24}$	$9.01^{+0.04}_{-0.05}$	-
	χ^2 / d.o.f.	552.05 / 463	449.27 / 393	213.37 / 194

‡: Flux in 0.5 − 7 keV band.

Table 5.7 Best-fit parameters for BGD-2 subtracted spectrum of selected emission region on the W rim of RCW 86. The energy ranges are 0.5 − 7 keV for Source#1-2, and 0.6 − 2 keV for Source#3.

Components	**Parameters**		**Values**	
		Source#1	Source#2	Source#3
Absorption	N_H (10^{21} cm^{-2})	$6.74^{+0.02}_{-0.03}$	$6.55^{+0.02}_{-0.01}$	$6.50^{+0.04}_{-0.04}$
VNEI (Ejecta#1)	kT_e (keV)	$0.18^{+0.01}_{-0.01}$	$0.19^{+0.01}_{-0.01}$	$0.20^{+0.01}_{-0.01}$
	τ (10^{11} cm^{-3} s)	$3.49^{+0.78}_{-1.35}$	$2.68^{+0.60}_{-0.13}$	$3.01^{+0.83}_{-0.48}$
	norm (10^{-2} photons cm^{-2} s^{-1})	$28.00^{+0.55}_{-0.53}$	$11.00^{+0.38}_{-0.21}$	$5.38^{+1.00}_{-1.27}$
VNEI (Ejecta#2)	kT_e (keV)	$0.50^{+0.06}_{-0.01}$	$0.76^{+0.02}_{-0.01}$	$0.76^{+0.43}_{-0.18}$
	Ne	$1.54^{+0.17}_{-0.12}$	$2.02^{+0.18}_{-0.41}$	$2.19^{+0.42}_{-0.34}$
	Mg	$1.02^{+0.10}_{-0.10}$		
	Si	$1.94^{+0.20}_{-0.26}$	$1.96^{+0.51}_{-0.30}$	$1.71^{+0.43}_{-0.31}$
	S	$3.14^{+1.27}_{-1.51}$		
	τ (10^{10} cm^{-3} s)	$4.44^{+0.97}_{-0.76}$	$2.18^{+1.06}_{-0.63}$	$3.34^{+1.90}_{-1.40}$
	norm (10^{-2} photons cm^{-2} s^{-1})	$1.22^{+0.03}_{-0.02}$	$0.19^{+0.03}_{-0.07}$	$0.12^{+0.01}_{-0.01}$
Line#1	Uncertainty of the Fe L-shell data in the VNEI code	1.21 (fixed)	1.21 (fixed)	-
Line#2	Fe Kα energy centroid (eV)	6.45 (fixed)	6.45 (fixed)	-
POWER-LAW	Photon Index	$2.79^{+0.09}_{-0.08}$	$2.79^{+0.11}_{-0.11}$	-
	norm (10^{-3} photons cm^{-2} s^{-1})	$1.36^{+0.14}_{-0.12}$	$1.16^{+0.13}_{-0.12}$	-
	χ^2 / d.o.f.	625.00 / 464	488.22 / 395	-
SRCUT	Spectral Index (α)	0.60 (fixed)	0.60 (fixed)	-
	$\nu_{\text{roll-off}}$ (10^{16} Hz)	$8.80^{+0.29}_{-0.29}$	$8.52^{+0.16}_{-0.16}$	-
	Flux (10^{-12} ergs cm^{-2} s^{-1}) ‡	$19.53^{+0.14}_{-0.20}$	$9.07^{+0.01}_{-0.27}$	-
	χ^2 / d.o.f.	649.50 / 479	478.30 / 395	217.97 / 194

‡ Flux in 0.5 − 7 keV band.

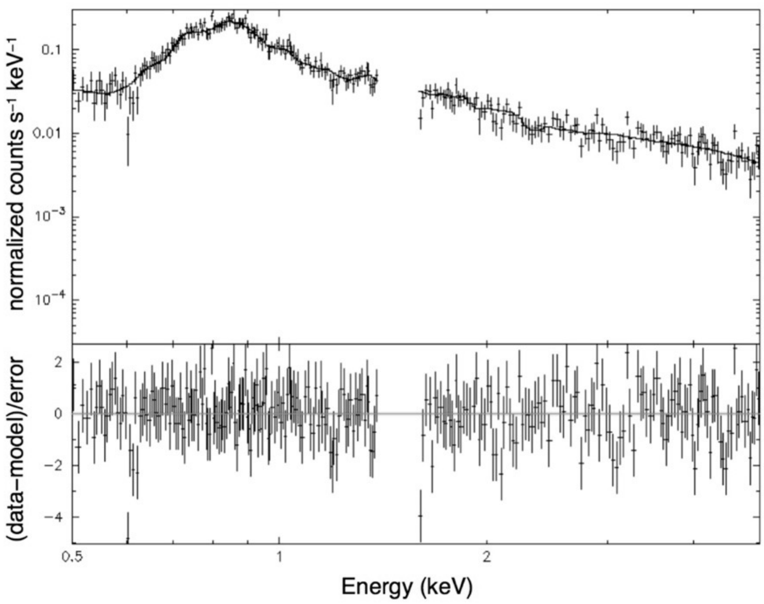

Figure 5.7 Modelled background spectrum of the selected region of RCW 86. 1.39 – 1.59 keV energy range was ignored because of the instrumental Al-K_{α} line.

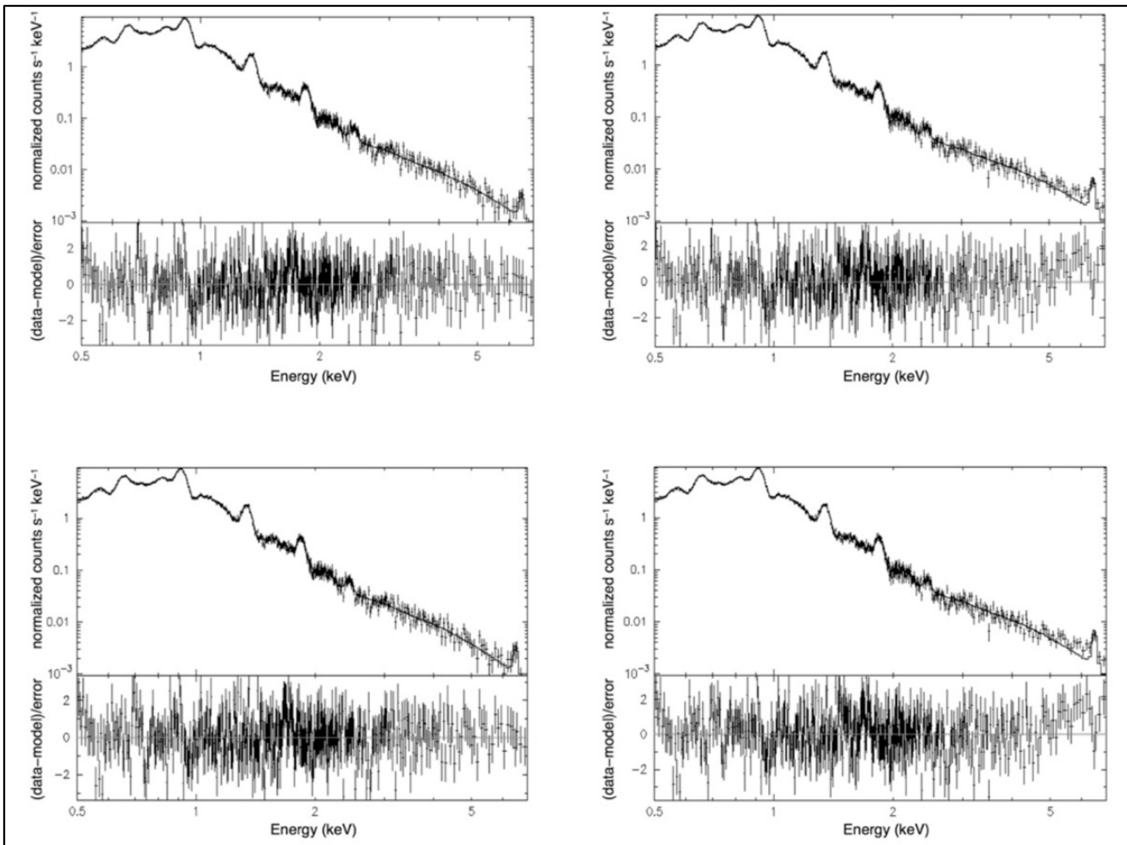

Left panels shows the BGD-1 subtracted spectra. Right panels show the BGD-2 subtracted spectra, each modelled with *PL* and *SRCUT*.

Figure 5.8 BGD-1 (left) and BGD-2 (right) subtracted spectra of the region#1.

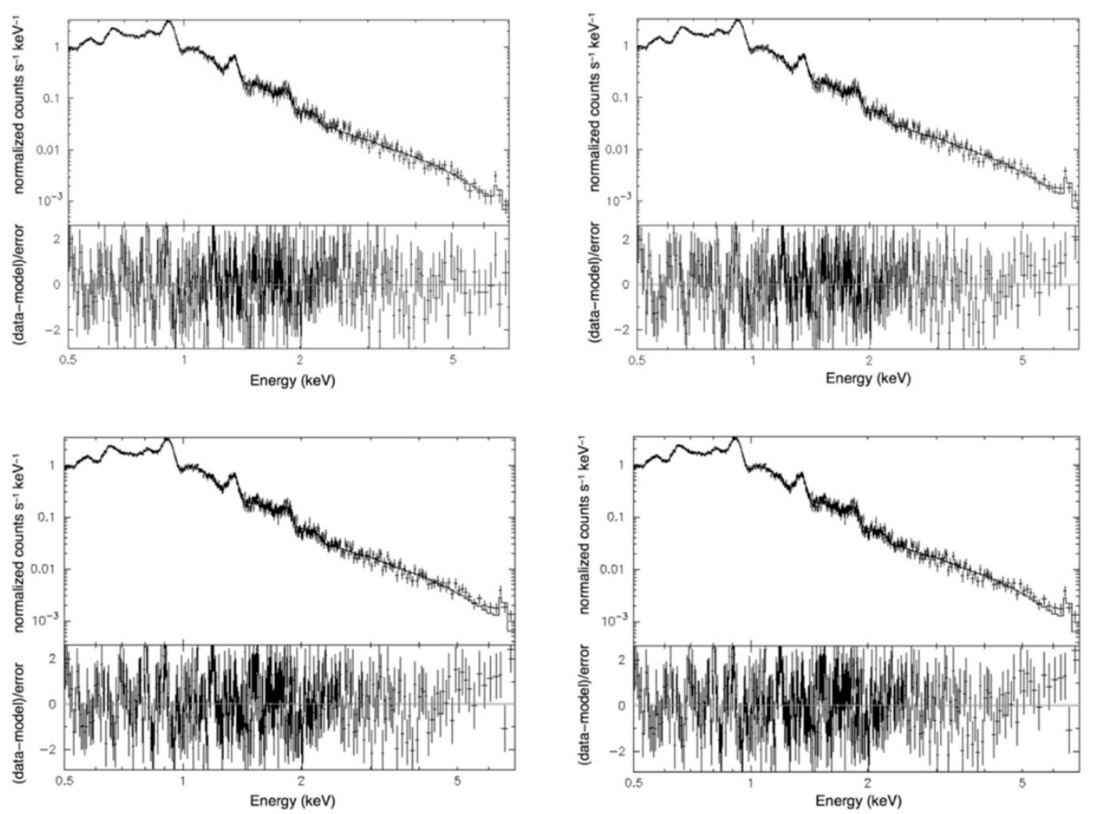

Left panels show the BGD-1 subtracted spectra. Right panels show the BGD-2 subtracted spectra, each modelled with *PL* and *SRCUT*.

Figure 5.9 BGD-1 (left) and BGD-2 (right) subtracted spectra of the region#2.

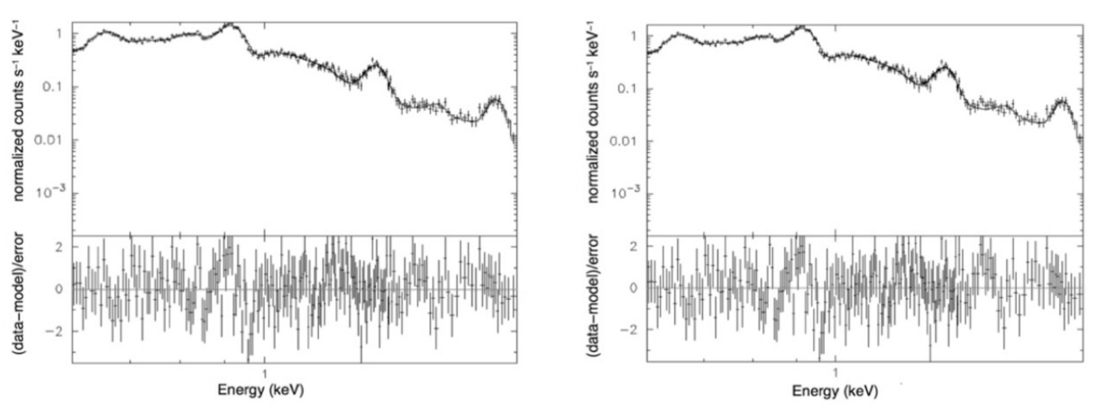

Left panel shows the BGD-1 subtracted spectra. Right panels show the BGD-2 subtracted spectra, each modelled with absorbed *VNEI* model.

Figure 5.10 BGD-1 (left) and BGD-2 (right) subtracted spectra of the region#3.

5.2.3 RX J1713.7−3946

5.2.3.1 Literature

RX J1713.7−3946 features NT components in its X-ray emission. Utilizing the *ROSAT*, *ASCA* and *RXTE* observation data and using a combination of the models *SRCUT* and *EQUIL* to fit the NT and thermal emission, Pannuti and Allen (2002) [101] found evidence for modest thermal emission energy of this thermal component that is $kT_e \sim 1.4$ keV. They suggest that this may be associated with the diffuse emission from the SNR. Also, for the maximum energy of the accelerated CR electrons by this SNR, they obtain an estimation of 70 TeV.

Analysing the *ASCA* data to discover of a diffuse X-ray source, Uchiyama et al. (2002) [102] showed that the strong shock of RX J1713.7−3946 is evidenced by CO-line observations, and it seems to be a site of acceleration of NT particles. Hence, this strong shock is likely to interact with the molecular cloud. The observed luminosity is $L_X = 1.7 \times 10^{35}$ erg s^{-1} (for a distance of 6 kpc). Furthermore, describing by a PL with a photon index of ~1.0, the energy spectrum (1 − 10 keV) of the hard X-ray source showed a flat continuum.

Pannuti et al. (2003) [103] used data from *RXTE* PCA, *ASCA* GIS, and *ROSAT* PSPC for their analysis, and fitted the spectra with *SRCUT* model, described an exponential cut-off in the population of the highest energy electrons accelerated by the SNR. They showed a weak emission near 6.4 keV in the *RXTE* PCA spectrum, likely originates from the diffuse X-ray emission from the surrounding Galactic ridge rather than from the SNR itself. They suggest that thermal emission is correlated with the diffuse emission in the interior of the remnant. They also estimated the maximum energy ($E_{cut\text{-}off}$) of CR electrons accelerated by the rims of the SNR to be 19 − 25 TeV (assuming a magnetic field strength of B = 10 μG) from their two component (thermal and non-thermal) fits to the X-ray emission from the NW rim and the central diffuse emission from the SNR.

Analysing the *XMM-Newton* archival data, an excess in the CO emission is found in the study of Cassam-Chenaï et al. (2004) [104] in the SW region of the SNR. This excess suggests that the absorption is due to molecular clouds. Instead of the commonly accepted value of 6 kpc, on the condition the SNR lies at a distance of 1.3 ± 0.4 kpc, the inferred cumulative absorbing column densities are in agreement with the X-ray findings in different places of the remnant. They also found that RX J1713.7–3946's progenitor mass between 12$M_\odot$ and 16$M_\odot$ according to a scenario based on a modified ambient medium due to the effect of a progenitor stellar wind. Also they found a strong absorption in the SW, and strong variations (0.4×10^{22} cm^{-2} $\leq N_H \leq 1.1\times10^{22}$ cm^{-2}) revealed by the X-ray mapping of the absorbing column density. There is a correlation between the X-ray brightness and the X-ray absorption along the western rims, and on this basis, they come with the correlation that the shock front of the SNR is encountering with the surrounding molecular clouds.

Analysing the *XMM-Newton* observation data, Hiraga et al. (2005) [105] did not found any complex structures in the interior region of the SNR, and fitted the spectra with a PL function, whose photon index ranges within $\Gamma = 2.0 – 2.8$ assuming some absorption of $10^{21} – 10^{22}$ cm^{-2}.

Using the observation data obtained by *Suzaku*, H.E.S.S. and *Fermi* LAT, and modelling the NT spectra from high energy bands in the basis of the non-linear diffusive shock acceleration, and using the observed thickness of the X-ray filaments of the SNR, Zhang and Yang (2011) [106] concluded that the high-energy γ-ray emission from the SNR has a hadronic origin.

Using *Suzaku* observation data, Takahashi et al. (2008) [107] determined that the hard X-ray spectrum of the SW part of the SNR in the 12 – 40 keV energy band to be described by a PL with a $\Gamma \sim 3.2$. The NT featureless spectrum of the SNR is thought to arise from the gradually steepening high-energy part of the synchrotron radiation spectrum produced by TeV-scale electrons. These electrons are accelerated through the mechanism of DSA according to the study of Reynolds (1998) [108]. They also found that a simple PL fails to describe the spectral range of 0.4 – 40 keV, but using a PL with an exponential cut-off with high-energy cut-off $\varrho_c = 1.2 \pm 0.3$ keV, and hard index $\Gamma = 1.50 \pm 0.09$, they got satisfying spectral fit over the full bandpass.

Utilizing *Suzaku* observations, Tanaka et al. (2008) [109] detected hard X-rays up to 40 keV. The hard X-ray spectra are well described by the PL models with the photon indices of about 3.0. Furthermore, they compared the TeV γ-ray and X-ray surface brightness maps using H.E.S.S. and *Suzaku* XIS data, and showed strong correlation between TeV γ- ray and X-ray components.

Utilizing *XMM-Newton* observation data and comparing with γ-ray and radio observations, Acero et al. (2009) [110] showed that RX J1713.7–3946 allows to investigate particle acceleration at SNRs. It is part of the class of the SNRs dominated by the synchrotron radiation in X-rays. They found that one of the brightest arcs seen at 1.4 GHz is of thermal origin, and likely not associated with the remnant. On the other hand, they compared the radial profile in γ - and X-rays, and found that the X-ray emission comes more from the inside of the remnant rather than in γ-rays.

With high spectral-resolution observations of RX J1713.7–3946 in γ- and X-rays, Fan et al. (2010) [111] suggest, emission of this SNR is dominated by the particles accelerated near the shock front. They used a systematic study of four lepton models for the TeV emission with the Markov chain Monte Carlo method.

Performing magneto hydrodynamic numerical simulations of the shock interaction with atomic and molecular gas, the study of Sano et al. (2013) [112] concluded that RX J1713.7−3946 emits synchrotron X-rays with any thermal features in its spectra. All the major HI and CO clumps with mass $>50M_{\odot}$ interact with the shock waves in the SNR. These clumps are associated with the NT X-rays, which are enhanced within ~1 pc of the HI and CO peaks.

Due to their suggestion that "X-rays become bright around the dense cloud cores due to turbulence amplification of magnetic field", Sano et al. (2015) [113], concluded that the X-ray flux of the SNR shows improvement toward the dense regions of the ISM. They performed spectral analysis of the *Suzaku* archival data in the 0.4 − 12 keV range. On the other hand, they obtained that photon indices show large variation within the SNR in the range of 2.1 − 2.9, where it shows smallest values around the dense regions of cloud cores as well as toward diffuse regions with no molecular gas.

Utilizing *XMM-Newton* and *Suzaku* observation data of the central region of the SNR, Katsuda et al. (2015) [114] measured in their study that Mg/Ne, Si/Ne, and Fe/Ne ratios of 2.0 – 2.6, 1.5 – 2.0, and <0.05 solar, and this suggest that the progenitor star of RX J1713.7−3946 was a relatively low-mass star ($\lesssim 20M_{\odot}$). As compared with other CC SNRs, the mean blast-wave speed of the SNR is ~ 6000 km s^{-1} (with an age of 1600 yr and a radius of 9.6 pc), and it is relatively fast. Thus, they proposed that RX J1713.7−3946 is a result of a Type Ib/c supernova whose progenitor was a member of an interacting binary. For the first time from this SNR, they also detected clear X-ray line emission, including Mg Heα and Ne Lyα.

RX J1713.7−3946 emits strong synchrotron X-rays, which dominates the total X-ray flux in the SNR, and emits bright TeV γ-rays whose origin is still uncertain [100], [101]. Analysing the NW part of the remnant using *Suzaku* data, Sezer et al. (2016) [115] detected rapid variability in X-ray emission from the SNR, which indicates the magnetic field B ~ mG.

Analysing the *Chandra* data of the remnant, Tsuji et al. (2016) [116] showed that "the blast-wave shock speed at the NW shell is to be (3900 ± 300) (d/kpc) km s^{-1} with an estimated distance of d = 1 kpc, and the proper motions of other structures within the NW shell are significantly less than that". Their hydro dynamical analysis reveals that the age of the remnant is between the range of 1580 – 2100 yr. This age associates with the SN 393.

5.2.3.2 Background Estimation

The background region data for *Chandra* analysis, extracted from a circular source free area of 77.52 $arcmin^2$ for SW rim and 34.32 $arcmin^2$ for NW rim in the same FoV (Figure 5.11).

The background spectrum of RX J1713.7−3946 SW rim *Chandra* observations consist of the CXB, GRXE and LHB components. The spectrum was fitted with a model of [$Abs_{(CXB)}$ × $PL_{(CXB)}$ + $Abs_{(GRXE)}$ × ($apec_{(HP)}$ + $apec_{(CP)}$ + $PL_{(CM)}$) + $Abs_{(FE)}$ × (apec + apec)] as in the study [54], where the CXB component parameters were fixed with the parameters mentioned before in the background analysis method of Cas A. The second term is the GRXE component, which is represented by a 2-CIE model, a low-temperature plasma (kT_e ~ 1 keV) plus a high-temperature plasma (kT_e ~ 7 keV) [54], and also with a cold matter NT component. Because of RX J1713.7−3946 emission is under effect of the a high-temperature plasma (kT_e ~ 7 keV) of GRXE, careful background subtraction is required. Thus, particular attention to background subtraction was paid with reanalysing of the *Chandra* data. The third term is the absorbed foreground emission, which is represented with optically thin thermal plasmas and fixed component values as in the study of [54] ($N_{H(FE)}$ = 5.6 × 10^{21} cm^{-2}, kT = 0.09 keV and 0.59 keV). The background spectrum of RX J1713.7−3946 NW rim *Chandra* observations consist of the CXB, GRXE and FE components. The spectrum was fitted with a model of [$Abs_{(CXB)} \times PL_{(CXB)} + Abs_{(GRXE)} \times (apec_{(HP)} + apec_{(CP)} + PL_{(CM)}) + Abs_{(FE)} \times (apec + apec)$] as in the background modelling of the SW rim.

For the background modelling of both rims, to calculate the absorption parameter, *TBABS* model was used [60] and the hydrogen column density parameter of CXB component was fixed to 1.38×10^{22} cm^{-2} as in the study of [100]. This value was taken from study of [88]. The background spectrum was simulated with using the *FAKEIT* command in XSPEC, and subtracted from the source spectra. The best-fit parameters and spectra of the background regions for NW and SW rims are given in the Table 5.8 and Table 5.9, Figure 5.12 and Figure 5.13, respectively.

5.2.3.3 Spectral Fitting

Figure 5.11 shows *Chandra* X-ray images of the NW and SW rims of the SNR in the energy band of 0.5 − 7.0 keV. The images are binned with 4″ × 4″. Smoothing with a Gaussian kernel of $\sigma = 3''$ was applied.

Three spectral source regions were extracted from *Chandra* observation of the SW rim (as seen in Figure 5.11). In order to characterize the emission of specific regions, for the SW rim, two rectangular regions centred at the X-ray peak location with the area of 0.82 arcmin^2 and 0.97 arcmin^2 were selected, respectively. For the NW rim, three rectangular regions centred at the X-ray peak location with the area of 0.90 arcmin^2, 0.62 arcmin^2 and 0.91 arcmin^2 were selected, respectively. For spectral analysis, each of them were grouped with a minimum of 25 counts per bin. The spectra of selected regions are represented by the absorbed NT models *PL* or *SRCUT*. Absorbed *PL* model fitting gives three parameters: Absorption-corrected X-ray flux $F_{0.5-7keV}$ is used for adjusting the normalization parameter while fitting with the *SRCUT* model. Typical X-ray spectra are shown in Figure 5.14 and 5.15 for SW rim, Figure 5.16, 5.17 and 5.18 for NW rim, and the best-fit parameters for both NT models are shown in Table 5.10 and Table 5.11 for NW rim, Table 5.12 and 5.13 for SW rim for the BGD-1 and BGD-2 subtracted spectra, respectively. All errors indicate 90% confidence intervals.

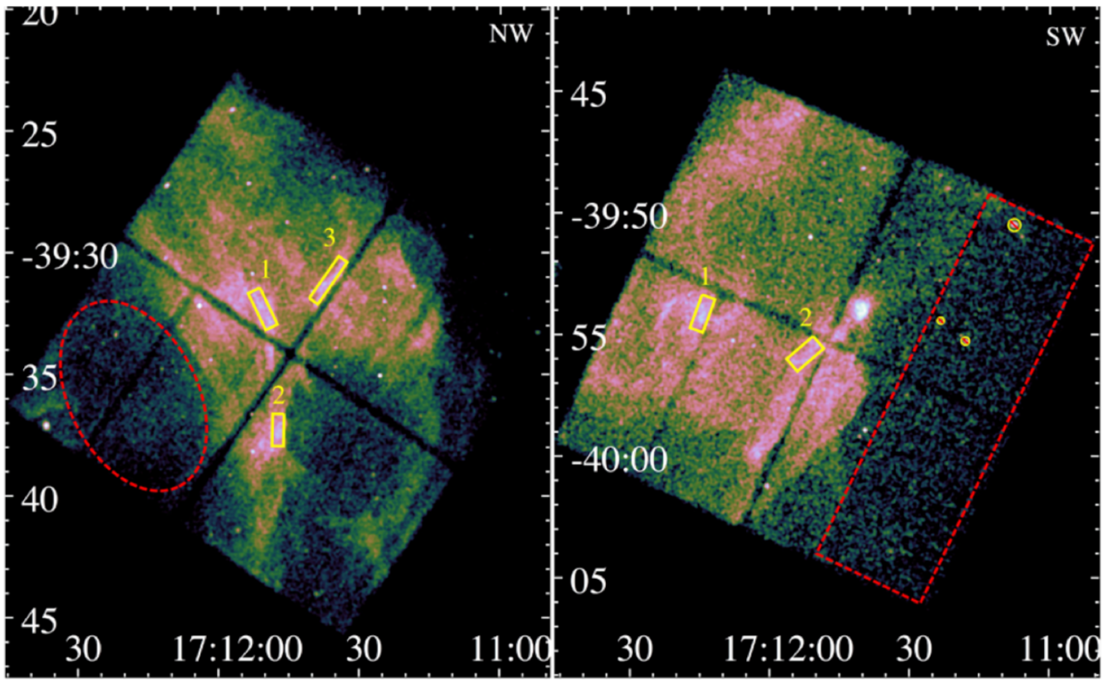

The source regions are given in numbered yellow solid rectangular areas, and the background region is chosen with the red dashed rectangular region where three circler emission regions were excluding from the background region during spectral analysis.

Figure 5.11 X-ray image of RX J1713.7–3946 with the source and background regions in the 05 − 7.0 keV energy band for the NW and SW rims.

5.2.3.4 Spectral Analysis Results of RX J1713.7–3946

RX J1713.7–3946 is an X-ray synchrotron emitting SNR [114], [118]. Due to obtain roll-off frequency to calculate maximum energy of electrons ($E_{max,e}$) with using the analysis methods described in previous section, background analysis was also aimed for a comparative approach to get sensitive values about synchrotron spectrum parameters. In accordance with these purposes, the background regions were modelled and their best-fit parameters are given in Table 5.8 and Table 5.9 and the spectra are in Figure 5.12 and Figure 5.13. Also, the spectra of selected source regions are shown in Figure 5.14 and 5.15 for SW rim, Figure 5.16, 5.17 and 5.18 for NW rim, and the best-fit parameters for both NT models are shown in Table 5.10 and Table 5.11 for NW rim, Table 5.12 and 5.13 for SW rim for the BGD-1 and BGD-2 subtracted spectra, respectively.

Table 5.8 Best-fit parameters for the background spectrum of the SW rim of RX J1713.7–3946.

Components	Parameters	Values
CXB	N_H (10^{22} cm^{-2}) ⊔	1.830 (fixed)
	Photon Index †	1.412 (fixed)
	S. B. (erg s^{-1} cm^{-2} arcmin^{-2}) †	5.410×10^{-15} (fixed)
FE	N_H (10^{22} cm^{-2}) ‡	0.56 (fixed)
	kT_e (keV) ‡	0.09 (fixed)
	norm (10^{-2} photons cm^{-2}s^{-1})	$0.167^{+0.018}_{-0.018}$
	kT_e (keV) ‡	0.59 (fixed)
	norm (10^{-2} photons cm^{-2} s^{-1})	$0.002^{+0.001}_{-0.001}$
GRXE	N_H (10^{22} cm^{-2})	$0.915^{+0.170}_{-0.154}$
	kT_e (keV) ⊔	1.0 (fixed) (LP)
	norm (10^{-2} photons cm^{-2}s^{-1})	$0.014^{+0.030}_{-0.014}$
	kT_e (keV) ⊔	7.0 (fixed) (HP)
	norm (10^{-2} photons cm^{-2}s^{-1})	$0.257^{+0.001}_{-0.001}$
	Photon Index *	2.00 (fixed) (CM)
	norm (photons cm^{-2}s^{-1}) *	$3.211^{+1.653}_{-1.598}$
	χ^2 / d.o.f.	461.25 / 438

†: [50] (S. B.: Surface Brightness in the 2 – 10 keV band). *: Flux in the 0.46 – 7.06 keV band [117]. ⊔: N_H(CXB) = 2 × N_H(GRXE) [54].

Table 5.9 Best-fit parameters for the background spectrum of the NW rim of RX J1713.7–3946.

Components	Parameters	Values
CXB	N_H (10^{22} cm^{-2}) ⊔	1.830 (fixed)
	Photon Index †	1.412 (fixed)
	S. B. (erg s^{-1} cm^{-2} arcmin^{-2}) †	5.410×10^{-15} (fixed)
FE	N_H (10^{22}cm^{-2}) ‡	0.56 (fixed)
	kT_e (keV) ‡	0.09 (fixed)
	norm (10^{-2} photons cm^{-2}s^{-1})	$8.847^{+0.015}_{-0.014}$
	kT_e (keV) ‡	0.59 (fixed)
	norm (10^{-3} photons cm^{-2}s^{-1})	$0.018^{+0.044}_{-0.018}$
GRXE	N_H (10^{22} cm^{-2})	$0.393^{+0.053}_{-0.018}$
	kT_e (keV) ⊔	2.0 (fixed) (LP)
	norm (photons cm^{-2}s^{-1})	$0.035^{+0.041}_{-0.030}$
	kT_e (keV) ⊔	7.0 (fixed) (HP)
	norm (10^{-2} photons cm^{-2}s^{-1})	$0.386^{+0.004}_{-0.004}$
	Photon Index *	2.00 (fixed) (CM)
	norm (10^{-2} photons cm^{-2}s^{-1}) *	$2.68^{+0.563}_{-0.580}$
	χ^2 / d.o.f.	531.71 / 438

†: [50] (S. B.: Surface Brightness in the 2 – 10 keV band). *: Flux in the 0.46 – 7.06 keV band [117]. ⊔: N_H(CXB) = 2 × N_H(GRXE) [54].

Table 5.10 Best-fit parameters for BGD-1 subtracted spectrum of selected emission region on the NW rim of RX J1713.7−3946 (1 − 5 keV).

Component	Parameter		Values	
		Source#1	Source#2	Source#3
Absorption	N_H (10^{22}cm^{-2})	$1.51^{+0.23}_{-0.22}$	$1.33^{+0.19}_{-0.18}$	$1.10^{+0.19}_{-0.18}$
POWER-LAW	Photon Index	$2.42^{+0.19}_{-0.19}$	$2.17^{+0.15}_{-0.15}$	$2.11^{+0.16}_{-0.17}$
	norm (10^{-3} photons cm^{-2}s^{-1})	$0.32^{+0.08}_{-0.06}$	$0.40^{+0.07}_{-0.07}$	$0.31^{+0.06}_{-0.05}$
	χ^2 / d.o.f.	109.70 / 109	177.42 / 149	128.06 / 135
Absorption	N_H (10^{22} cm^{-2})	$1.37^{+0.09}_{-0.08}$	$1.25^{+0.07}_{-0.07}$	$1.02^{+0.07}_{-0.07}$
SRCUT	Spectral Index(α)	0.60 (fixed)	0.60 (fixed)	0.60 (fixed)
	$\nu_{\text{roll-off}}$ (10^{17} Hz)	$2.53^{+0.16}_{-0.16}$	$6.32^{+0.44}_{-0.41}$	$8.87^{+0.80}_{-0.74}$
	Flux (10^{-13} ergs cm^{-2} s^{-1}) ‡	$3.52^{+0.14}_{-0.14}$	$5.84^{+0.24}_{-0.23}$	$5.11^{+0.23}_{-0.24}$
	χ^2 / d.o.f.	109.89 / 110	175.74 / 150	128.22 / 136

‡ Flux in 1 − 5 keV band.

Table 5.11 Best-fit parameters for BGD-2 subtracted spectrum of selected emission region on the NW rim of RX J1713.7−3946 (1 − 5 keV).

Component	**Parameter**		**Values**	
		Source#1	Source#2	Source#3
Absorption	N_H (10^{22}cm^{-2})	$1.54^{+0.23}_{-0.22}$	$1.34^{+0.18}_{-0.18}$	$1.12^{+0.19}_{-0.18}$
POWER-LAW	Photon Index	$2.47^{+0.19}_{-0.19}$	$2.20^{+0.15}_{-0.15}$	$2.15^{+0.16}_{-0.16}$
	norm (10^{-3} photons cm^{-2}s^{-1})	$0.34^{+0.09}_{-0.07}$	$0.42^{+0.07}_{-0.07}$	$0.33^{+0.07}_{-0.06}$
	χ^2 / d.o.f.	109.30 / 109	180.04 / 149	133.45 / 135
Absorption	N_H (10^{22} cm^{-2})	$1.41^{+0.09}_{-0.08}$	$1.30^{+0.07}_{-0.07}$	$1.06^{+0.07}_{-0.07}$
SRCUT	Spectral Index (α)	0.60 (fixed)	0.60 (fixed)	0.60 (fixed)
	$\nu_{\text{roll-off}}$ (10^{17} Hz)	$2.10^{+0.13}_{-0.12}$	$4.74^{+0.30}_{-0.29}$	$6.55^{+0.53}_{-0.48}$
	Flux (10^{-13} ergs cm^{-2} s^{-1}) ‡	$3.51^{+0.14}_{-0.14}$	$5.83^{+0.21}_{-0.21}$	$5.07^{+0.20}_{-0.23}$
	χ^2 / d.o.f.	109.70 / 110	178.70 / 150	133.81 / 136

‡ Flux in 1 − 5 keV band.

Table 5.12 Best-fit parameters for BGD-1 subtracted spectrum of selected emission region on the SW rim of RX J1713.7−3946 (0.5 − 7 keV).

Component	**Parameter**	**Values**	**Values**
		Source#1	Source#2
Absorption	N_H (10^{22} cm^{-2})	$1.37^{+0.22}_{-0.20}$	$1.30^{+0.19}_{-0.18}$
POWER-LAW	Photon Index	$2.22^{+0.19}_{-0.19}$	$2.51^{+0.20}_{-0.19}$
	norm (10^{-3} photons cm^{-2}s^{-1})	$0.39^{+0.09}_{-0.08}$	$0.43^{+0.01}_{-0.08}$
	χ^2 / d.o.f.	44.05 / 56	47.13 / 56
Absorption	N_H (10^{22} cm^{-2})	$1.26^{+0.09}_{-0.08}$	$1.16^{+0.08}_{-0.08}$
SRCUT	Spectral Index (α)	0.60 (fixed)	0.60 (fixed)
	$\nu_{\text{roll-off}}$ (10^{17} Hz)	$6.30^{+0.70}_{-0.65}$	$2.09^{+0.16}_{-0.15}$
	Flux (10^{-13} ergs cm^{-2} s^{-1}) ‡	$6.77^{+0.39}_{-0.47}$	$5.68^{+0.35}_{-0.27}$
	χ^2 / d.o.f.	43.26 / 57	48.02 / 57

‡ Flux in 0.5 − 7 keV band.

Table 5.13 Best-fit parameters for BGD-2 subtracted spectrum of selected emission region on the SW rim of RX J1713.7−3946 (0.5 − 7 keV).

Component	Parameter	Values	Values
		Source#1	Source#2
Absorption	N_H (10^{22} cm^{-2})	$1.34^{+0.22}_{-0.20}$	$1.28^{+0.19}_{-0.18}$
POWER-LAW	Photon Index	$2.17^{+0.19}_{-0.18}$	$2.48^{+0.19}_{-0.18}$
	norm (10^{-3} photons $cm^{-2}s^{-1}$)	$0.37^{+0.09}_{-0.07}$	$0.42^{+0.01}_{-0.08}$
	χ^2 / d.o.f.	44.80 / 56	49.04 / 56
Absorption	N_H (10^{22} cm^{-2})	$1.23^{+0.09}_{-0.08}$	$1.17^{+0.08}_{-0.08}$
SRCUT	Spectral Index (α)	0.60 (fixed)	0.60 (fixed)
	$\nu_{roll\text{-}off}$ (10^{17} Hz)	$7.69^{+0.92}_{-0.84}$	$2.06^{+0.15}_{-0.15}$
	Flux (10^{-13} ergs cm^{-2} s^{-1}) ‡	$6.87^{+0.35}_{-0.49}$	$5.72^{+0.33}_{-0.38}$
	χ^2 / d.o.f.	43.59 / 57	50.76 / 57

‡ Flux in 0.5 − 7 keV band.

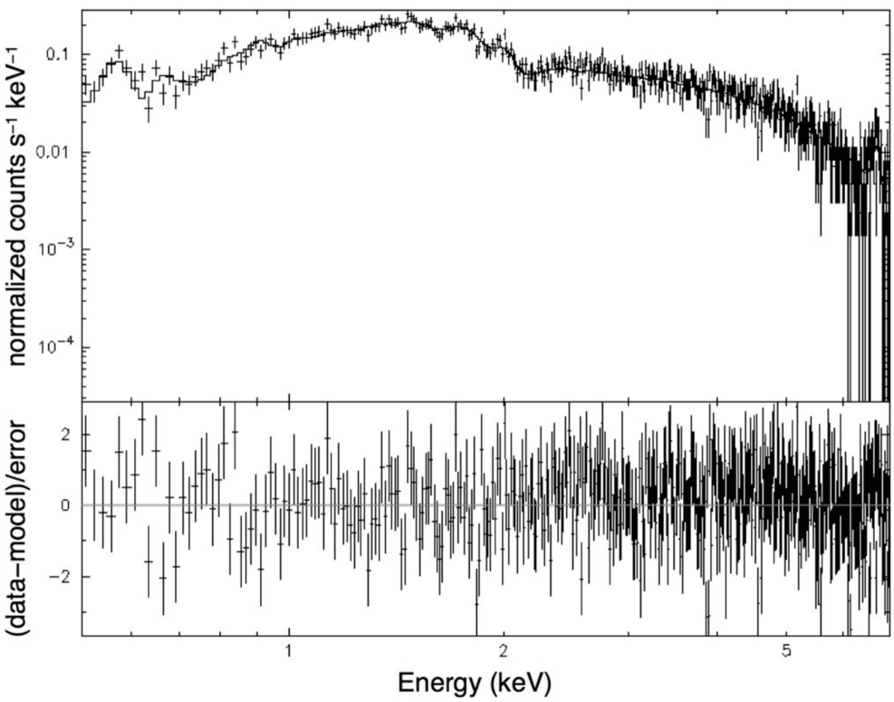

Figure 5.12 Modelled background spectrum of the selected region SW rim of RX J1713.7–3946.

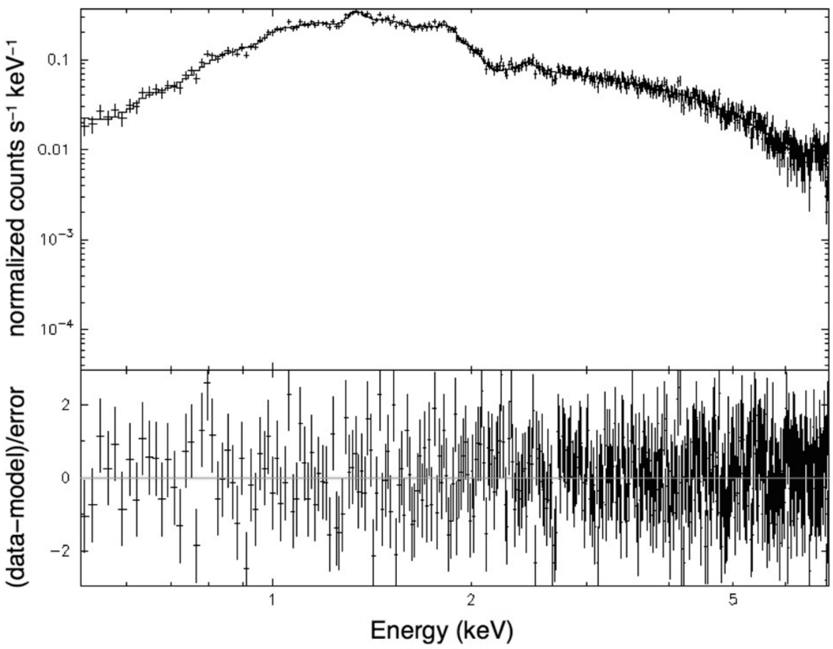

Figure 5.13 Modelled background spectrum of the selected region NW rim of RX J1713.7–3946.

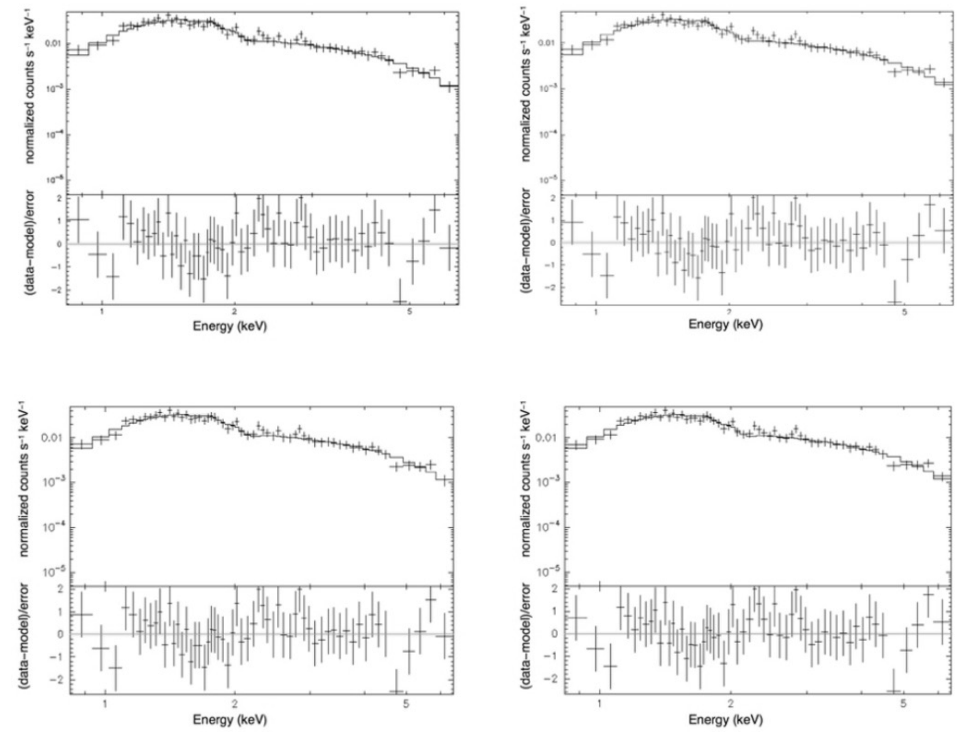

Left panels show the BGD-1 subtracted spectra. Right panels show the BGD-2 subtracted spectra, each modelled with *PL* and *SRCUT*.

Figure 5.14 BGD-1 (left) and BGD-2 (right) subtracted spectra of the region#1 on the SW rim.

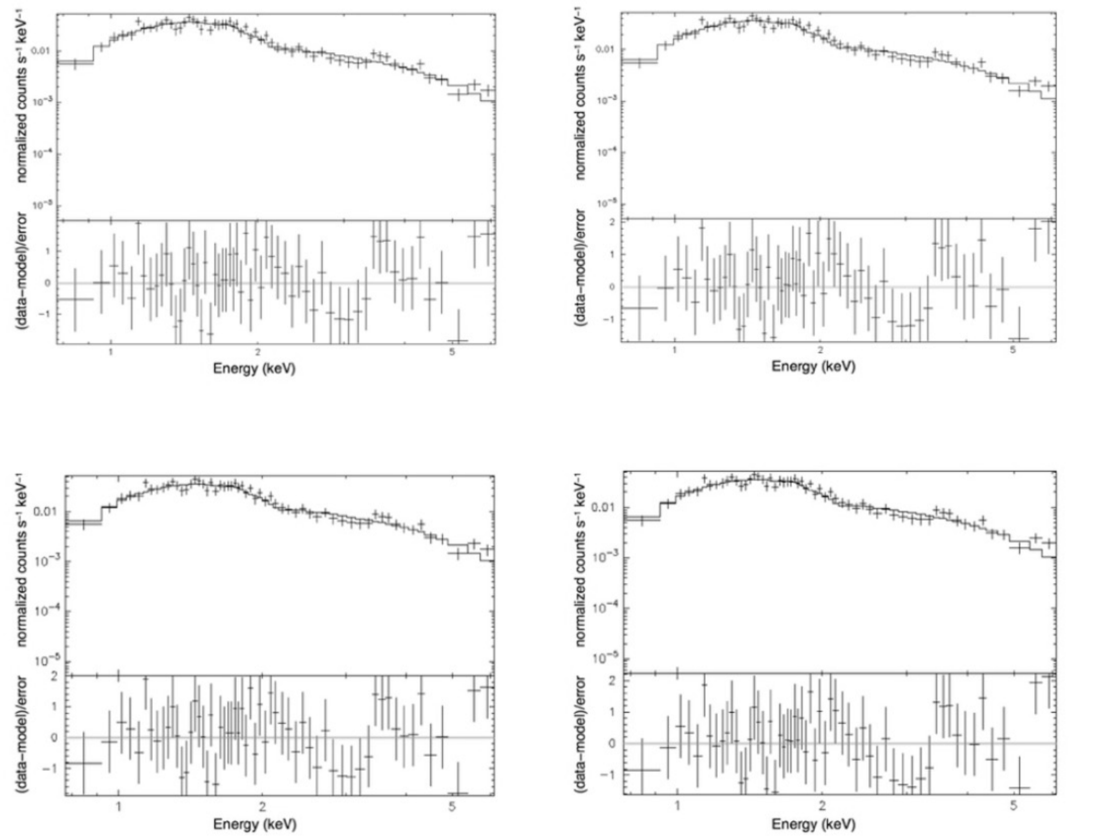

Left panels show the BGD-1 subtracted spectra. Right panels show the BGD-2 subtracted spectra, each modelled with *PL* and *SRCUT*.

Figure 5.15 BGD-1 (left) and BGD-2 (right) subtracted spectra of the region#2 on the SW rim.

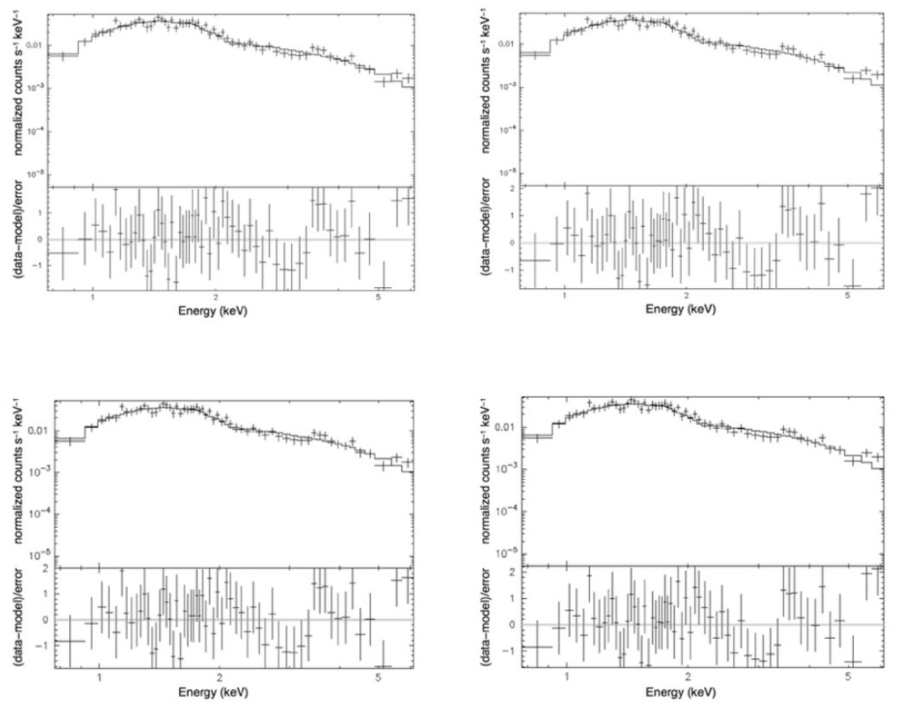

Left panels show the BGD-1 subtracted spectra. Right panels show the BGD-2 subtracted spectra, each modelled with *PL* and *SRCUT*.

Figure 5.16 BGD-1 (left) and BGD-2 (right) subtracted spectra of the region#1 on the NW rim.

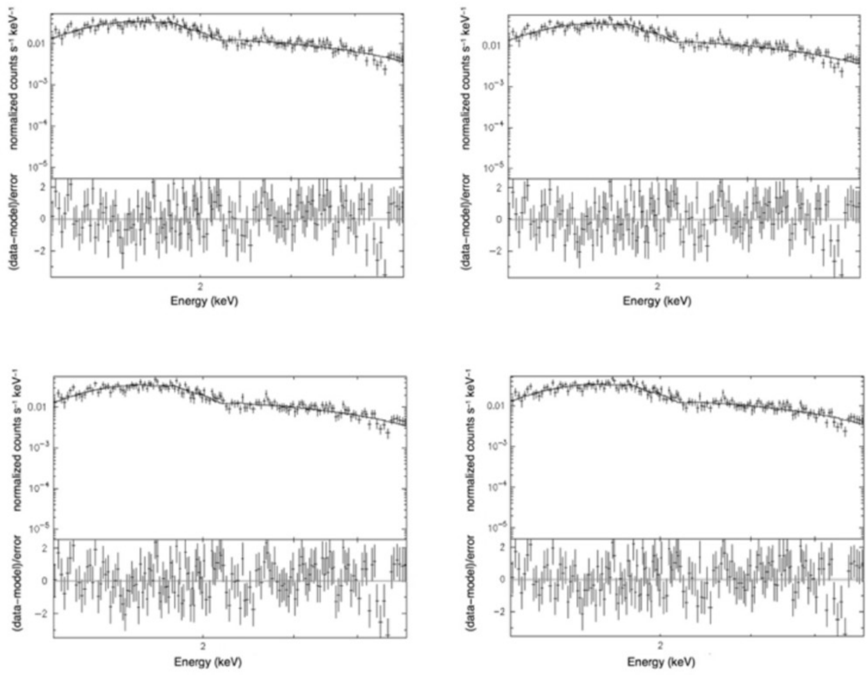

Left panels show the BGD-1 subtracted spectra. Right panels show the BGD-2 subtracted spectra, each modelled with *PL* and *SRCUT*.

Figure 5.17 BGD-1 (left) and BGD-2 (right) subtracted spectra of the region#2 on the SW rim.

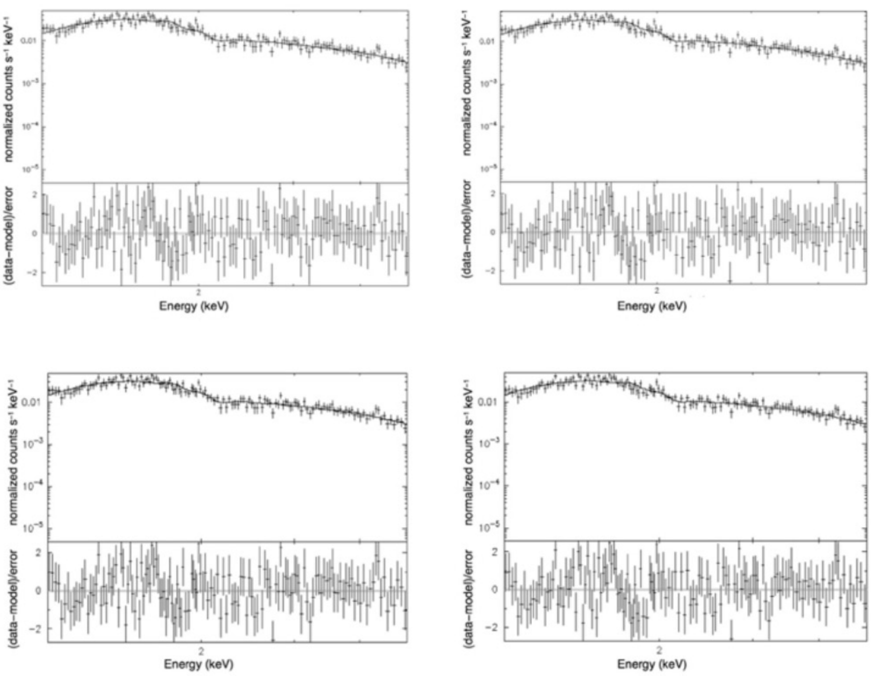

Left panels show the BGD-1 subtracted spectra. Right panels show the BGD-2 subtracted spectra, each modelled with *PL* and *SRCUT*.

Figure 5.18 BGD-1 (left) and BGD-2 (right) subtracted spectra of the region#3 on the SW rim.

5.2.4 SN 1006

5.2.4.1 Literature

Utilizing the *XMM-Newton* observation data, Acero et al. (2007) [119] studied the PS thermal emission in the NW and the SE rims of SN 1006. They focused on the thermal emission dominated NW and SE rims of the remnant. They modelled the PS thermal emission, and used a plane-parallel shock plasma model plus another component for the ejecta. They estimated the density in the SE rim whose low value of ~0.05 cm^{-3}, which represents the rest of the remnant. Also, on the NW region, the remnant seems to be encountering a denser ISM. They concluded that in the SE region, the shock speed is ~4900 km s^{-1}, and 2890 km s^{-1} in the NW region, where the density is higher, causing the expansion to slow down.

In their *Suzaku* analysis Yamaguchi et al. (2008) [120], through its brightness in Fe-K_{α}, selected a region in the southern part of SN 1006. They fitted the spectrum with a combined model of three NEI and a PL component. Hereby, they found the low-$n_e t$ plasma (~8×10^{8} cm^{-3} s) highly overabundant in heavy elements, and or the first time found Fe-K_α lines. They suggested that the abundance pattern coincide with the ejecta properties of Type Ia SN. The abundance of the medium-n_et (~6×10^9 cm^{-3} s) plasma is assumed to be solar, and they associated this component with the shocked ISM. Also they concluded for this plasma that K_α lines of OVII and OVIII appear to dominate the thermal emission from the SNR. The high-n_et plasma (~10^{10} cm^{-3} s) is overabundant in medium elements, like Mg, Si, and S, but heavy element like Fe. Their interpretation for this situation is this high-n_et plasma has an ejecta origin, and the composition is dominated by lower atomic number species. They interpreted that the profile of first and second ionisation parameters suggest Fe was heated by RS more recently than the other ejecta elements. Besides, the third thermal component was associated with the emission from the ISM. They indicated that the electron temperature which is about 0.5 keV is lower than their expectation from the shock velocity, and their suggestion for this condition is that a lack of collision-less electron heating at the FS. They implied the extreme non-equilibrium state, and extremely low ionisation parameter as they are due to the low density of the ambient medium.

Miceli et al. (2009) [121] studied with *XMM-Newton*, and described the emission at the rims of the shell by a mixture of thermal emission in non-equilibrium of ionisation and by a NT emission. They concluded that thermal emission in the SNR may be associated with the shocked ejecta, and the chemical composition and the temperature of it are not homogeneous. Also, they found lower Si/O abundances and lower temperatures in the NW rim than the SE rim. Besides, they found the emission at the bright limbs is mainly correlated with the NT component.

In the *XMM-Newton* study of Miceli et al. (2012) [122], they found an azimuthal trend of the ISM PS density. This is a matter of the CR acceleration at the shock front of the remnant, and this situation modifies the shock compression ratio by particle acceleration.

In the study that includes *XMM-Newton* archival data of the bright NW oxygen knot, Broersen et al. (2013) [123] used the RGS to measure the thermal broadening of the OVII line triplet. They measured the line broadening as $\sigma_e = 2.4 \pm 0.3$ eV, corresponding to an oxygen temperature of about 275 keV, and they obtained an electron temperature of ~1.35 keV. They also found evidence of a bow shock emits X-ray synchrotron emission.

Analysing a set of *XMM-Newton* archival data of SN 1006, Miceli et al. (2013) [124] studied the shape of the cut-off of the synchrotron radiation in the NT limbs, and they found that the *SRCUT* model does not correctly describe the observed spectra.

SN 1006 indicates a bilateral shape with two opposite bright limbs. Interpretation of Yu et al. (2015) [125] for this situation is that the circumstellar medium around the SNR is more uniform than the other SNRs with variating complex shapes. They generated the filamentary and knotty structure of the remnant in their three-dimensional (3D) magneto hydrodynamic simulations study. They concluded with these simulations that the big bump at the NE rim of the SNR is formed by the cavity in the background medium.

Miceli et al. (2016) [126] performed 3D magneto hydrodynamic simulations modelling to understand interaction of the remnant with the ambient cloud, and the evolution of it. They found that the pre-shock density of the cloud is of about 0.5 cm^{-3}. They also synthesized the hadronic and the leptonic γ-ray emission from the models. They concluded that SW rim of the SNR is interacting with a dense ambient cloud, a possible region for the hadronic emission.

5.2.4.2 Background Estimation

SN 1006 is above the Galactic plane (l = 327$^{\circ}_{.}$4109, b = +14$^{\circ}_{.}$4674). Thus, the possible contamination of the GRXE is negligible [87].

For all the rims, the background emission spectra were chosen from source free regions in the same FoV (Figure 5.19), and were fitted with the assumption that the emission contains CXB, and also LHB. The background spectra were fitted with a model of [$Abs_{(CXB)} \times PL_{(CXB)} + apec_{(LHB)}$], where the *APEC* represents the LHB component, while an absorbed PL represents the CXB emission defined with a photon index of 1.41, and a surface brightness value of 5.41×10^{-15} erg s^{-1} cm^{-2} $arcmin^{-2}$ in the 2 − 10 keV band [50]. The column density was fixed to 6.8×10^{20} cm^{-2} following the HI observation by [127]. Next, the background spectrum was simulated using *FAKEIT* command, and subtracted from the source spectrum. The best-fit parameters and the spectra of the background regions are shown in Table 5.14, 5.15, 5.16, 5.17 and 5.18, Figure 5.20, 5.21, 5.22, 5.23 and 5.24, respectively.

5.2.4.3 Spectral Fitting

Figure 5.19 shows ACIS-I and ACIS-S RGB mosaicked images of data of ObsId: 732, 1959, 3838, 4385, 4394, 9107, 13737, 13738, 13739, 13741, 13742, 13743, 14423, 14424, 14435 (which include NW, S, SE, SW and W rims) of SN 1006 in various energy bands (Red: 0.50 − 0.91 keV, Green: 0.91 − 1.34 keV, Blue: 1.34 − 3.00 keV). In order to characterize the emission of specific regions, for the mentioned rims of the SNR, the regions centred at the source location. All these regions are shown by the solid boxes and ellipses in the figure below (Figure 5.19), and they were selected through their X-ray peak emission.

Figure 5.19 shows ACIS-I and ACIS-S images of NW, S, SE, SW, and W rims of SN 1006. In order to characterize the emission of specific regions, for the NW rim, one elliptical and two rectangular regions centred at the X-ray peak location with the area of 1.24 $arcmin^2$, 0.59 $arcmin^2$ and 0.77 $arcmin^2$ were selected, respectively. For the S rim, two rectangular regions centred at the X-ray peak location with the area of 0.30 $arcmin^2$ and 0.93 $arcmin^2$ were selected, respectively. For the SE rim, one rectangular region centred at the X-ray peak location with the area of 1.50 $arcmin^2$ was selected. For the SW rim, two rectangular regions centred at the X-ray peak location with the area of 0.81 $arcmin^2$ and 0.92 $arcmin^2$ were selected, respectively. For the W rim, three elliptical regions centred at the X-ray peak location with the area of 0.93 $arcmin^2$, 0.34 $arcmin^2$ and 0.93 $arcmin^2$ were selected, respectively. All these regions are shown by the solid ellipses and boxes in the Figure 5.19, respectively. The spectral source regions were extracted from these regions. They were grouped with a minimum of 25 counts bin^{-1}. The X-ray spectra of selected regions are well represented by the absorbed NT models *PL* or *SRCUT*. On the NW rim, there is a thermal-emitting region (region#3), solely, is was fitted with *VNEI* model in XSPEC. Absorbed *PL* model fitting gives three parameters: Absorption-corrected X-ray flux $F_{0.5-7keV}$ is used for adjusting the normalization parameter while fitting with the *SRCUT* model. For all the rims, typical X-ray spectra are shown in Figure 5.25 − 5.35 and the best-fit parameters for both NT models are shown in Table 5.19 − 5.28 for BGD-1 and BGD-2 subtracted spectra, respectively.

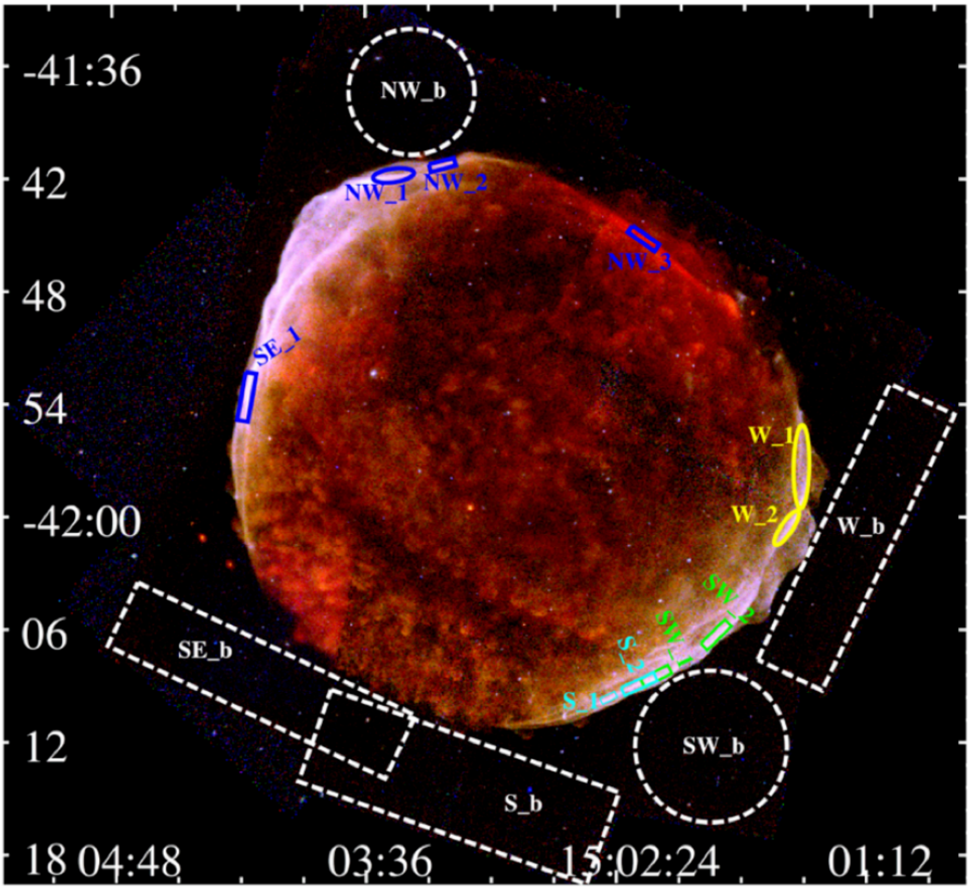

The source regions are given in numbered yellow, cyan, blue, and green solid rectangular areas, and the background regions are chosen with the white dashed rectangular and circular regions.

Figure 5.19 RGB image of the SNR SN 1006 with the source and background regions for all the rims.

5.2.4.4 Spectral Analysis Results of SN 1006

SN 1006 is an X-ray synchrotron emitting SNR [119], [128]. Due to obtain roll-off frequency to calculate maximum energy of electrons ($E_{max,e}$) with using the analysis methods described in previous section, background analysis was also aimed for a comparative approach to get sensitive values about synchrotron spectrum parameters. In accordance with these purposes, the background regions were modelled and their best-fit parameters are given in Table 5.14 − 5.18 and the spectra are in Figure 5.20 − 5.24. Also, the spectra of the selected source regions are shown in Figure 5.25 − 5.35 and the best-fit parameters for both NT models are shown in Table 5.19 − 5.28 for BGD-1 and BGD-2 subtracted spectra, respectively. All errors indicate 90% confidence intervals.

Table 5.14 Best-fit parameters for the background spectrum of the NW rim of SN 1006.

Components	Parameters	Values
CXB	N_H (10^{22} cm^{-2}) ‡	0.068 (fixed)
	Photon Index †	1.412 (fixed)
	S. B. (erg s^{-1} cm^{-2} arcmin^{-2}) †	5.410×10^{-15} (fixed)
LHB	kT_e (keV)	$0.987^{+0.014}_{-0.014}$
	norm (10^{-2} photons cm^{-2} s^{-1})	$0.025^{+0.001}_{-0.001}$
	χ^2 / d.o.f.	388.56 / 442

†: [50] (S. B.: Surface Brightness in the 2 – 10 keV band). ‡: [127].

Table 5.15 Best-fit parameters for the background spectrum of the S rim of SN 1006.

Components	Parameters	Values
CXB	N_H (10^{22} cm^{-2}) ‡	0.068 (fixed)
	Photon Index †	1.412 (fixed)
	S. B. (erg s^{-1} cm^{-2} arcmin^{-2}) †	5.410×10^{-15} (fixed)
LHB	kT (keV)	$0.917^{+0.020}_{-0.021}$
	norm (10^{-2} photons cm^{-2} s^{-1})	$0.025^{+0.001}_{-0.001}$
	χ^2 / d.o.f.	554.14 / 442

†: [50] (S. B.: Surface Brightness in the 2 – 10 keV band). ‡: [127].

Table 5.16 Best-fit parameters for the background spectrum of the SE rim of SN 1006.

Components	Parameters	Values
CXB	N_H (10^{22} cm^{-2}) ‡	0.068 (fixed)
	Photon Index †	1.412 (fixed)
	S. B. (erg s^{-1} cm^{-2} arcmin^{-2}) †	5.410×10^{-15} (fixed)
LHB	kT_e (keV)	$0.945^{+0.020}_{-0.021}$
	norm (10^{-2} photons cm^{-2} s^{-1})	$0.017^{+0.001}_{-0.001}$
	χ^2 / d.o.f.	528.73 / 442

†: [50] (S. B.: Surface Brightness in the 2 – 10 keV band). ‡: [127].

Table 5.17 Best-fit parameters for the background spectrum of the SW rim of SN 1006.

Components	Parameters	Values
CXB	N_H (10^{22} cm^{-2}) ‡	0.068 (fixed)
	Photon Index †	1.412 (fixed)
	S. B. (erg s^{-1} cm^{-2} arcmin^{-2}) †	5.410×10^{-15} (fixed)
LHB	kT_e (keV)	$0.951^{+0.019}_{-0.019}$
	norm (10^{-2} photons cm^{-2} s^{-1})	$0.018^{+0.001}_{-0.001}$
	χ^2 / d.o.f.	518.23 / 442

†: [50] (S. B.: Surface Brightness in the 2 – 10 keV band). ‡: [127].

Table 5.18 Best-fit parameters for the background spectrum of the W rim of SN 1006.

Components	Parameters	Values
CXB	N_H (10^{22} cm^{-2}) ‡	0.068 (fixed)
	Photon Index †	1.412 (fixed)
	S. B. (erg s^{-1} cm^{-2} arcmin^{-2}) †	5.410×10^{-15} (fixed)
LHB	kT_e (keV)	$0.973^{+0.018}_{-0.018}$
	norm (10^{-2} photons cm^{-2} s^{-1})	$0.035^{+0.001}_{-0.002}$
	χ^2 / d.o.f.	373 / 442

†: [50] (S. B.: Surface Brightness in the 2 – 10 keV band). ‡: [127].

Table 5.19 Best-fit parameters for BGD-1 subtracted spectrum of selected emission region on the NW rim of SN 1006 (0.5 – 5 keV).

Components	**Parameters**	**Values**	**Values**
		Source#1	Source#2
Absorption	N_H (10^{21} cm^{-2})	$0.94^{+0.03}_{-0.03}$	$1.80^{+0.31}_{-0.30}$
POWER-LAW	Photon Index	$2.72^{+0.08}_{-0.08}$	$2.91^{+0.11}_{-0.11}$
	norm (10^{-3} photons cm^{-2}s^{-1})	$0.63^{+0.04}_{-0.04}$	$0.29^{+0.21}_{-0.20}$
	χ^2 / d.o.f.	143.06 / 157	140.89 / 121
Absorption	N_H (10^{21} cm^{-2})	$0.30^{+0.09}_{-0.08}$	$1.10^{+0.13}_{-0.12}$
SRCUT	Spectral Index (α)	0.60 (fixed)	0.57 (fixed)
	$\nu_{roll\text{-}off}$ (10^{16} Hz)	$7.03^{+0.16}_{-0.16}$	$4.44^{+0.12}_{-0.12}$
	Flux (10^{-13} ergs cm^{-2} s^{-1}) ‡	$15.31^{+0.30}_{-0.34}$	$5.62^{+0.09}_{-0.09}$
	χ^2 / d.o.f.	143.06 / 157	132.19 / 122

‡ Flux in 0.5 − 5 keV band.

Table 5.20 Best-fit parameters for BGD-2 subtracted spectrum of selected emission region on the NW rim of SN 1006 (0.5 − 5 keV).

Components	**Parameters**	**Values**	**Values**
		Source#1	Source#2
Absorption	N_H (10^{21} cm^{-2})	$0.19^{+0.10}_{-0.10}$	$1.26^{+0.29}_{-0.28}$
POWER-LAW	Photon Index	$2.45^{+0.07}_{-0.07}$	$2.67^{+0.09}_{-0.09}$
	norm (10^{-3} photons cm^{-2}s^{-1})	$0.55^{+0.03}_{-0.03}$	$0.26^{+0.02}_{-0.02}$
	χ^2 / d.o.f.	149.68 / 157	139.83 / 121
Absorption	N_H (10^{21} cm^{-2})	$0.03^{+0.01}_{-0.01}$	$0.89^{+0.12}_{-0.12}$
SRCUT	Spectral Index (α)	0.57 (fixed)	0.57 (fixed)
	$\nu_{roll\text{-}off}$ (10^{16} Hz)	$11.84^{+0.31}_{-0.28}$	$6.68^{+0.19}_{-0.19}$
	Flux (10^{-13}ergs cm^{-2} s^{-1}) ‡	$16.36^{+0.31}_{-0.30}$	$5.97^{+0.09}_{-0.08}$
	χ^2 / d.o.f.	151.27 / 158	139.83 / 121

‡ Flux in 0.5 − 5 keV band.

Table 5.21 Best-fit parameters for BGD-1 subtracted spectrum of selected emission region on the S rim of SN 1006. The energy ranges are 0.5 − 5 keV range for Source#1, and 1 − 5 keV for Source#2.

Components	**Parameters**	**Values**	**Values**
		Source#1	Source#2
Absorption	N_H (10^{21} cm^{-2})	$1.38^{+0.68}_{-0.63}$	$2.30^{+1.06}_{-1.04}$
POWER-LAW	Photon Index	$2.60^{+0.14}_{-0.13}$	$2.90^{+0.12}_{-0.12}$
	norm (10^{-3} photons cm^{-2}s^{-1})	$0.20^{+0.03}_{-0.02}$	$0.84^{+0.01}_{-0.01}$
	χ^2 / d.o.f.	89.28 / 96	129.20 / 131
Absorption	N_H (10^{21}cm^{-2})	$0.80^{+0.64}_{-0.63}$	$0.70^{+0.23}_{-0.23}$
SRCUT	Spectral Index (α)	0.57 (fixed)	0.57 (fixed)
	$\nu_{roll\text{-}off}$ (10^{16} Hz)	$9.37^{+0.30}_{-0.25}$	$5.93^{+0.10}_{-0.11}$
	Flux (10^{-13} ergs cm^{-2} s^{-1}) ‡	$4.55^{+0.24}_{-0.27}$	$10.05^{+0.41}_{-0.32}$
	χ^2 / d.o.f.	83.10 / 97	129.23 / 132

‡ Flux in 0.5 − 5 keV range for Source#1 and 1 − 5 keV for Source#2.

Table 5.22 Best-fit parameters for BGD-2 subtracted spectrum of selected emission region on the S rim of SN 1006. The energy ranges are 0.5 − 5 keV range for Source#1, and 1 − 5 keV for Source#2.

Components	**Parameters**	**Values**	**Values**
		Source#1	Source#2
Absorption	N_H (10^{21} cm^{-2})	$1.12^{+0.66}_{-0.61}$	$1.97^{+1.04}_{-1.02}$
POWER-LAW	Photon Index	$2.53^{+0.13}_{-0.12}$	$2.83^{+0.12}_{-0.12}$
	norm (10^{-3} photons cm^{-2}s^{-1})	$0.19^{+0.02}_{-0.02}$	$0.80^{+0.01}_{-0.01}$
	χ^2 / d.o.f.	90.03 / 96	131.95 / 131
Absorption	N_H (10^{21} cm^{-2})	$0.71^{+0.28}_{-0.27}$	$0.34^{+0.02}_{-0.02}$
SRCUT	Spectral Index (α)	0.57 (fixed)	0.57 (fixed)
	$\nu_{roll\text{-}off}$ (10^{16} Hz)	$10.70^{+0.49}_{-0.48}$	$7.25^{+0.20}_{-0.20}$
	Flux (10^{-13} ergs cm^{-2} s^{-1}) ‡	$4.64^{+0.18}_{-0.27}$	$10.27^{+0.37}_{-0.31}$
	χ^2 / d.o.f.	80.85 / 97	132.64 / 132

‡ Flux in 0.5 − 5 keV range for Source#1 and 1 − 5 keV for Source#2.

Table 5.23 Best-fit parameters for BGD-1 subtracted spectrum of selected emission region on the SE rim of SN 1006 (1 − 5 keV).

Components	**Parameters**	**Values**
		Source#1
Absorption	N_H (10^{21}cm^{-2})	$4.19^{+0.73}_{-0.72}$
POWER-LAW	Photon Index	$2.95^{+0.08}_{-0.08}$
	norm (10^{-3} photons cm^{-2}s^{-1})	$1.54^{+0.14}_{-0.13}$
	χ^2 / d.o.f.	186.21 / 177
Absorption	N_H (10^{21} cm^{-2})	$2.48^{+0.27}_{-0.27}$
SRCUT	Spectral Index (α)	0.57 (fixed)
	$\nu_{\text{roll-off}}$ (10^{16} Hz)	$5.42^{+0.10}_{-0.10}$
	Flux (10^{-13}ergs cm^{-2}s^{-1}) ‡	$16.23^{+0.41}_{-0.39}$
	χ^2 / d.o.f.	187.56 / 175

‡ Flux in 1 − 5 band.

Table 5.24 Best-fit parameters for BGD-2 subtracted spectrum of selected emission region on the SE rim of SN 1006 (1 − 5 keV).

Components	**Parameters**	**Values**
		Source#1
Absorption	N_H (10^{21} cm^{-2})	$3.94^{+0.72}_{-0.71}$
POWER-LAW	Photon Index	$2.89^{+0.08}_{-0.08}$
	norm (10^{-3} photons cm^{-2} s^{-1})	$1.48^{+0.13}_{-0.12}$
	χ^2 / d.o.f.	185.44 / 177
Absorption	N_H (10^{21} cm^{-2})	$2.21^{+0.27}_{-0.26}$
SRCUT	Spectral Index (α)	0.57 (fixed)
	$\nu_{\text{roll-off}}$ (10^{16} Hz)	$6.36^{+0.12}_{-0.12}$
	Flux (10^{-13} ergs cm^{-2} s^{-1}) ‡	$16.58^{+0.38}_{-0.32}$
	χ^2 / d.o.f.	187.12 / 175

‡ Flux in 1 − 5 band.

Table 5.25 Best-fit parameters for BGD-1 subtracted spectrum of selected emission region on the SW rim of SN 1006 ($1-5$ keV).

Components	Parameters	Values	Values
		Source#1	Source#2
Absorption	N_H (10^{21} cm^{-2})	$3.06^{+0.82}_{-0.80}$	$3.47^{+0.76}_{-0.75}$
POWER-LAW	Photon Index	$2.77^{+0.10}_{-0.10}$	$2.84^{+0.09}_{-0.09}$
	norm (10^{-3} photons cm^{-2} s^{-1})	$0.68^{+0.07}_{-0.07}$	$0.90^{+0.13}_{-0.12}$
	χ^2 / d.o.f.	153.20 / 150	177.63 / 177
Absorption	N_H (10^{21} cm^{-2})	$1.74^{+0.30}_{-0.30}$	$1.91^{+0.28}_{-0.27}$
SRCUT	Spectral Index (α)	0.57 (fixed)	0.57 (fixed)
	$\nu_{\text{roll-off}}$ (10^{16} Hz)	$7.69^{+0.19}_{-0.18}$	$6.92^{+0.15}_{-0.15}$
	Flux (10^{-13} ergs cm^{-2} s^{-1}) ‡	$8.60^{+0.10}_{-0.19}$	$10.65^{+0.31}_{-0.27}$
	χ^2 / d.o.f.	155.90 / 151	181.01 / 162

‡ Flux in $1-5$ band.

Table 5.26 Best-fit parameters for BGD-2 subtracted spectrum of selected emission region on the SW rim of SN 1006 ($1-5$ keV).

Components	Parameters	Values	Values
		Source#1	Source#2
Absorption	N_H (10^{21} cm^{-2})	$4.80^{+1.97}_{-2.02}$	$3.28^{+0.74}_{-0.73}$
POWER-LAW	Photon Index	$3.11^{+0.39}_{-0.39}$	$2.78^{+0.09}_{-0.09}$
	norm (10^{-3} photons cm^{-2} s^{-1})	$0.88^{+0.30}_{-0.22}$	$0.88^{+0.08}_{-0.08}$
	χ^2 / d.o.f.	150.59 / 149	175.72 / 161
Absorption	N_H (10^{21} cm^{-2})	$1.49^{+0.30}_{-0.30}$	$3.92^{+0.29}_{-0.29}$
SRCUT	Spectral Index (α)	0.57 (fixed)	0.57 (fixed)
	$\nu_{\text{roll-off}}$ (10^{16} Hz)	$9.11^{+0.23}_{-0.23}$	$3.92^{+0.07}_{-0.07}$
	Flux (10^{-13}ergs cm^{-2}s^{-1}) ‡	$8.78^{+0.20}_{-0.30}$	$10.64^{+0.24}_{-0.22}$
	χ^2 / d.o.f.	156.57 / 151	215.81 / 162

‡ Flux in $1-5$ band.

Table 5.27 Best-fit parameters for BGD-1 subtracted spectrum of selected emission region on the W rim of SN 1006 (1 − 5 keV).

Components	Parameters		Values	
		Source#1	Source#2	Source#3
Absorption	N_H (10^{21} cm^{-2})	$3.67^{+0.74}_{-0.73}$	$2.88^{+1.07}_{-1.04}$	$3.52^{+1.09}_{-1.06}$
POWER-LAW	Photon Index	$2.90^{+0.09}_{-0.08}$	$2.75^{+0.13}_{-0.13}$	$2.84^{+0.13}_{-0.13}$
	norm (10^{-3} photons cm^{-2}s^{-1})	$1.33^{+0.12}_{-0.12}$	$0.68^{+0.10}_{-0.08}$	$0.82^{+0.11}_{-0.10}$
	χ^2 / d.o.f.	187.23 / 169	130.24 / 124	113.10 / 130
Absorption	N_H (10^{21} cm^{-2})	$2.07^{+0.27}_{-0.27}$	$1.55^{+0.39}_{-0.39}$	$1.85^{+0.39}_{-0.38}$
SRCUT	Spectral Index (α)	0.57 (fixed)	0.57 (fixed)	0.57 (fixed)
	$\nu_{\text{roll-off}}$ (10^{16} Hz)	$5.96^{+0.12}_{-0.12}$	$8.00^{+0.25}_{-0.25}$	$7.06^{+0.20}_{-0.20}$
	Flux (10^{-13} ergs cm^{-2}s^{-1}) ‡	$14.91^{+0.33}_{-0.38}$	$8.69^{+0.28}_{-0.38}$	$9.66^{+0.29}_{-0.28}$
	χ^2 / d.o.f.	115.24 / 131	130.21 / 125	115.24 / 131

‡ Flux in 1 − 5 band.

Table 5.28 Best-fit parameters for BGD-2 subtracted spectrum of selected emission region on the W rim of SN 1006 (1 − 5 keV).

Components	Parameters		Values	
		Source#1	Source#2	Source#3
Absorption	N_H (10^{21} cm^{-2})	$3.26^{+0.72}_{-0.71}$	$2.61^{+1.04}_{-1.02}$	$3.28^{+1.07}_{-1.04}$
POWER-LAW	Photon Index	$2.78^{+0.08}_{-0.08}$	$2.67^{+0.12}_{-0.12}$	$2.77^{+0.12}_{-0.12}$
	norm (10^{-3} photons cm^{-2}s^{-1})	$1.25^{+0.12}_{-0.12}$	$0.65^{+0.08}_{-0.07}$	$0.79^{+0.10}_{-0.09}$
	χ^2 / d.o.f.	183.40 / 169	128.51 / 124	114.43 / 130
Absorption	N_H (10^{21} cm^{-2})	$1.85^{+0.27}_{-0.2}$	$1.31^{+0.39}_{-0.38}$	$1.77^{+0.38}_{-0.38}$
SRCUT	Spectral Index (α)	0.57 (fixed)	0.57 (fixed)	0.57 (fixed)
	$\nu_{\text{roll-off}}$ (10^{16} Hz)	$7.66^{+0.16}_{-0.16}$	$10.05^{+0.33}_{-0.33}$	$8.00^{+0.23}_{-0.23}$
	Flux (10^{-13} ergs cm^{-2}s^{-1}) ‡	$15.45^{+0.35}_{-0.38}$	$8.94^{+0.29}_{-0.34}$	$9.85^{+0.30}_{-0.29}$
	χ^2 / d.o.f.	180.68 / 170	129.00 / 125	117.19 / 131

‡ Flux in 1 − 5 band.

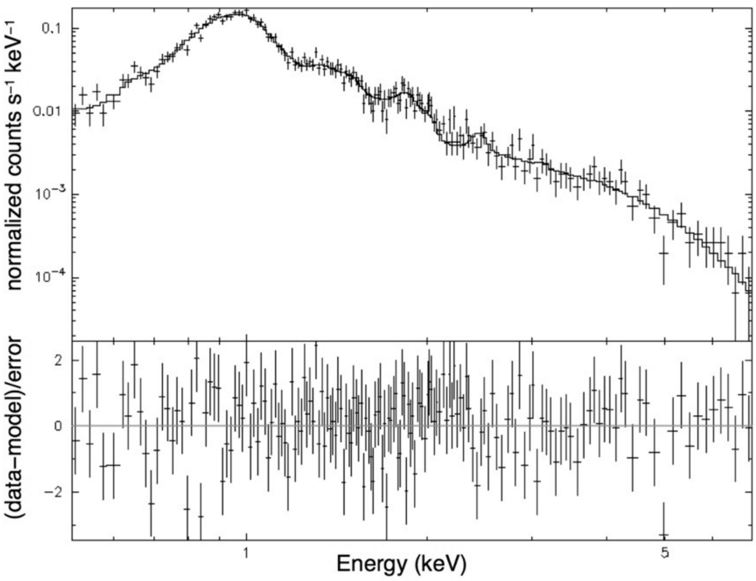

Figure 5.20 Modelled background spectrum of the selected region of the NW rim of SN 1006.

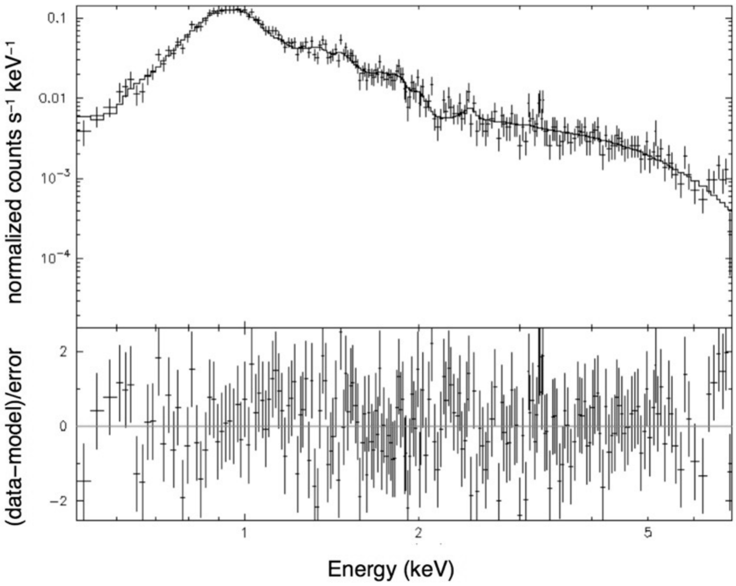

Figure 5.21 Modelled background spectrum of the selected region of the S rim of SN 1006.

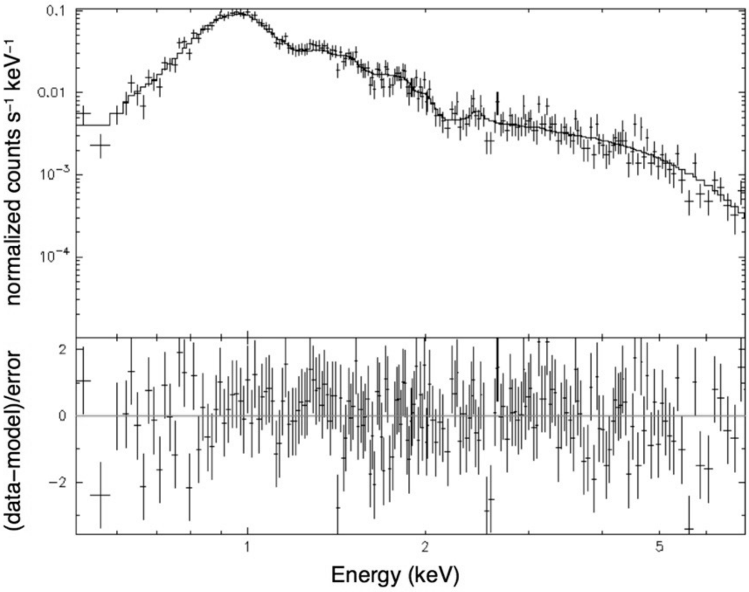

Figure 5.22 Modelled background spectrum of the selected region of the SE rim of SN 1006.

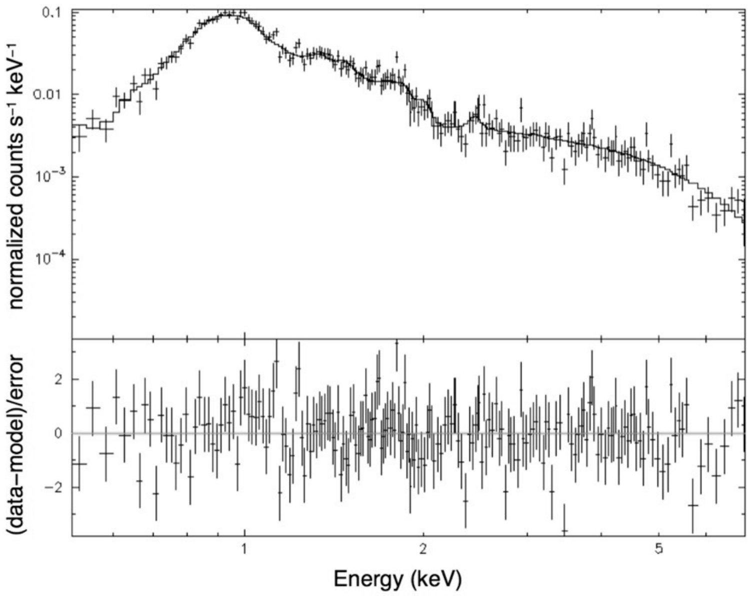

Figure 5.23 Modelled background spectrum of the selected region of the SW rim of SN 1006.

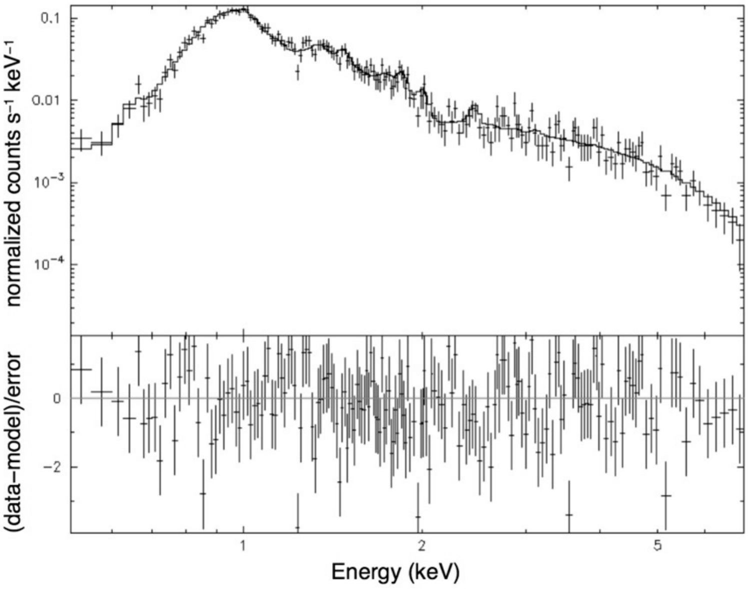

Figure 5.24 Modelled background spectrum of the selected region of the W rim of SN 1006.

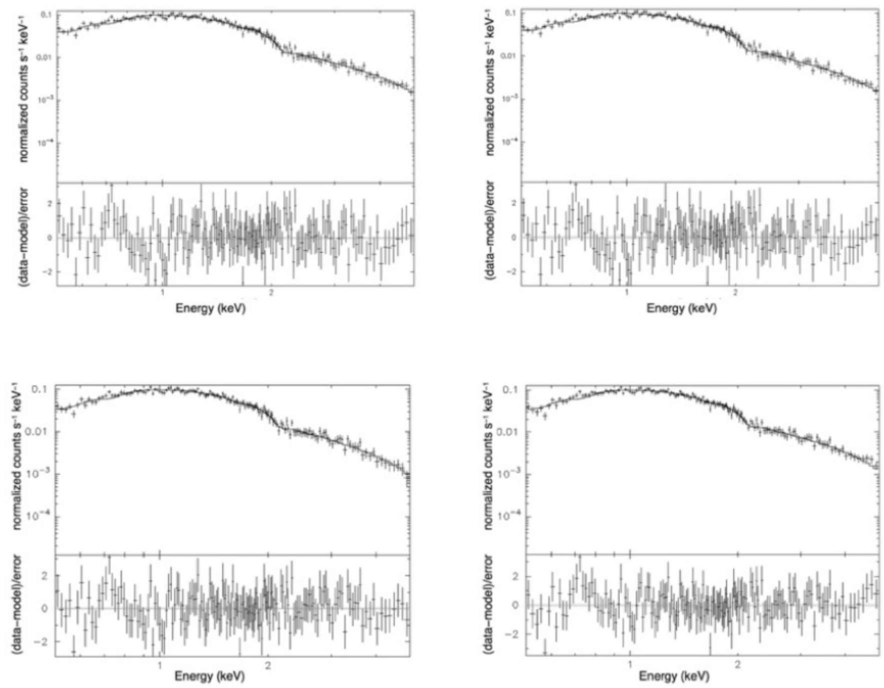

Left panels show the BGD-1 subtracted spectra. Right panels show the BGD-2 subtracted spectra, each modelled with *PL* and *SRCUT*.

Figure 5.25 BGD-1 (left) and BGD-2 (right) subtracted spectra of the region#1 on the NW rim.

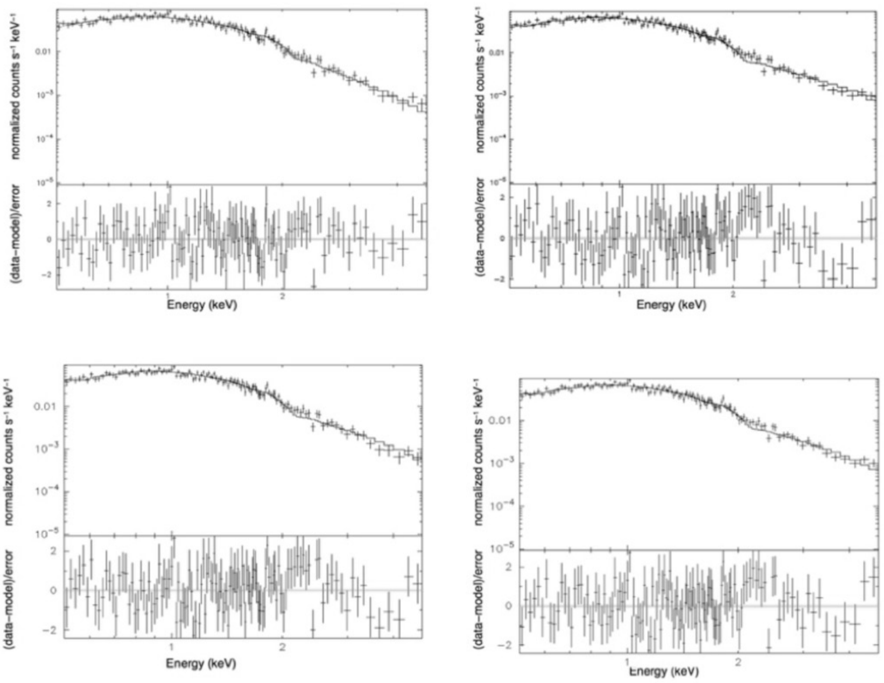

Left panels show the BGD-1 subtracted spectra. Right panels show the BGD-2 subtracted spectra, each modelled with *PL* and *SRCUT*.

Figure 5.26 BGD-1 (left) and BGD-2 (right) subtracted spectra of the region#2 on the NW rim.

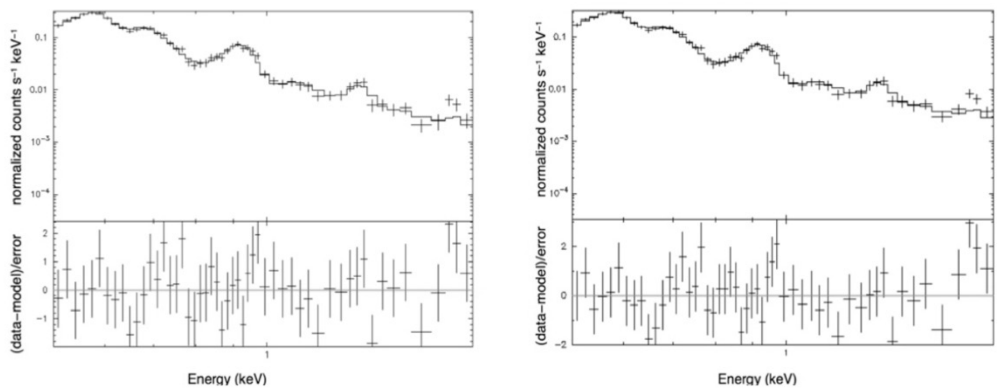

Left panels show the BGD-1 subtracted spectra. Right panels show the BGD-2 subtracted spectra, each modelled with *VNEI*.

Figure 5.27 BGD-1 (left) and BGD-2 (right) subtracted spectra of the region#3 on the NW rim.

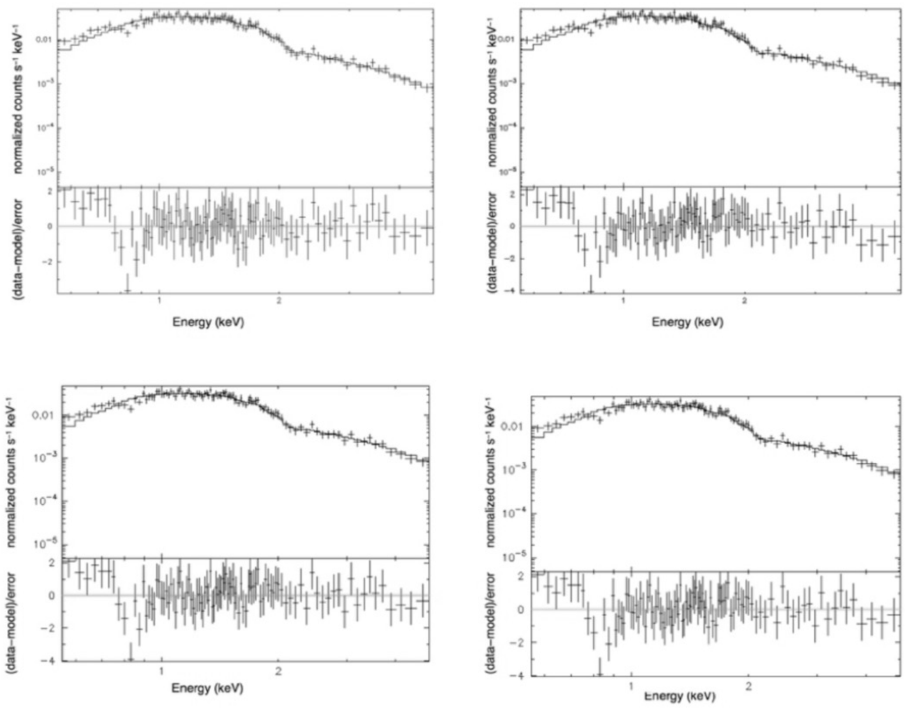

Left panels show the BGD-1 subtracted spectra. Right panels show the BGD-2 subtracted spectra, each modelled with *PL* and *SRCUT*.

Figure 5.28 BGD-1 (left) and BGD-2 (right) subtracted spectra of the region#1 on the S rim.

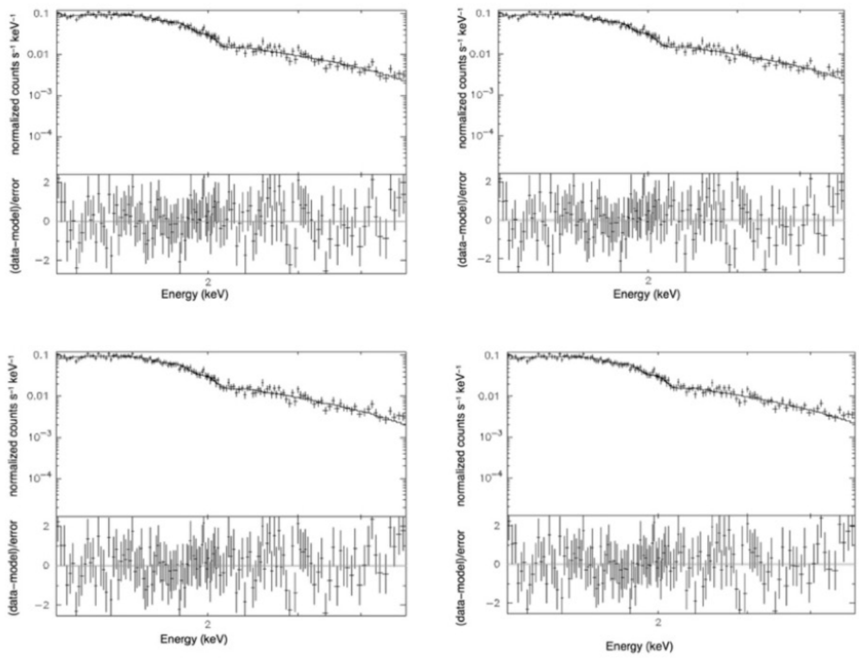

Left panels show the BGD-1 subtracted spectra. Right panels show the BGD-2 subtracted spectra, each modelled with *PL* and *SRCUT*.

Figure 5.29 BGD-1 (left) and BGD-2 (right) subtracted spectra of the region#2 on the S rim.

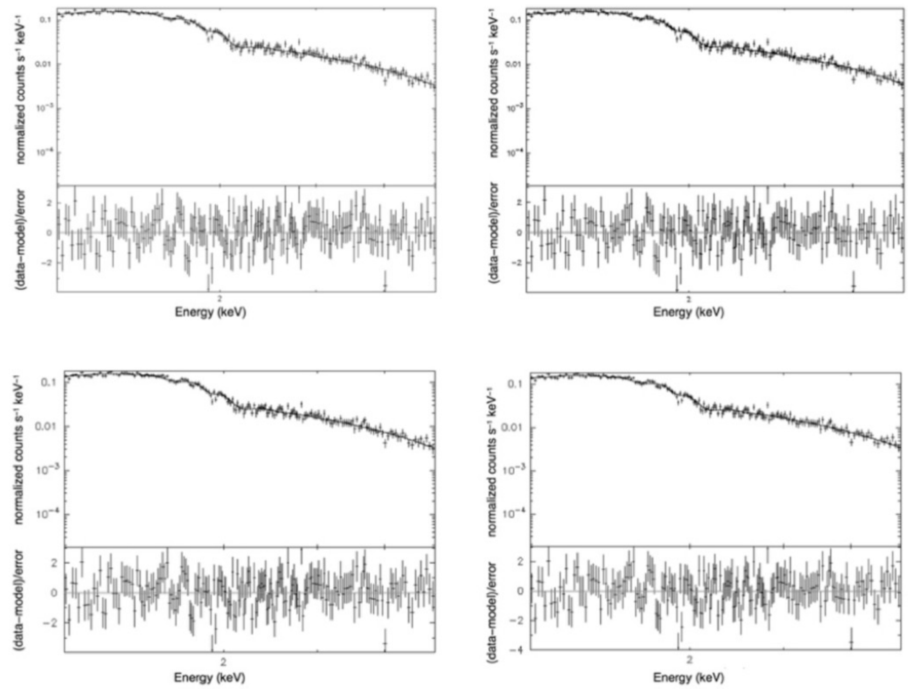

Left panels show the BGD-1 subtracted spectra. Right panels show the BGD-2 subtracted spectra, each modelled with *PL* and *SRCUT*.

Figure 5.30 BGD-1 (left) and BGD-2 (right) subtracted spectra of the region#1 on the SE rim.

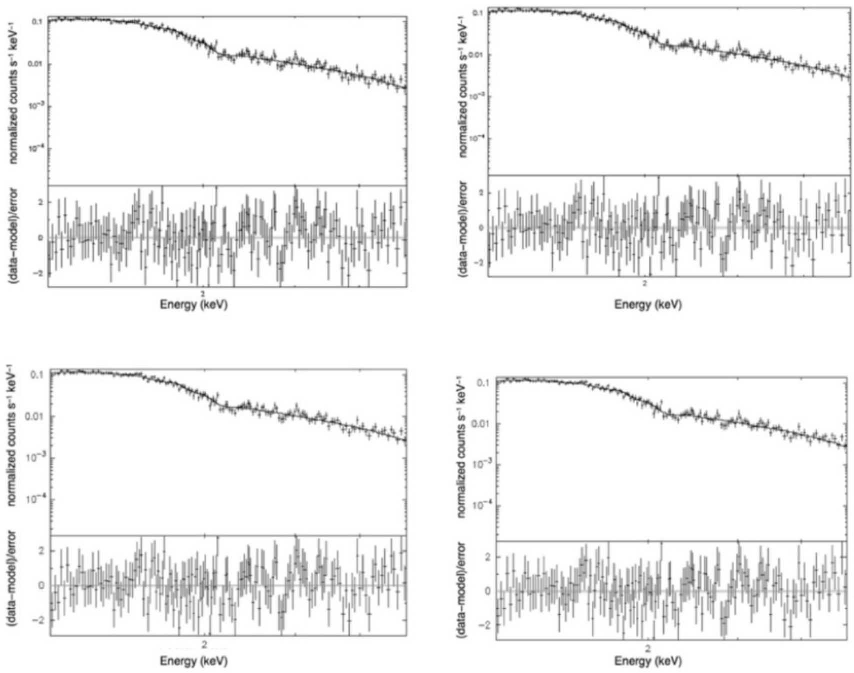

Left panels show the BGD-1 subtracted spectra. Right panels show the BGD-2 subtracted spectra, each modelled with *PL* and *SRCUT*.

Figure 5.31 BGD-1 (left) and BGD-2 (right) subtracted spectra of the region#1 on the SW rim.

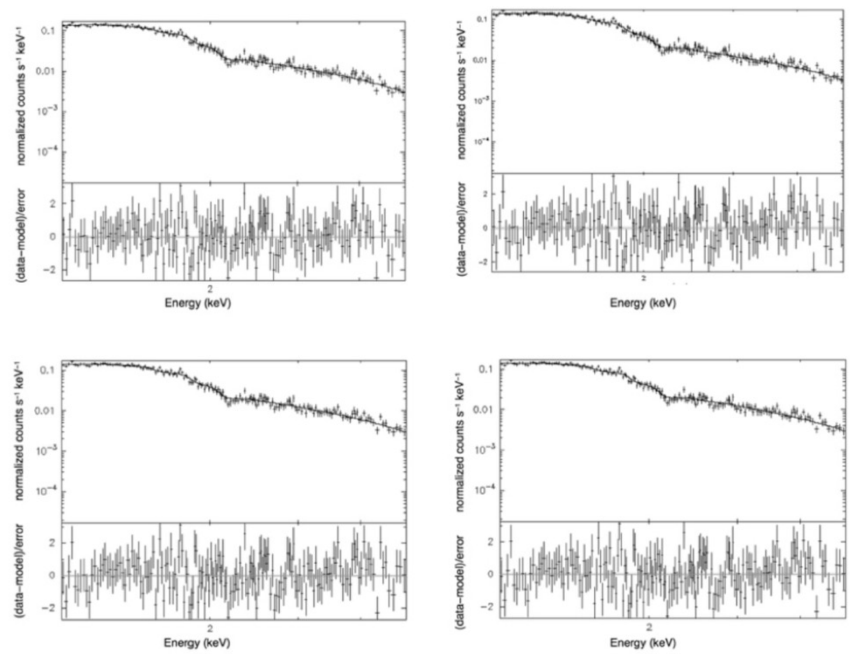

Left panels show the BGD-1 subtracted spectra. Right panels show the BGD-2 subtracted spectra, each modelled with *PL* and *SRCUT*.

Figure 5.32 BGD-1 (left) and BGD-2 (right) subtracted spectra of the region#2 on the SW rim.

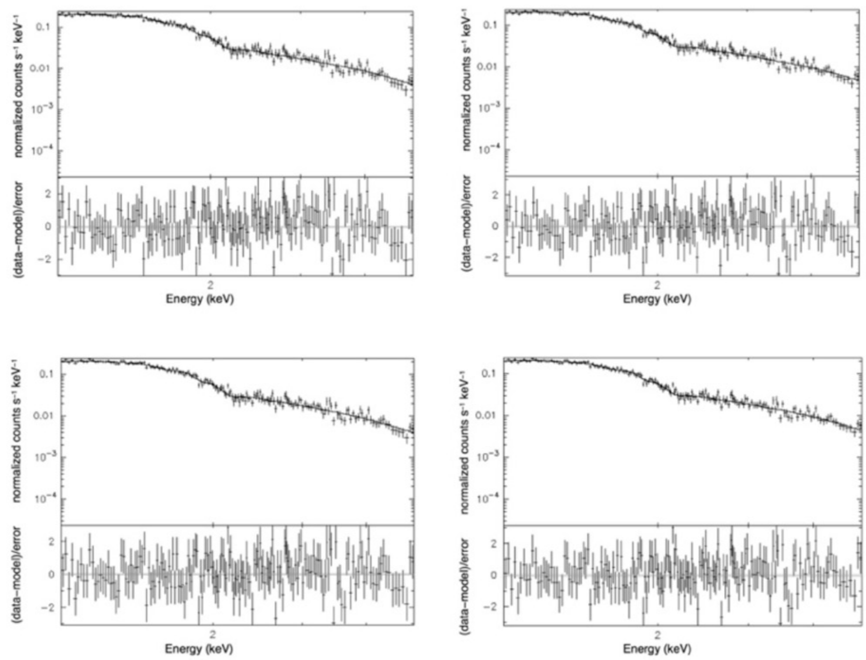

Left panels show the BGD-1 subtracted spectra. Right panels show the BGD-2 subtracted spectra, each modelled with *PL* and *SRCUT*.

Figure 5.33 BGD-1 (left) and BGD-2 (right) subtracted spectra of the region#1 on the W rim.

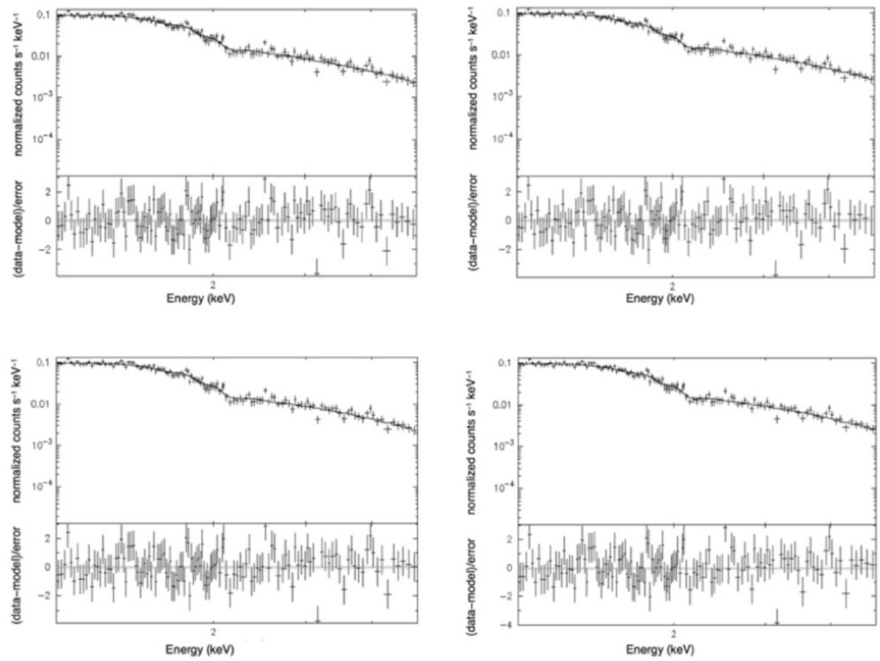

Left panels show the BGD-1 subtracted spectra. Right panels show the BGD-2 subtracted spectra, each modelled with *PL* and *SRCUT*.

Figure 5.34 BGD-1 (left) and BGD-2 (right) subtracted spectra of the region#2 on the W rim.

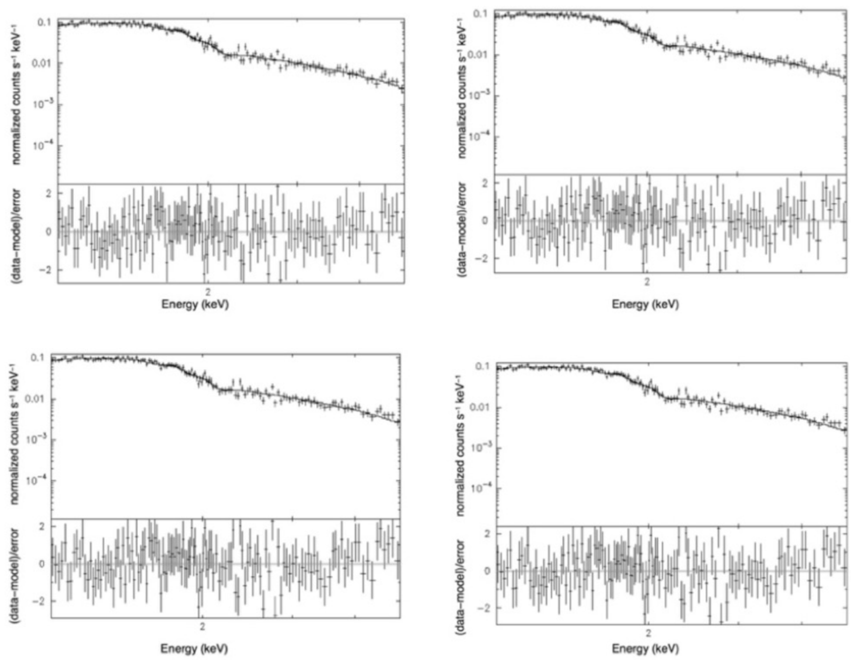

Left panels show the BGD-1 subtracted spectra. Right panels show the BGD-2 subtracted spectra, each modelled with *PL* and *SRCUT*.

Figure 5.35 BGD-1 (left) and BGD-2 (right) subtracted spectra of the region#3 on the W rim.

5.2.5 Vela Jr.

5.2.4.1 Literature

Bamba et al. (2005) [129] studied the filamentary structure on the NW edge of the SNR in the hard X-ray band, and showed NT emission from the remnant. They found no line-like structure, and the spectra of filaments are hard. The spectra are well reproduced with an absorbed PL model with a photon index value of about 2.67, or the spectra are well fitted with *SRCUT* model with the roll-off frequency of about 4.3×10^{16} Hz under the assumption of p = 0.3. Utilizing *Chandra* data, they estimated the age and the distance of Vela Jr. as ~660 yr, and ~0.33 kpc, respectively. They implied that these age and distance results may suggest that there is no significant interaction between Vela SNR and Vela Jr.

Telezhinsky (2009) [130] considered Vela Jr. as being the old SNR at the beginning of the transition from adiabatic to radiative stage of evolution. Vela Jr. is situated outside Vela SNR at the distance of ~600 pc and its age is 17,500 yr, according to the used hydro dynamical model of the transition stage to the SNR, where the high energy fluxes from Vela Jr. and its broadband spectrum are modelled. On the other hand, this model explains the observed TeV γ-ray flux by hadronic mechanism. Telezhinsky (2009) [130] found that the explosion energy was 0.2×10^{51} ergs.

Iyudin et al. (2010) [131] detected both high and low velocity interstellar CaII absorptions from Vela Jr. They indicated that if their estimates are correct, SN Ib or SN Ic could have produced this SNR due to the implying that the angular size of the SNR, the absence of broad C II absorption lines, the constraints imposed by the flux of the ^{44}Ti γ-ray line.

Using *XMM-Newton*, Acero et al. (2011) [132] searched for the X-ray counterpart of the pulsar PSR J0855−4644 discovered near the SE rim of Vela Jr. by the Parkes Multibeam Survey. They found no bright thin X-ray filaments in the NW rim of the SNR. They derived an upper limit to the distance of the SNR and the pulsar <900 pc. They found an extended NT emission, and the nebula of the pulsar has a maximum extent of ~150″.

Allen et al. (2015) [133] analysed *Chandra* archival ACIS data of the Vela Jr. to understand its expansion. According to the results, the relatively bright and narrow portion of the NW rim experienced a radial displacement of about 2.40 arcsec over a period of 5652 yr. They implying that the expansion rate is 13.6 ± 4.2% kyr^{-1}. They used the models of [134] to perform a hydrodynamic analysis to constrain the age. They considered plenty of scenarios to try to encircle all possible sets of hydrodynamic characteristics, using ranges of initial kinetic energies, ejecta masses, ejecta mass density distributions, ambient densities, and evolutionary states. The age of Vela jr. is most likely in the range of 2.4 − 5.1 kyr due to these scenarios, no matter what was the SN event. They suggest that the remnant could not be younger than 2.2 kyr. The other suggestion they made is that Vela Jr. is fairly too old to be related with emission from the decay of ^{44}Ti. Based on the *Chandra* expansion rate, they set a minimum limit on the distance of about 0.5 kpc.

Vela Jr. emits synchrotron X-rays, and also TeV γ-rays. Using thirty-nine *Suzaku* mapping observation data, Takeda et al. (2016) [135] detected hard X-ray emission from the NW rim of the SNR, which is a TeV emitting region. They found "X-rays with the energy up to 22 keV from the north region of the SNR, and showed that the soft and hard X-ray spectrum is well reproduced by a single PL model with the photon indices of 2.93 ± 0.02 and 3.15 ± 1.16 in the 12 – 22 keV band, respectively". They derived "the flux of (4.43 ± 0.03) × 10^{-11} erg cm^{-2} s^{-1} in 2 – 10 keV band, and Aharonian et al. (2007) [136] derived the TeV flux of entire Vela Jr. of (15.2 ± 0.7 ± 3.20) ± 10^{-12} cm^{-2} s^{-1} with H.E.S.S." According to these studies, both band spectra exhibit similar slope and the X-ray to TeV γ-ray flux ratio is ~ 2.91. Takeda et al. (2016) [135] estimated "the magnetic field B ~ 5.5 μG, assuming the cosmic microwave background IC scattering as TeV emission".

5.2.4.2 Background Estimation

For the both N and NW rims of Vela Jr., the spectra of the selected sources were fitted with subtracting the BGD-1. Next, the background spectra of the sources on the N and NW observations were modelled with subtracting the BGD-2.

Vela Jr. is on the Galactic plane (l = 266$^{\circ}_{.}$259, b = −01$^{\circ}_{.}$220). Thus, the possible contamination of the GRXE was evaluated [87]. However, it was neglected with assuming its affectless feature on the spectra. Hence, the background spectrum of N rim was fitted with the assumption that the emission contains CXB, and FE. The background spectrum was fitted with a model of [Abs$_{(CXB)}$ × PL$_{(CXB)}$ + apec$_{(FE)}$], where the *APEC* represents the FE component, while an absorbed PL model represents the CXB emission defined under the assumption with PL shape with a photon index of about 1.41, and a surface brightness value of 5.41×10^{-15} erg s^{-1} cm^{-2} $arcmin^{-2}$ in the 2 − 10 keV band [22]. Next, the background spectrum was simulated.

As in the background modelling for the northern rim observation, for the background analysis of NW rim the GRXE component is negligible. Hence, fitting the background spectrum with a single CXB component is sufficient for the spectral analysis for this region. The same parameters were used for the CXB component as mentioned before; only the column density was set free. Same as the previous background modelling, the background spectrum was simulated using *FAKEIT* command, and subtracted from the source spectrum. The best-fit parameters and spectra of the background regions are shown in Table 5.29 and Table 5.30 Figure 5.37 and Figure 5.38, respectively.

5.2.4.3 Spectral Fitting

The absorption column density was fixed to be 6.7×10^{21} cm^{-2} [26] using *TBABS* in XSPEC with the metal abundance adopted from [60]. The energy range of below 2 keV was restricted to avoid thermal contamination from Vela SNR for the all fits, because of the ambiguity caused by this remnant [137].

The spectral analysis region was fitted on the N rim with an absorbed *PL* model. Then, the same region was fitted with BGD-2 subtracted spectrum with an absorbed single *PL* and an absorbed *broken PL* model, respectively. The absorbed *broken PL* model gave an acceptable reduced chi-square value, compared with the absorbed *PL* model.

The three spectral analysis regions on the NW rim were fitted with an absorbed *single PL* model and an absorbed *SRCUT* model [108], [138]. While applying the *PL* model, as in the spectral analysis of the northern region, the column density N_H was fixed to be 6.7×10^{21} cm^{-2}, and the other parameters were set free. While fitting *SRCUT* model, a synchrotron emission for the hard X-ray emission observed from the SNR were assumed and spectral index (α) and flux density values were employed as ~0.52 and 0.074 Jy at 1 GHz [29], respectively, and the Galactic hydrogen column density parameters were set free for the sources region#1 and region#2.

After spectral analysis of the region#1 and region#2, they were excluded from the emission region#3 (Figure 5.36), to characterize the whole NT emission of NW edge, taking into account of the nearby emission of these X-ray peaks.

In all fits, the column density (N_H) was always fixed to 6.7×10^{21} cm^{-2} as mentioned before, the photon indexes (Γ), breaking energy and the normalizations are set as free parameters. All spectra were fitted in the 2.0 − 7.0 keV effective energy band. The best-fit parameters are shown in Table 5.31, 5.32, 5.33 and 5.34, the background subtracted spectra are shown in Figure 5.39, 5.40, 5.41 and 5.42 for BGD-1 and BGD-2 spectra, respectively.

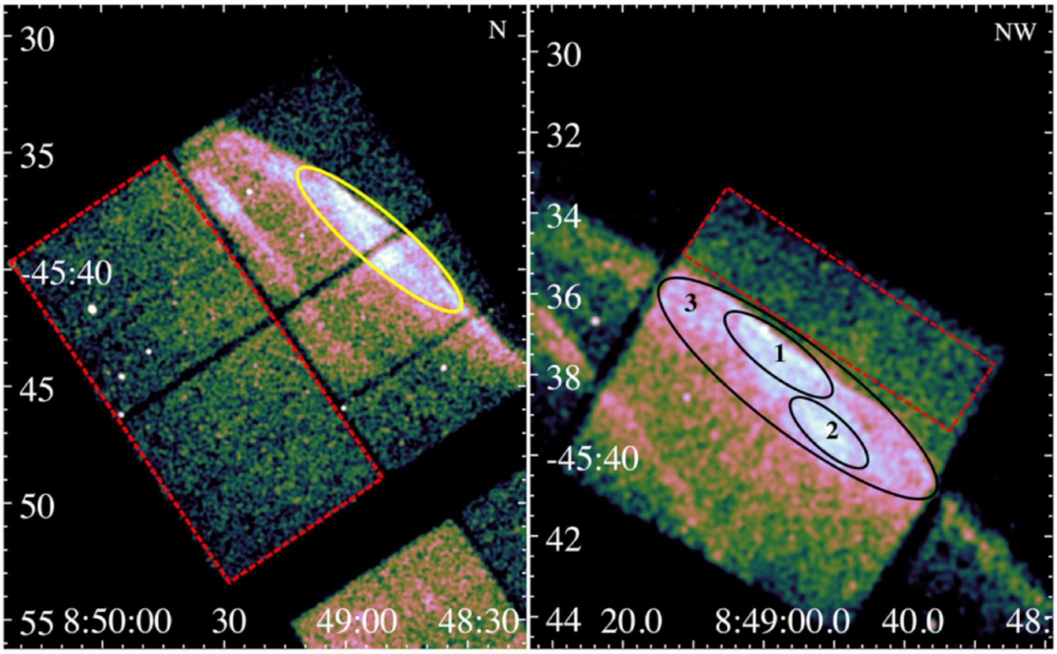

The source regions are given in numbered yellow and black areas and the background regions are chosen with the red dashed rectangular regions.

Figure 5.36 X-ray image of the SNR Vela Jr. with the source and background regions for all the rims.

5.2.4.4 Spectral Analysis Results of Vela Jr.

Vela Jr. is an X-ray synchrotron emitting SNR [110], [135]. Due to obtain roll-off frequency to calculate maximum energy of electrons ($E_{max,e}$) with using the analysis methods described in previous section, background analysis was also aimed for a comparative approach to get sensitive values about synchrotron spectrum parameters. In accordance with these purposes, the background regions were modelled and their best-fit parameters are given in Table 5.29 and Table 5.30, the spectra are in Figure 5.37 − 5.38. Also, the spectra of the selected source regions are shown in Table 5.31, 5.32, 5.33 and 5.34, the background subtracted spectra are shown in Figure 5.39, 5.40, 5.41 and 5.42 for BGD-1 and BGD-2 spectra, respectively. All errors indicate 90% confidence intervals.

Table 5.29 Best-fit parameters for the background spectrum of the N rim of Vela Jr.

Components	Parameters	Values
CXB	N_H (10^{22} cm^{-2})*	0.670 (fixed)
	Photon Index †	1.412 (fixed)
	S.B. (erg s^{-1} cm^{-2} $arcmin^{-2}$) †	5.410×10^{-15} (fixed)
FE	kT (keV)	$0.671^{+0.046}_{-0.091}$
	norm (10^{-3} photons cm^{-2} s^{-1})	$0.744^{+0.004}_{-0.001}$
	χ^2 / d.o.f.	290.64 / 340

*: [137] †: [50] (S. B.: Surface Brightness in the 2 – 10 keV band).

Table 5.30 Best-fit parameters for the background spectrum of the NW rim of Vela Jr.

Components	Parameters	Values
CXB	N_H (10^{22} cm^{-2}) †	$2.510^{+0.781}_{-0.678}$
	Photon Index	1.412 (fixed)
	S.B. (erg s^{-1} cm^{-2} $arcmin^{-2}$) †	5.410×10^{-15} (fixed)
	χ^2 / d.o.f.	262.44 / 341

†: [50] (S. B.: Surface Brightness in the 2 – 10 keV band).

Table 5.31 Best-fit parameters for BGD-1 subtracted spectrum of selected emission region on the N rim of Vela Jr.

Components	Parameters	Values
Absorption	N_H (10^{22} cm^{-2})	$0.75^{+0.08}_{-0.08}$
POWER-LAW	Photon Index	$2.54^{+0.08}_{-0.08}$
	norm (10^{-3} photons cm^{-2} s^{-1})	$0.30^{+0.03}_{-0.02}$
	χ^2 / d.o.f.	244.06/224
Absorption	N_H (10^{22} cm^{-2})	$0.61^{+0.03}_{-0.03}$
SRCUT	Spectral Index (α)	0.52 (fixed)
	$\nu_{roll\text{-}off}$ (10^{17} Hz)	$1.33^{+0.03}_{-0.03}$
	Flux (10^{-12} ergs cm^{-2} s^{-1}) ‡	$3.77^{+0.08}_{-0.10}$
	χ^2 / d.o.f.	243.89 / 225

‡ Flux in 1 − 5 keV band.

Table 5.32 Best-fit parameters for BGD-2 subtracted spectrum of selected emission region on the N rim of Vela Jr.

Components	**Parameters**	**Values**
Absorption	N_H (10^{22} cm^{-2})	$0.80^{+0.07}_{-0.07}$
POWER-LAW	Photon Index	$2.40^{+0.07}_{-0.07}$
	norm (10^{-3} photons cm^{-2} s^{-1})	$0.31^{+0.03}_{-0.02}$
	χ^2 / d.o.f.	264.78/224
Absorption	N_H (10^{22} cm^{-2})	$0.68^{+0.03}_{-0.03}$
SRCUT	Spectral Index (α) *	0.52 (fixed)
	$\nu_{\text{roll-off}}$ (10^{17} Hz)	$2.07^{+0.05}_{-0.05}$
	Flux (10^{-12} ergs cm^{-2} s^{-1}) ‡	$4.20^{+0.10}_{-0.09}$
	χ^2 / d.o.f.	267.70 / 225

‡: Flux in 1 − 5 keV band. *: [139].

Table 5.33 Best-fit parameters for BGD-1 subtracted spectrum of selected emission region on the NW rim of Vela Jr.

Components	**Parameters**		**Values**	
		Source No. 1	Source No. 2	Source No. 3
Absorption	N_H (10^{22} cm^{-2})†	0.67 (fixed)	0.67 (fixed)	0.67 (fixed)
POWER-LAW	Photon Index	$2.52^{+0.12}_{-0.13}$	$2.64^{+0.17}_{-0.16}$	$2.52^{+0.08}_{-0.08}$
	norm (10^{-3} photons cm^{-2}s^{-1})	$0.79^{+0.11}_{-0.10}$	$0.67^{+0.09}_{-0.10}$	$2.05^{+0.18}_{-0.07}$
	χ^2 / d.o.f.	115.25 / 108	85.06 / 84	170.63 / 182
SRCUT	N_H (10^{22} cm^{-2})	$0.98^{+0.35}_{-0.35}$	$0.92^{+0.42}_{-0.42}$	0.67 (fixed) ‡
	Spectral Index (α) ‡	0.52 (fixed)	0.52 (fixed)	0.52 (fixed)
	ν_{rolloff} (10^{17} Hz)	$1.01^{+0.05}_{-0.05}$	$0.78^{+0.04}_{-0.04}$	$2.70^{+0.07}_{-0.07}$
	norm (Jy at 1 GHz) ‡	0.074 (fixed)	0.074 (fixed)	0.074 (fixed)
	χ^2 / d.o.f.	115.95 / 108	85.98 / 84	196.59 / 193

†: [137]. ‡: [139].

Table 5.34 Best-fit parameters for BGD-2 subtracted spectrum of selected emission region on the NW rim of Vela Jr.

Components	**Parameters**		**Values**	
		Source No. 1	Source No. 2	Source No. 3
Absorption	N_H (10^{22} cm^{-2}) †	0.67 (fixed)	0.67 (fixed)	0.67 (fixed)
POWER-LAW	Photon Index	$2.42^{+0.11}_{-0.11}$	$2.53^{+0.13}_{-0.13}$	$2.37^{+0.08}_{-0.08}$
	norm (10^{-3} photons $cm^{-2}s^{-1}$)	$0.77^{+0.11}_{-0.10}$	$0.64^{+0.10}_{-0.09}$	$2.02^{+0.07}_{-0.06}$
	χ^2 / d.o.f.	115.25 / 108	85.06 / 84	170.63 / 182
Absorption	N_H (10^{22} cm^{-2})	$1.14^{+0.33}_{-0.32}$	$1.12^{+0.39}_{-0.39}$	0.67 (fixed) ‡
SRCUT	Spectral Index (α)‡	0.52 (fixed)	0.52 (fixed)	0.52 (fixed)
	$\nu_{rolloff}$ (10^{17} Hz)	$1.11^{+0.05}_{-0.04}$	$0.85^{+0.04}_{-0.04}$	$3.33^{+0.08}_{-0.08}$
	norm (Jy at 1 GHz) ‡	0.074 (fixed)	0.074 (fixed)	0.074 (fixed)
	χ^2 / d.o.f.	119.98 / 108	88.63 / 84	179.51 / 183

†: [137]. ‡: [139].

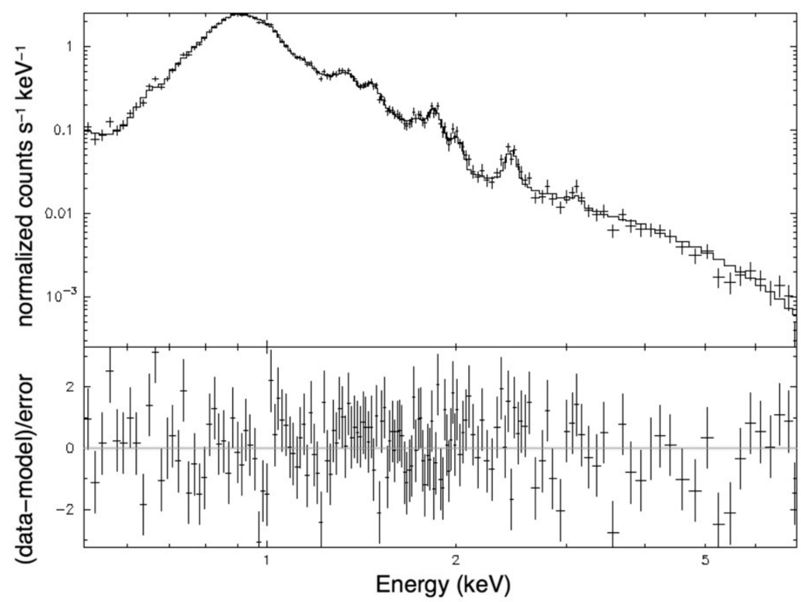

Figure 5.37 Modelled background spectrum of the selected region of the N rim of Vela Jr.

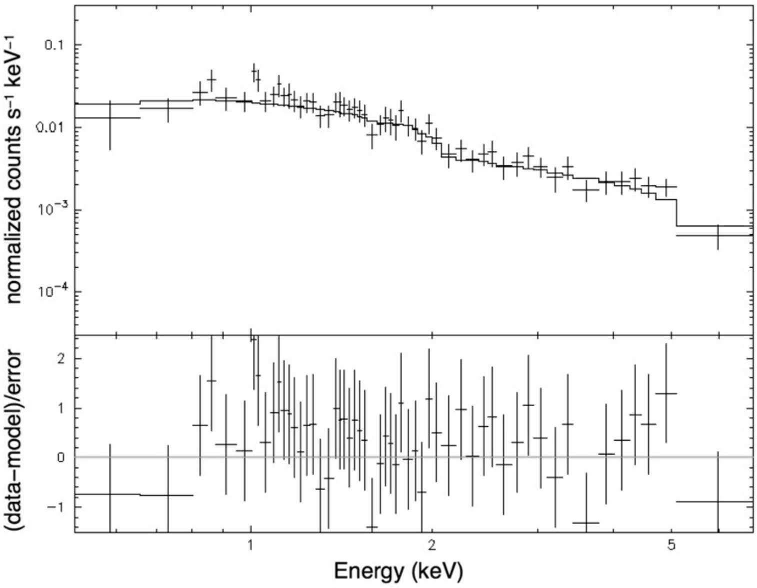

Figure 5.38 Modelled background spectrum of the selected region of the NW rim of Vela Jr.

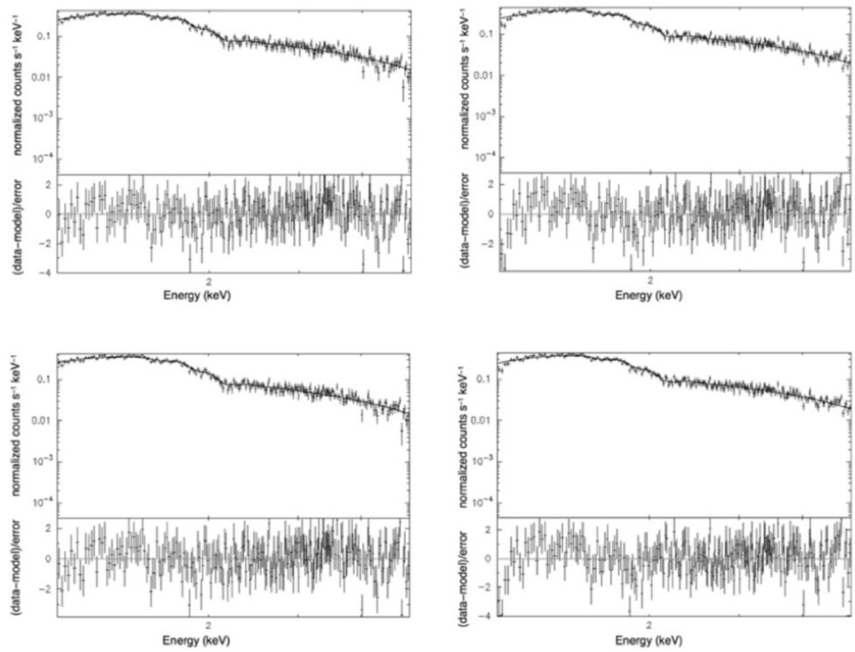

Left panels show the BGD-1 subtracted spectra. Right panels show the BGD-2 subtracted spectra, each modelled with *PL* and *SRCUT*.

Figure 5.39 BGD-1 (left) and BGD-2 (right) subtracted spectra of the region#1 on the N rim.

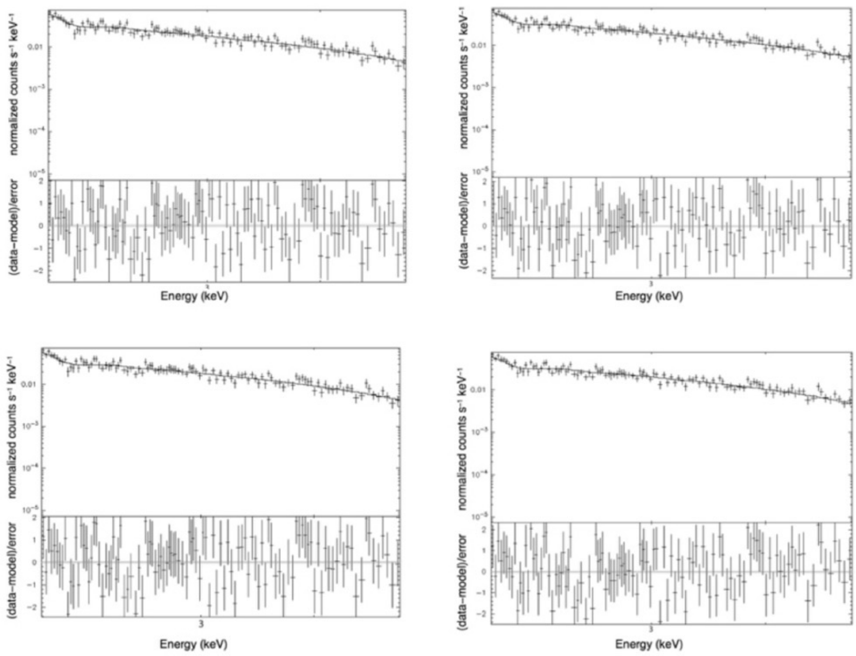

Left panels show the BGD-1 subtracted spectra. Right panels show the BGD-2 subtracted spectra, each modelled with *PL* and *SRCUT*.

Figure 5.40 BGD-1 (left) and BGD-2 (right) subtracted spectra of the region#1 on the NW rim.

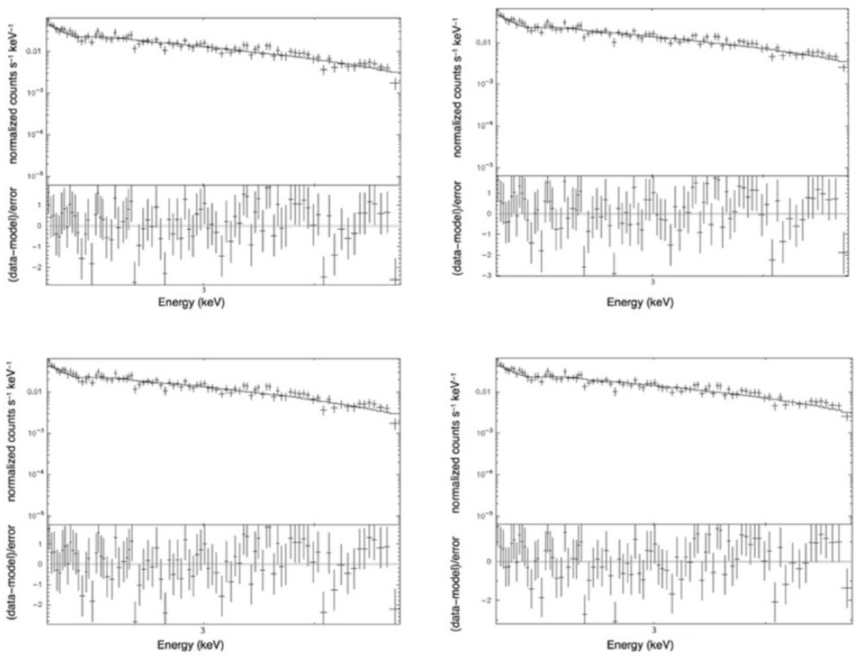

Left panels show the BGD-1 subtracted spectra. Right panels show the BGD-2 subtracted spectra, each modelled with *PL* and *SRCUT*.

Figure 5.41 BGD-1 (left) and BGD-2 (right) subtracted spectra of the region#2 on the NW rim.

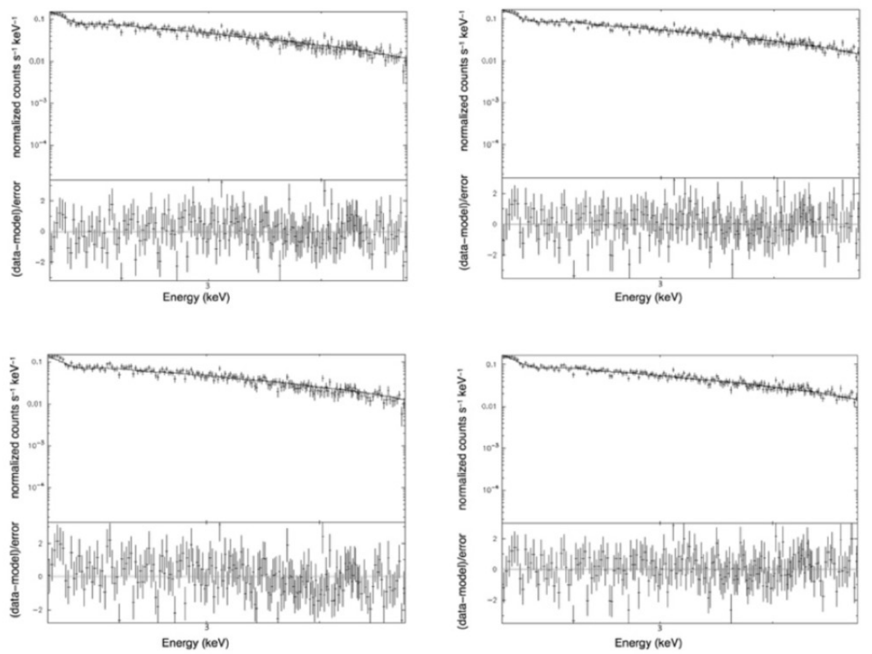

Left panels show the BGD-1 subtracted spectra. Right panels show the BGD-2 subtracted spectra, each modelled with *PL* and *SRCUT*.

Figure 5.42 BGD-1 (left) and BGD-2 (right) subtracted spectra of the region#3 on the NW rim.

5.3 Calculations of the Maximum Energy of Electrons

Observations of synchrotron emission in X-ray band can be advantageous to inspect young SNRs as electron accelerator in the range of 10 – 100 TeV [140]. From radio to X-ray energy bands in the electromagnetic spectrum, spectral fitting of the synchrotron emission is enlightening about the acceleration mechanism and its characteristic that correlated with roll-off frequency (ν_{roll}) of the spectrum, which is required for the estimating the maximum energy of the electrons ($E_{max,e}$), and thus with the given values of downstream magnetic field (B_d), and the SNR age (t_{age}), maximum energy of protons ($E_{max,p}$) can be calculated ($E_{max,e}^2\, B^2\, t_{age}$).

The key point to determine the $E_{max,e}$ is whether the SNR age is shorter than the synchrotron loss time scale or not.

Thus, with the *SRCUT* model in XSPEC was used to calculate the roll-off frequency to calculate $E_{max,e}$. On the other hand, $E_{max,p}$ in the system could be determined by the equation 5.3. The maximum energy of electrons can be calculated in two methods (where $t_{loss,e}$ is synchrotron time scale):

For the age-limited case (when $t_{age} < t_{loss,e}$), the acceleration time scale (ATS) is equal to the acceleration site – the age of the remnant is equal to the ATS ($t_{age} = t_{acc}$).

In this case, the maximum energy is given as

$$E_{max,e} = \frac{4.8 \times 10^2}{\xi} \left(\frac{\upsilon_s}{10^8 cms^{-1}}\right)^2 \left(\frac{B_d}{10\ \mu G}\right)^{-1/2} \left(\frac{t_{age}}{10^5\ yr}\right) \text{TeV} \tag{5.1}$$

Loss-limited case (when $t_{age} > t_{loss,e}$), the maximum energy is given as

$$E_{max,e} = \frac{24}{\xi^{1/2}} \left(\frac{\upsilon_s}{10^8 cms^{-1}}\right) \left(\frac{B_d}{10\ \mu G}\right)^{-1/2} \text{TeV} \tag{5.2}$$

where ξ ($\gtrsim$1), B_d, and υ_s are gyro-factor (the ratio of the particle mean free path to the gyro-radius or represents the largeness of the magnetic field turbulence), the downstream magnetic field, and the shock velocity, respectively. The case of $\xi = 1$ (the case of most efficient acceleration) correlates to the “Bohm limit”, and intends high level of turbulence ($\delta B \sim B$). According to our high magnetic field values from literature, we used loss-limited case in our calculations. Because electrons with higher energies or in higher magnetic fields lose energy faster [39]. Besides, maximum energy of protons can be calculated as [141]

$$E_{max,p} \approx 2.6 \times 10^{15}\ \text{eV} \left(\frac{\upsilon_{roll}}{5 \times 10^{18} Hz}\right) \left(\frac{B_d}{mG}\right) \left(\frac{t_{age}}{10^2 yr}\right) \tag{5.3}$$

Also, the shock velocity can be derived using the roll-off frequency as below [141],

$$\nu_{roll\text{-}off} \approx 9.2 \times 10^{16}\ \text{Hz} \left(\frac{\upsilon_s}{10^8 cms^{-1}}\right)^2 \tag{5.4}$$

Also [138],

$$\nu_{roll\text{-}off} = 5 \times 10^{17}\ \text{Hz} \left(\frac{B_d}{10\ \mu G}\right) \left(\frac{E_{max,e}}{100\ TeV}\right)^2 \tag{5.5}$$

According to the formulae above, calculated results using the roll-off frequency obtained by spectral analysis and magnetic field, and age values gathered from literature, are shown in Table 5.35. “Strength of magnetic fields are critical values in determining the maximum energy of the particles accelerated, despite they are not dynamically important in SNRs” (e.g., [142]). During maximum energy calculations of accelerated particles, magnetic field values were chosen according to the method used in literature which is pointing the thickness of synchrotron X-rays. This method extracts “average magnetic field strength” in the downstream region. Related magnetic field values can be seen in Table 5.35. Additionally, the age of an SNR can be derived with using the values of the velocity of the ejecta and the radius which are related to the initial explosion energy, the mass of the ejecta and the ambient density (Section 2.3.2). If these values are somehow not known, and the thermal emission is the point, the age of the SNR can be found using the relation between the ionisation timescale and the electron density ($\tau = n_e\, t_{age}$). The values gathered from previously studies are also shown in Table 5.35 – 5.44.

If a “strong magnetic field” (B ~ 0.1 – 1 mG [141]) is a concern, “the electron acceleration is limited by synchrotron cooling”. Then, the electron spectrum becomes not a single PL but has a cooling break, where X-ray-emitting electrons with energy E is bigger than the cooling break energy E_b, determined by the equality of synchrotron cooling time and the age of the SNR ($t_{syn}(E_b) = t_{age}$), while, “electrons suffer energy loss via synchrotron cooling during the acceleration, and this causes a steepening of the energy spectrum” [39]. In order to test this situation, *cutoffpl* model was used to derive $E_{max,e}$ (for further steps of the process see Section 6.1). In the case of the cooling break, shock velocity, maximum energy of electrons and protons can be calculated with the formulae below:

Shock velocity can be derived from, [109]

$$\varepsilon_0 = 0.55 \left(\frac{v_s}{3000\ kms^{-1}}\right)^2 \eta^{-1}\ [\mathrm{keV}] \tag{5.6}$$

Maximum energy of electrons can be derived from, [143]

$$\varepsilon_0 = 5.3 \left(\frac{B}{10\ \mu G}\right) \left(\frac{E_{max,e}}{100\ TeV}\right)^2 [\mathrm{keV}] \tag{5.7}$$

Maximum energy of protons [141]

$$E_{max,p} = 83 \left(\frac{E_{max,e}}{10\ TeV}\right)^2 \left(\frac{B}{100\ \mu G}\right)^2 \left(\frac{t_{age}}{10^3\ yr}\right) [\mathrm{TeV}] \tag{5.8}$$

Table 5.35 First results of calculations of $E_{max,e}$ for Cas A. (BGD-1 subtracted spectra)

SNR	**$\nu_{roll\text{-}off}$ (10^{16} Hz)**	**B (μG)**	**t_{age} (yr)**	**v_s (10^8 cms^{-1})**	**$E_{max,e}$ (TeV)**
Cas A Region#2	33.29 ± 1.19	230*	325**	3.62 ± 0.12	18.12 ± 0.60
Cas A Region#3	170.13 ± 16.97	230*	325**	18.50 ± 0.45	92.58 ± 2.25

*: [144], **: [145]

Table 5.36 First results of calculations of $E_{max,e}$ for RCW 86. (BGD-1 subtracted spectra).

SNR	**$\nu_{roll\text{-}off}$ (10^{16} Hz)**	**B (μG)**	**t_{age} (yr)**	**v_s (10^8 cms^{-1})**	**$E_{max,e}$ (TeV)**
RCW 86 Region#1	4.75 ± 0.27	80*	1630**	0.52 ± 0.06	4.41 ± 0.51
RCW 86 Region#2	8.16 ± 0.60	80*	1630**	0.89 ± 0.08	7.55 ± 0.69

*: [146], **: [147]

Table 5.37 First results of calculations of $E_{max,e}$ for RX J1713.7−3946. (BGD-1 subtracted spectra).

SNR	**$\nu_{roll-off}$ (10^{17} Hz)**	**B (μG)**	**t_{age} (yr)**	**v_s (10^8 cms^{-1})**	**$E_{max,e}$ (TeV)**
RX J1713.7−3946 (NW) Region#1	2.53 ± 0.16	77*	1580 – 2100**	2.75 ± 0.14	23.78 ± 1.21
RX J1713.7−3946 (NW) Region#2	6.32 ± 0.42	77*	1580 – 2100**	6.87 ± 0.22	59.42 ± 1.90
RX J1713.7−3946 (NW) Region#3	8.87 ± 0.77	77*	1580 – 2100**	9.64 ± 0.30	83.38 ± 2.59
RX J1713.7−3946 (SW) Region#1	6.30 ± 0.67	77*	1580 – 2100**	6.85 ± 0.28	59.25 ± 2.42
RX J1713.7−3946 (SW) Region#2	2.09 ± 0.15	77*	1580 – 2100**	2.27 ± 0.13	19.63 ± 1.12

*: [144], **: [116]

Table 5.38 First results of calculations of $E_{max,e}$ for SN 1006. (BGD-1 subtracted spectra).

SNR	**$\nu_{roll\text{-}off}$ (10^{16} Hz)**	**B (μG)**	**t_{age} (yr)**	**v_s (10^8 cms^{-1})**	**$E_{max,e}$ (TeV)**
SN 1006 (NW) Region#1	7.03 ± 0.16	90*	~1011**	0.76 ± 0.04	6.08 ± 0.32
SN 1006 (NW) Region#2	4.44 ± 0.12	90*	~1011**	0.48 ± 0.04	3.84 ± 0.32
SN 1006 (S) Region#1	9.37 ± 0.27	90*	~1011**	1.02 ± 0.06	8.16 ± 0.48
SN 1006 (S) Region#1	5.93 ± 0.10	90*	~1011**	0.64 ± 0.03	5.12 ± 0.24
SN 1006 (SE) Region#1	5.42 ± 0.10	90*	~1011**	0.59 ± 0.03	4.72 ± 0.24
SN 1006 (SW) Region#1	7.69 ± 0.18	90*	~1011**	0.84 ± 0.04	6.72 ± 0.32
SN 1006 (SW) Region#2	6.92 ± 0.15	90*	~1011**	0.75 ± 0.04	6.00 ± 0.32
SN 1006 (W) Region#1	5.96 ± 0.12	90*	~1011**	0.65 ± 0.04	5.20 ± 0.32
SN 1006 (W) Region#2	8.00 ± 0.25	90*	~1011**	0.87 ± 0.05	6.96 ± 0.40
SN 1006 (W) Region#3	7.06 ± 0.20	90*	~1011**	0.77 ± 0.05	6.16 ± 0.40

*: [144], **: [148]

Table 5.39 First results of calculations of $E_{max,e}$ for Vela Jr. (BGD-1 subtracted spectra).

SNR	**$\nu_{roll\text{-}off}$ (10^{17} Hz)**	**B (μG)**	**t_{age} (yr)**	**v_s (10^8 cms^{-1})**	**$E_{max,e}$ (TeV)**
Vela Jr. (N) Region#1	1.33 ± 0.03	500*	2400 – 5100**	1.45 ± 0.06	4.92 ± 0.20
Vela Jr. (NW) Region#1	1.01 ± 0.05	500*	2400 – 5100**	1.10 ± 0.08	3.73 ± 0.27
Vela Jr. (NW) Region#2	0.78 ± 0.04	500*	2400 – 5100**	0.85 ± 0.07	2.88 ± 0.24
Vela Jr. (NW) Region#3	2.70 ± 0.07	500*	2400 – 5100**	2.93 ± 0.09	9.94 ± 0.30

*: [129], **: [133]

Table 5.40 Second results of calculations of $E_{max,e}$ for Cas A. (BGD-2 subtracted spectra).

SNR	**$\nu_{roll\text{-}off}$ (10^{16} Hz)**	**B (μG)**	**t_{age} (yr)**	**v_s (10^8 cms^{-1})**	**$E_{max,e}$ (TeV)**
Cas A Region#2	33.24 ± 1.20	230*	325**	3.61 ± 0.12	18.07 ± 0.60
Cas A Region#3	315.44 ± 38.57	230*	325**	34.27 ± 0.67	296.40 ± 5.79

*: [144], **: [145]

Table 5.41 Second results of calculations of $E_{max,e}$ for RCW 86. (BGD-2 subtracted spectra).

SNR	**$\nu_{roll\text{-}off}$ (10^{16} Hz)**	**B (μG)**	**t_{age} (yr)**	**v_s (10^8 cms^{-1})**	**$E_{max,e}$ (TeV)**
RCW 86 Region#1	8.80 ± 0.29	80*	1630**	0.97 ± 0.06	8.23 ± 0.51
RCW 86 Region#2	8.52 ± 0.16	80*	1630**	0.93 ± 0.04	7.89 ± 0.34

*: [146], **: [147]

Table 5.42 Second results of calculations of $E_{max,e}$ for RX J1713.7−3946. (BGD-2 subtracted spectra).

SNR	$\nu_{roll\text{-}off}$ (10^{17} Hz)	B (μG)	t_{age} (yr)	v_s (10^8 cms^{-1})	$E_{max,e}$ (TeV)
RX J1713.7−3946 (NW) Region#1	2.10 ± 0.12	77*	1580 – 2100**	2.28 ± 0.12	19.72 ± 1.04
RX J1713.7−3946 (NW) Region#2	4.74 ± 0.29	77*	1580 – 2100**	5.15 ± 0.18	44.54 ± 1.56
RX J1713.7−3946 (NW) Region#3	6.55 ± 0.50	77*	1580 – 2100**	7.12 ± 0.24	61.58 ± 2.07
RX J1713.7−3946 (SW) Region#1	7.69 ± 0.88	77*	1580 – 2100**	8.36 ± 0.32	72.31 ± 2.77
RX J1713.7−3946 (SW) Region#2	2.06 ± 0.15	77*	1580 – 2100**	2.24 ± 0.13	19.37 ± 1.12

*: [144], **: [116]

Table 5.43 Second results of $E_{max,e}$ for SN 1006. (BGD-2 subtracted spectra)

SNR	$\nu_{roll\text{-}off}$ (10^{16} Hz)	B (μG)	t_{age} (yr)	v_s (10^8 cms^{-1})	$E_{max,e}$ (TeV)
SN 1006 (NW) Region#1	11.84 ± 0.29	90*	~1011**	1.29 ± 0.06	10.32± 0.48
SN 1006 (NW) Region#2	6.68 ± 0.19	90*	~1011**	0.73 ± 0.05	5.84 ± 0.40
SN 1006 (S) Region#1	10.70 ± 0.48	90*	~1011**	1.16 ± 0.08	9.28 ± 0.64
SN 1006 (S) Region#1	7.25 ± 0.20	90*	~1011**	0.79 ± 0.05	6.32 ± 0.40
SN 1006 (SE) Region#1	6.36 ± 0.12	90*	~1011**	0.69 ± 0.04	5.52 ± 0.32
SN 1006 (SW) Region#1	9.11 ± 0.23	90*	~1011**	0.99 ± 0.05	7.92 ± 0.40
SN 1006 (SW) Region#2	3.92 ± 0.07	90*	~1011**	0.43 ± 0.03	3.44 ± 0.24
SN 1006 (W) Region#1	7.66 ± 0.16	90*	~1011**	0.83 ± 0.04	6.64 ± 0.32
SN 1006 (W) Region#2	10.05 ± 0.33	90*	~1011**	1.09 ± 0.06	8.72 ± 0.48
SN 1006 (W) Region#3	8.00 ± 0.23	90*	~1011**	0.87 ± 0.05	6.96 ± 0.40

*: [144], **: [148]

Table 5.44 Second results of calculations of $E_{max,e}$ for Vela Jr. (BGD-2 subtracted spectra).

SNR	**$\nu_{roll\text{-}off}$ (10^{17} Hz)**	**B (μG)**	**t_{age} (yr)**	**v_s (10^8 cms^{-1})**	**$E_{max,e}$ (TeV)**
Vela Jr. (N) Region#1	2.07 ± 0.05	500*	2400 – 5100**	2.25 ± 0.08	7.64 ± 0.27
Vela Jr. (NW) Region#1	1.11 ± 0.04	500*	2400 – 5100**	1.21 ± 0.07	4.11 ± 0.24
Vela Jr. (NW) Region#2	0.85 ± 0.04	500*	2400 – 5100**	0.92 ± 0.07	3.12 ± 0.24
Vela Jr. (NW) Region#3	3.33 ± 0.08	500*	2400 – 5100**	3.62 ± 0.10	12.29 ± 0.34

*: [129], **: [133]

CHAPTER 6

DISCUSSION AND CONCLUSION

6.1 Discussion

In this thesis, the spectral analysis has been done for the targeted emission regions on five SNRs (Cas A, RCW 86, RX J1713.7−3946, SN 1006, and Vela Jr.) in the previous chapters. In this discussion section, summarised results for these regions from Chapter 5 were gathered. As mentioned before, making contribution to search for PeV energy in SNRs, and understand the physical process of this energy were aimed in this study.

The observations with *Chandra* and *XMM-Newton* have enabled us to derive detailed X-ray spectral parameters, such as roll-off frequencies. These parameters enable us to calculate the maximum energy of protons and electrons that pro-argument values of CR acceleration. Furthermore, these observatories give us an excellent opportunity through their high spectral resolutions to compare the results of the background estimation method, which is an important topic in recent years for a precise spectral analysis. Adding to these, understanding the NT X-ray emission in shell-type SNRs with a comparative approach is a highlighter processes to ideate the synchrotron X-ray nature of them, which is caused by high-energy electrons in the amplified magnetic field, and still remains as an issue of concern. To sum up, we studied CR acceleration from shell-type SNRs as well as laying emphasis on the background estimation.

For the spectral analysis, we used NT models (e.g., *cutoffpl*, *srcut*) as described in Section 5 to estimate the important parameters. Magnetic field values found in previous studies are one of the key concerns. Because of the particles accelerated up to high energies interact with the magnetic field, and emit synchrotron emission within a range of radio to X-ray band. Synchrotron X-rays are emitted by accelerated electrons with the high energies in ≳TeV energy [39]. Also, in the shock regions of the SNR, the amplification of the magnetic field due to CRs has an effect on both the acceleration process and the emission from the accelerated particle population. In other words, as relevant particle acceleration is active, the magnetic field amplification due to CR-induced instabilities eventually may occur and achieve a condition of $\delta B/B \gg 1$, not only in the downstream field, but even in the upstream region (e.g. [149]). Furthermore, the maximum energy of the electrons highly depends on the explosion energy and the environment of the SNR. In the strong magnetic field environment, SNRs accelerate and decelerate electrons rapidly. In the low magnetic field environment, acceleration of the electrons occurs slowly, and they are accelerated up to higher energies.

There are several methods for the calculations of the magnetic field value: assuming TeV γ-ray emission is leptonic Inverse-Compton emission (e.g., [103], [151]) (but this result has not been established yet), or finding the maximum value of the field strength from the hot spots in the downstream regions (e.g., [150]). As a result of these circumstances, the magnetic field values were chosen according to the method used in the literature pointing the thickness of synchrotron X-rays. Various authors (e.g., [144], [152]) reported that whether the magnetic field strength of the PS region is firmly associated with the width of the X-ray synchrotron emitting filaments, where width of them occurs from a sequence of the velocity. This method extracts "average magnetic field strength" in the downstream regions. For a related estimation, we used the magnetic field values which were calculated by the same method in the literature. At that point, if "strong magnetic field" ($B \sim 0.1$–1 mG [141]) is the concern, "the electron acceleration process" is limited by the synchrotron cooling mechanism. Formerly, the electron spectrum becomes not a single PL, but has a cooling break, where X-ray-emitting electrons with energy, E, is bigger than the cooling break energy, E_b, determined by the equality of synchrotron cooling time and the age of the SNR ($t_{syn}(E_b) = t_{age}$), while, electrons suffer from energy loss over the synchrotron cooling during the acceleration, and at that time this the energy spectrum steepens [153]. In order to test this situation, we used *cutoffpl* model to estimate the $E_{max,e}$. Because in the strong magnetic field case, single PL assumption of the *srcut* model for electron spectrum is broken. Avoiding from this problem could be tested by employing the *cutoffpl* model which includes the "cut-off energy in the X-ray spectrum". This implies that the electron acceleration proceeds close to the "Bohm diffusion limit" [153]. However, *cutoffpl* model was not fitted well for the chosen regions of each SNR with very high (> 400 keV) value of e-folding energy of exponential roll-off. It may be due to lack of statistics and lack of energy band. This may indicate that the spectrum could be fit with a simple PL model. Nevertheless, before completely deciding on the using *srcut*, we endeavoured fitting the spectrum with fixing the photon index of *cutoffpl* which is found in the simple PL fittings, to ensure about what model to use correctly. Statistically (χ_ν^2 ~ 1.2) and physically acceptable (E_{cutoff} ~ 2.11 keV with non-modelled background, and ~1.78 keV with modelled background) *cutoffpl* fitting was found just for the region#2 of RCW 86. ν_s and $E_{max,e}$ were found as $3.23^{+1.81}_{-1.54}$ × 10^8 cms^{-1}, and $4.98^{+1.56}_{-1.13}$ TeV, for non-modelled background subtracted spectral results, and $2.97^{+1.49}_{-1.30}$ × 10^8 cms^{-1}, $4.20^{+1.06}_{-0.80}$ TeV for modelled background subtracted spectral results. While the spectra of the regions of the other SNRs were roughly represented by the *PL* model. In this case, the cut-off is not valid for the statistic point of view. For all regions of the SNRs, the PL Γ values are consistent with each other. Hence, the spectra do not need significant cut-off.

Table 5.1 shows five of the Galactic SNRs, which have synchrotron X-ray emission, with observational parameters. Note that our analysis sample does not include G1.9+0.3, one of the young SNR with synchrotron X-rays [154], [155]. We used this SNR's roll-off frequency, the maximum energy of electrons, shock velocity, and age values from the previous studies in the literature for the comparison to test the argument that as the remnant ages, v_s decreases and ν_{roll} becomes smaller, as well, and so does the roll-off energy [153]. The age of G1.9+0.3 (~100 yr) is younger than Cas A (~325 yr). In the interest of demonstrating the argument, we used the NT models to calculate maximum energies of particles (listed in Table 5.35 – 5.44). Figure 6.1 and Figure 6.2 shows the ν_{roll} dependence with SNR age. In the free expansion phase of the SNR, ν_{roll} increases in proportion to the age. Our results indicate the relation between the aging of the SNR, and decreasing roll-off frequency (see Figure 6.1 and Figure 6.2). As seen in the plots mentioned, as age increases the roll-off frequency decreases except one situation: In spite of G1.9+03, the youngest SNR in the Milky Way, the Region#2 on Cas A has bigger roll-off frequency. On the other hand, even SN 1006 is younger than the SNRs RX J1713.7−3946, and Vela Jr., it has almost identical or smaller ν_{roll} value in comparison with them.

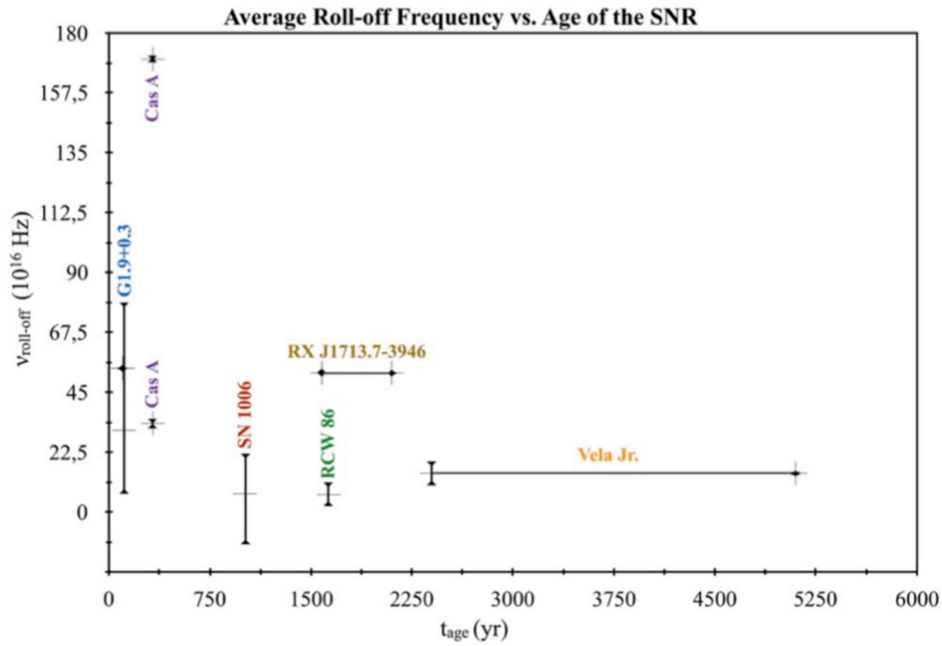

Averaged data were adopted for all the targeted regions. The values obtained by BGD-1 subtracted spectra.

Figure 6.1 First results of the correlation between the roll-off frequency (ν_{roll}) and the age of the SNR (t_{age}).

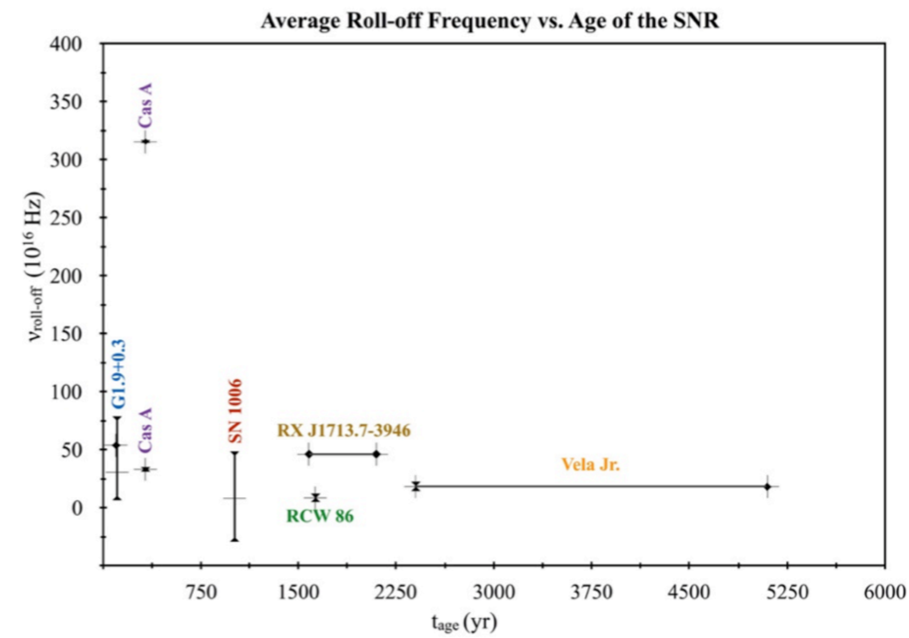

Averaged data were adopted for all the targeted regions. The values obtained by BGD-2 subtracted spectra.

Figure 6.2 Second results of the correlation between the roll-off frequency (ν_{roll}) and the age of the SNR (t_{age}).

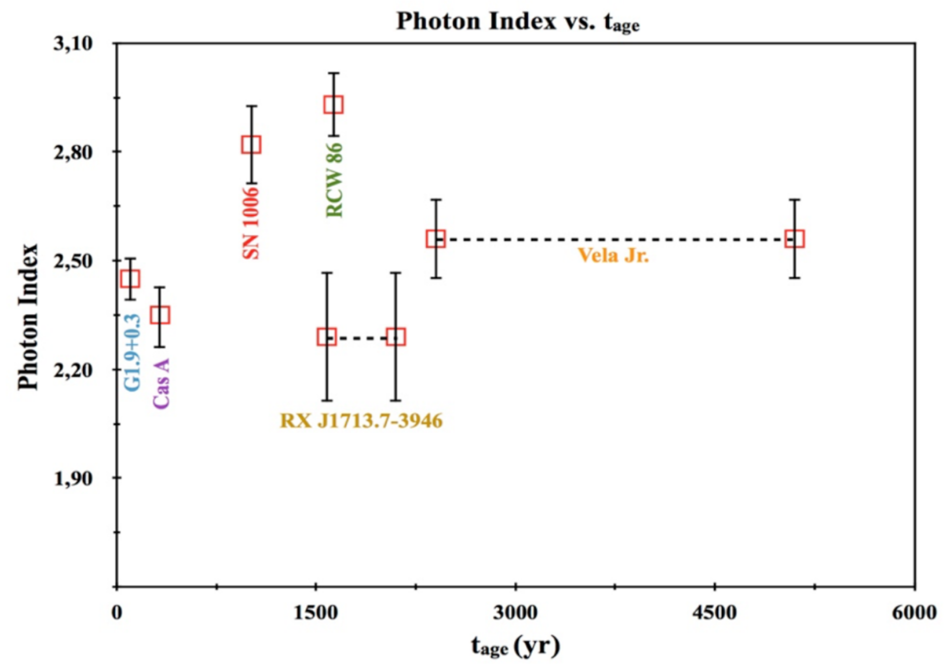

Averaged data were adopted for all the targeted regions. The values obtained by BGD-1 subtracted spectra.

Figure 6.3 First results of the correlation between the photon index and the age of the SNR.

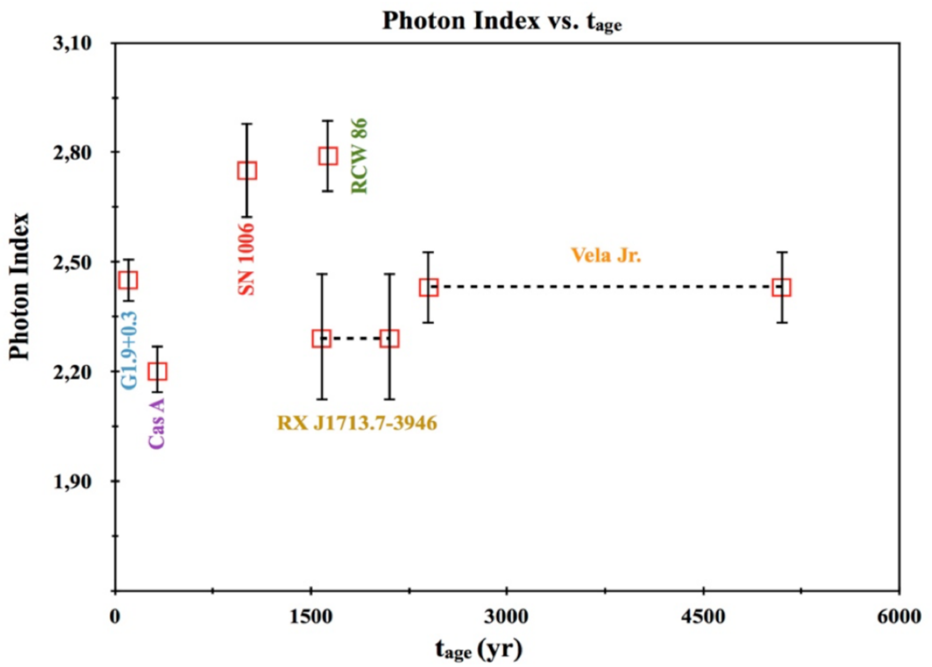

Averaged data were adopted for all the targeted regions. The values obtained by BGD-2 subtracted spectra.

Figure 6.4 Second results of the correlation between the photon index and the age of the SNR.

Figure 6.3 and Figure 6.4 show the relation between the photon index values of the targeted spectral regions, and age of the SNRs. Very young SNRs (≲300 yrs) show harder synchrotron spectra. As they age further, the growth of the spectrum stops. The photon indices are converted into roll-off frequencies, $\nu_{roll\text{-}off}$, in *srcut* model, as shown in Figure 6.2 and Figure 6.3, as mentioned before. We must note that the parameter $\nu_{roll\text{-}off}$ is determined by indirect and complicated parameters, $E_{max,e}$ and B_d in eq. (5.5). For example, the condition of acceleration sites in Cas A may have stronger magnetic field than those in other SNRs, and it has much harder photon index and bigger value of roll-off frequency.

SNRs may contain both thermal and NT X-ray emission. The presence of the strong NT X-ray continuum can provide distinguishing of these remnants by the weakness of their lines [156]. RCW 86 has weak emission lines. These emission lines yield low and peculiar abundances when thermal models alone are used to interpret their X-ray spectra. Thus, this situation indicates the presence of a strong NT synchrotron continuum.

Our results show that in high shock velocities, $E_{max,e}$ value is higher. This result agrees with previous studies (e.g., [99], [157], [158]). They suggest that if $E_{max,e}$ is estimated by the balance between the acceleration and synchrotron cooling, the roll-off of synchrotron emission depends only on the v_s. Thus, the maximum energy of accelerating of the electrons is higher in high shock speed regions. This dependence is shown in Figure 6.5 and Figure 6.6, where two plots can be seen which show the values calculated from the results by non-modelled and modelled background subtracted spectra, respectively. The R^2 value represents the measure of the goodness of fit of the trendline to the data, which points that background modelling method is a necessary process for more reliable values.

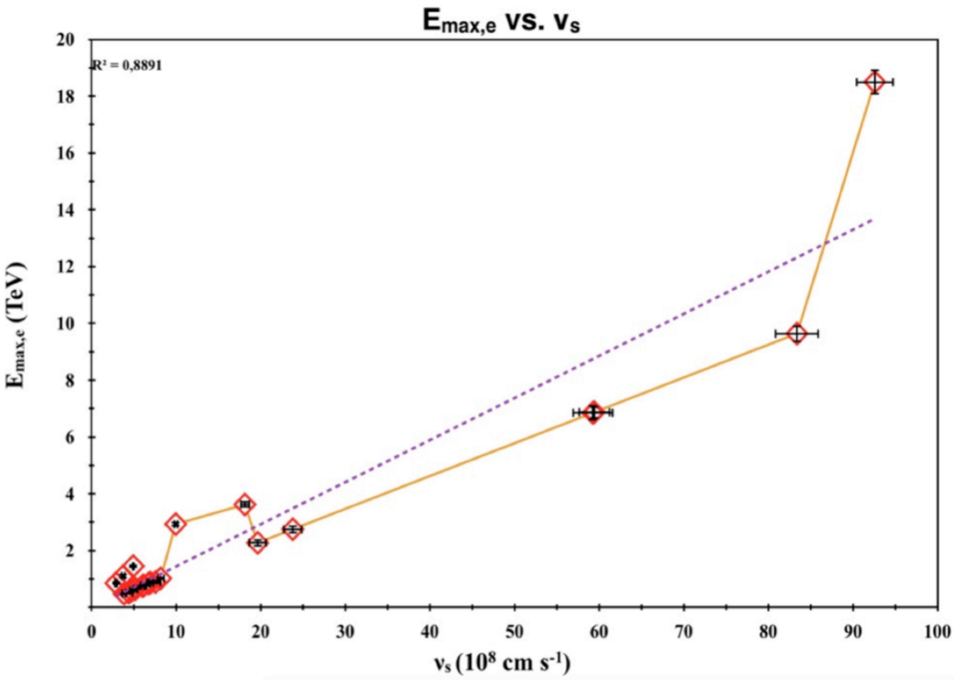

R^2 value represents the measure of the goodness of fit of the trendline to the data.

Figure 6.5 First plot of $E_{max,e}$ vs. v_s values, obtained by BGD-1 subtracted spectra.

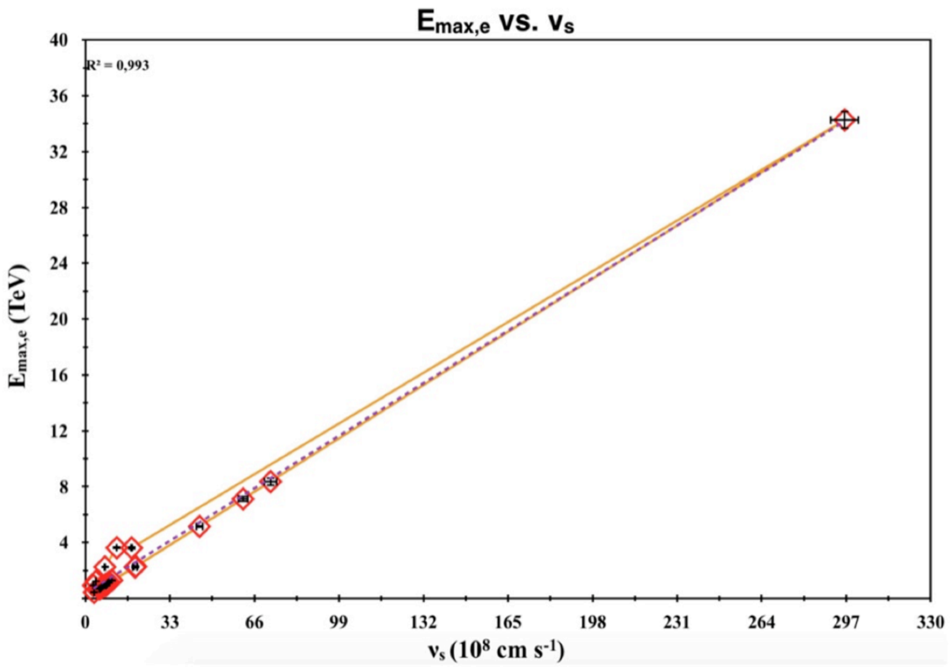

R^2 value represents the measure of the goodness of fit of the trendline to the data.

Figure 6.6 Second plot of $E_{max,e}$ vs. v_s values, obtained by BGD-2 subtracted spectra.

With *srcut* or *cutoffpl* XSPEC models, it is not a reliable approach to search for PeV energies with their inadequacy. This process requires high precision beyond the background modelling. Because, with the existing methods and ever-growing technology, there are new magnetic field calculations continuously in the literature, which is a main point to understand the particle acceleration via SNRs in high energies. The model *srcut* is consistent in the weak magnetic field, and also, the classic shape of *cutoffpl* model is not consistent in the strong magnetic field. Thus, as mentioned before, if strong magnetic field is an important concern, these existing theoretical models are insufficient.

6.2 Conclusion

We summarise the main results of our spectral analyses of the NT X-rays from Cas A, RCW 86, RX J1713.7−3946, SN 1006 and Vela Jr. with data of *Chandra* and *XMM-Newton* X-ray Observatories:

1. We found "hard regions" on the outer rims of the shells of Cas A, RCW 86, RX J1713.7−3946, SN 1006, and Vela Jr. The spectra of the regions are well reproduced by PL model which shows variations within each SNR from Γ = 2.10 – 2.58 for Cas A, from Γ = 2.79 – 3.01 for RCW 86, from Γ = 1.10 – 1.54 for RX J1713.7−3946, from Γ = 0.19 – 4.80 for SN 1006 and from Γ = 2.37 – 2.64 for Vela Jr. This PL X-ray emission at high energies from the SNRs, is most likely synchrotron X-ray from accelerated high energy electrons and protons.
2. Thermal X-ray emission was also detected from some shell regions on SN 1006 and RCW 86, and emission lines from Cas A. They have weak emission lines, as it can be distinguished by the weakness of these lines because of the presence of a strong NT X-ray continuum. It is known that both NT and thermal X-ray emission may be exhibited by the SNRs [156].
3. In the southern rim of the RCW 86, there is synchrotron X-rays in addition to weak thermal plasma emission. The emission spectra were represented with two-temperature non-equilibrium collisional ionisation plasma model plus simple PL model for Region#1 and Region#2 and only two-temperature non-equilibrium collisional ionisation plasma model for Region#3, which are absorbed through the interstellar column density (as seen in Table 5.35 – 5.44). RCW 86 has weak emission lines, as it can be distinguished by the weakness of these lines because

of the presence of a strong NT continuum. Modelling of X-ray spectra of the source regions on RCW 86 revealed the presence of the NT synchrotron emission, in addition to thermal components with two ejecta. The main purpose of this thesis is not to derive the thermal parameters, but to measure thermal emission generally, and to analyse the properties of X-ray synchrotron emission of the targeted regions by searching basically NT regions.

4. We estimated the v_s, and $E_{max,e}$, which have been accelerated in the shells of the remnants by the FS. Results can be seen in Table 5.35 – 5.44 for the non-modelled and modelled background subtracted spectra, respectively.
5. Our results show that in high shock velocities, the maximum energy of accelerated electrons is higher. This result agrees with previous studies (e.g., [99], [157], [158]).
6. We found that as the SNRs evolve, their X-ray spectra tend to become softer, and then may stop, according to their photon index values. This result agrees with a previous study [159].
7. The conducted results revealed that analysing an extended source with accurately modelled background emission might be effective on spectral results. In Figure 6.5 and Figure 6.6, effect of the modelled background spectra can be seen according to the R^2 value which develops with 10% change, and points that background modelling method might be a necessary process for more reliable values. On the other hand, in the other plots (Figure 6.1 − 6.4), a significant variation cannot be seen, which may become obvious with more samples.
8. It was estimated that some of the targeted emission regions of Cas A and Vela Jr. contain PeV energies, but this result need to be tested according to the insufficiency of the synchrotron models under XSPEC.

6.3 Future Prospects

Galactic SNRs that emit synchrotron X-rays are still remain important issue to study them statistically, and understand them basically. Also, with the existing theoretical NT models, it is not a reliable approach to search for PeV energies with their inadequacy. This process requires high precision beyond the background modelling, since it only has an effect of 10% on the goodness of the fit, as we discussed. That cannot be said that this method will provide a better result for the synchrotron fitting. However, with improvement of the existing methods and ever-growing technology, there are new magnetic field calculations continuously in the literature, which is a key point to examine the particle acceleration mechanisms in the young SNRs in high energies. Thus, as mentioned before, if strong magnetic field is the main concern, the existing XSPEC models are inadequate. Furthermore, the search for more samples and more reliable analysis methods might be required to get definite results, since current synchrotron models need to be retested and improved. On the other hand, in order to investigate synchrotron characteristics and origin for PeV energies, we should further explore other shock regions of these SNRs we chose in this study, with high statistics.

The present study will reveal the high shock speed regions, and their significance for the understanding of the efficient CR acceleration process, and their source in the young Galactic SNRs. Thus, targeted NT emitting regions on the young SNRs will be the focus of interest in the future work.

In this thesis, it has been shown that there has not been a model under XSPEC yet for the strong magnetic field values. Thus, a code for this model needs to be developed. In accordance with this purpose, we have started to work with a group of international researchers with this purpose as the future prospect.

REFERENCES

[1] Sawada, M., (2011). Plasma Diagnostics for Non-Standard Supernova Remnants in the Galactic Center Region, PhD. Thesis, Kyoto University, Graduate School of Science, Kyoto, Japan.

[2] Someya, K., (2012). A Systematic X-ray Study of Supernova Remnants in the Large Magellanic Cloud, PhD. Thesis, Tokyo Institute of Technology, Department of Physics, Tokyo, Japan.

[3] Yamaguchi, H., (2008). X-Ray Study of Ejecta-Dominated Supernova Remnants with Suzaku, PhD. Thesis, Kyoto University, Graduate School of Science, Kyoto, Japan.

[4] Woosley, S.E. and Weaver T.A., (1986). "The Physics of Supernova Explosions", IN: Annual Review of Astronomy and Astrophysics, 24(A87-26730 10-90):205-253.

[5] Langer, N. and Woosley, S.E., (1996). "Supernovae and Their Progenitors", ASP Conference Series, 98:220-231.

[6] Woosley, S. and Janka, T., (2005). "The Physics of Core-Collapse Supernovae", Nature Physics, 1: 147-154.

[7] Nadyozhin, D.K. and Imshennik, V.S., (2005). "Physics of Supernovae", International Journal of Modern Physics A, 20: 6597-6611.

[8] Sezer, A., (2007). Photometry and Spectrometry Analysis of Some Supernova Remnants, PhD. Thesis, Akdeniz University, Institute of Natural Sciences, Antalya, Turkey.

[9] Chaisson, E. and McMillan, S., (1997). Astronomy Today, Second Edition, Prentice Hall Inc., New Jersey.

[10] Uchida, H., (2010). X-ray Study of the Cygnus Loop Supernova Remnant, PhD. Thesis, Osaka University, Graduate School of Science, Osaka.

[11] Vink, J., (2012), "Supernova Remnants: The X-ray Perspective", Astronomy and Astrophysics Reviews, 20(1).

[12] Barbon, R., Ciatti, F., and Rosino, L., (1979). "Photometric Properties of Type II Supernovae", Astronomy & Astrophysics, 72(3):287-292.

[13] Filippenko, A.V., (1997). "Optical Spectra of Supernovae", Annual Reviews of Astronomy and Astrophysics, 35:309-355.

[14] Röpke, F.K., Seitenzahl, Benitez, S., Fink, M., Pakmor, R., Kromer, M., Sim,

S.A., Ciaraldi-Schoolmann, F. and Hillebrandt, W., (2011). “Modelling Type Ia Supernova Explosions”, Elsevier B.V. Progressive in Particle and Nuclear Physics, 66:309-318.

[15] Webbink, R.F., (1984), “Double White Dwarfs as Progenitors of R Coronae Borealis Stars and Type I Supernovae”, Astrophysical Journal, Part 1, 277:355-360.

[16] Iben Jr.,I. and Tutukov, A.V., (1984). “Supernovae of Type I as End Products of The Evolution of Binaries with Components of Moderate Initial Mass ($M \leq M_{\odot}$)”, The Astrophysical Journal Supplement Series, 54:335-372.

[17] Saio, H. and Nomoto, K., (1985). “Evolution of A Merging Pair of C + O White Dwarfs to Form A Single Neutron Star”, Astronomy & Astrophysics, 150(1):L21-L23.

[18] Nomoto, K., (1982). “Accreting White Dwarf Models for Type 1 Supernovae. II - Off-Center Detonation Supernovae”, Astrophysical Journal, Part 1, 257:780-792.

[19] Khokhlov, A.M., (1991). “Delayed detonation model for type IA supernovae”, Astronomy & Astrophysics, 245(1):114-128.

[20] Prialnik, D., (2000). “An Introduction to the Theory of Stellar Structure and Evolution”, Cambridge University Press, Cambridge.

[21] Heger, A., Fryer, C.L., Woosley, S.E., Langer, N. and Hartmann, D.H., (2003), “How Massive Single Stars End Their Life”, The Astrophysical Journal, 591(1):288-300.

[22] Lyne A.G. and Graham-Smith F., (1998). Pulsar Astronomy, Cambridge University Press, New York.

[23] Bhattacharya, D., (1990). “On the Morphology of Supernova Remnants with Pulsars”, Journal of Astrophysics and Astronomy, 11:125-140.

[24] Green D. A., A Catalogue of Galactic Supernova Remnants (2014 May version): http://www.mrao.cam.ac.uk/surveys/snrs/, 25 May 2014.

[25] Sedov, L.I., (1959). Similarity and Dimensional Methods in Mechanics, Academic Press, New York.

[26] Temim, T., (2009). Multi-wavelength Observations of Pulsar Wind Nebulae and Composite Supernova Remnants, PhD. Thesis, University of Minnesota, The Faculty of the Graduate School, Minnesota.

[27] McKee, C.F. and Ostriker, J.P., (1977). “A Theory of the Interstellar Medium – Three Components Regulated by Supernova Explosions in an Inhomogeneous Substrate”, Astrophysical Journal, Part 1, 218:148-169.

[28] Cioffi, D.F., McKee, C.F. and Bertschinger, E., (1988). “Dynamics of Radiative Supernova Remnants”, Astrophysical Journal, Part 1, 334:252-265.

[29] Gonzalez, M.E., (2003). Chandra X-ray Studies of the Supernova Remnants G292.0+1.8 and G292.2-0.5 Containing the Young Pulsars J1124-5916 and J1119-6127. MSc. Thesis, University of Manitoba, Department of Physics and Astronomy, Manitoba.

[30] Zarnecki, J. C., (1979). “Some Recent Observations of Supernova Remnants

Emitting X-Rays", Proceedings of the Royal Society of London. Series A, Mathematical and Physical Sciences, 366(1726):311–327.

[31] Arguedas, M. A. A., (2011). Non-Thermal Emission from Young Supernova Remnants Implications on Cosmic-ray Acceleration. PhD Thesis, Purdue University, Graduate School, Indiana.

[32] Perri, S., Amato, E. and Zimbardo, G., (2016). "Transport of Relativistic Electrons at Shocks in Shell-Type Supernova Remnants: Diffusive and Superdiffusive Regimes", Astronomy & Astrophysics, 596(A34):10.

[33] Safi-Harb, S., (2012). "Plerionic Supernova Remnants", High Energy Gamma-Ray Astronomy: 5th International Meeting on High Energy Gamma-Ray Astronomy. AIP Conference Proceedings, 1505:13-20.

[34] Kassim, N. E., Hertz, P., Weiler, K. W., (1993). "ROSAT Observations of the Composite Supernova Remnant G326.3-1.8", Astrophysical Journal, 419:733.

[35] Rho, J., Petre, R., (1998). "Mixed-Morphology Supernova Remnants", The Astrophysical Journal, 503(2):L167-L170.

[36] Torii, K., Tsunemi, H. and Slane, P., (1998). "X-Ray Study of Crab-Like and Composite SNRs", Symposium - International Astronomical Union, 188:258–259.

[37] Seward, F. D. and Charles, P. A., (2010). Exploring the X-ray Universe, Second Edition, Cambridge University Press, Cambridge.

[38] Sano, N. H., (2013). An Observational Study of Shock-Cloud Interaction in the Young VHE γ-ray SNR RX J1713.7−3946, Evidence for Cosmic-Ray Acceleration, PhD Thesis, Nagoya University, Department of Physics, Nagoya, Japan.

[39] Nakamura, R. (2010). A Study of Cosmic-Ray Acceleration History in Supernova Remnants through Observations of Synchrotron X-ray Radiation, PhD Thesis, Department of Physics, Tokyo Institute of Technology & The Institute of Space and Astronautical Science, Tokyo, Japan.

[40] Beatty J. J., and Westerhoff, S., (2009). "The Highest-Energy Cosmic-rays", Annual Review of Nuclear and Particle Science, 59:319-345.

[41] Bradt, H., (2004). Astronomy Methods: A Physical Approach to Astronomical Observations, Cambridge University Press, Cambridge.

[42] Gorenstein, P., (1977). In X-ray Astronomy, D. Reidel Publishing Company, Holland.

[43] Bryans, P., Badnell, N. R., Gorczyca, T. W., Laming, J. M., Mitthumsiri, W. and Savin, D. W., (2006). "Collisional Ionisation Equilibrium for Optically Thin Plasmas. I. Updated Recombination Rate Coefficients for Bare through Sodium-like Ions", The Astrophysical Journal Supplement Series, 167(2):343-356.

[44] Dalgarno, A. and Layzer, D., (1987). Spectroscopy of Astrophysical Plasmas, Cambridge University Press, Cambridge.

[45] Böhringer, H., (1997). "Equilibrium Ionisation and Non-Equilibrium Ionisation Plasma Models", International Astronomical Union Colloquium, 166:341–352.

[46] Reynolds, S. P., (2008). "Supernova Remnants at High Energy", Annual Review

of Astronomy and Astrophysics, 46(1):89-126.

[47] Blumenthal, G. R. and Gould, R. J., (1970). “Bremsstrahlung, Synchrotron Radiation, and Compton Scattering of High-Energy Electrons Traversing Dilute Gases”, Reviews of Modern Physics, 42(2):237-271.

[48] Bordovitsyn, V. A. and Ternov, I. M., (1999). Synchrotron Radiation Theory and Its Development: In Memory of I.M. Ternov, World Scientific Publishing Co. Pte. Ltd., Singapore.

[49] Garmire, G. P., Bautz, M. W., Ford, P. G., Nousek, J. A. and Ricker, G. R., Jr., (2003). “Advanced CCD imaging spectrometer (ACIS) instrument on the Chandra X-ray Observatory”, X-Ray and Gamma-Ray Telescopes and Instruments for Astronomy. Edited by Joachim E. Truemper, Harvey D. Tananbaum. Proceedings of the SPIE, 4851:28-44.

[50] Kushino, A., Ishisaki, Y., Morita, U., Yamasaki, N. Y., Ishida, M., Ohashi, T. and Ueda, Y., (2002). “Study of the X-Ray Background Spectrum and Its Large-Scale Fluctuation with ASCA”, Publications of the Astronomical Society of Japan, 54(3):327-352.

[51] Ebisawa, K., Maeda, Y., Kaneda, H. and Yamauchi, S., (2001). “Origin of the Hard X-ray Emission from the Galactic Plane”, Science, 293(5535):1633-1635.

[52] Ebisawa, K., Tsujimoto, M., Paizis, A., Hamaguchi, K., Bamba, A., Cutri, R., Kaneda, H., Maeda, Y., Sato, G., Senda, A., Ueno, M., Yamauchi, S., Beckmann, V., Courvoisier, T. J.-L., Dubath, P. and Nishihara, E., (2005). “Chandra Deep X-Ray Observation of a Typical Galactic Plane Region and Near-Infrared Identification”, The Astrophysical Journal, 635(1):214-242.

[53] Ebisawa, K., Yamauchi, S., Tanaka, Y., Koyama, K., Ezoe, Y., Bamba, A., Kokubun, M., Hyodo, Y., Tsujimoto, M. and Takahashi, H., (2008). “Spectral Study of the Galactic Ridge X-Ray Emission with Suzaku”, Publications of the Astronomical Society of Japan, 60:223-230.

[54] Uchiyama, H., Nobukawa, M., Tsuru, T. G. and Koyama, K., (2013). “K-Shell Line Distribution of Heavy Elements along the Galactic Plane Observed with Suzaku”, Publications of the Astronomical Society of Japan, 65(1).

[55] Kaneda, H., Makishima, K., Yamauchi, S., Koyama, K., Matsuzaki, K. and Yamasaki, N. Y., (1997). “Complex Spectra of the Galactic Ridge X-Rays Observed with ASCA”, The Astrophysical Journal, 491(2):638-652.

[56] Liu, W., Chiao, M., Collier, M. R., Cravens, T., Galeazzi, M., Koutroumpa, D., Kuntz, K. D., Lallement, R., Lepri, S. T., McCammon, D., Morgan, K., Porter, F. S., Snowden, S. L., Thomas, N. E., Uprety, Y., Ursino, E. and Walsh, B. M., (2017). “The Structure of the Local Hot Bubble”, 834(1).

[57] Henley, D. B. and Shelton, R. L., (2013). “An XMM-Newton Survey of the Soft X-Ray Background. III. The Galactic Halo X-Ray Emission”, The Astrophysical Journal, 773(2).

[58] Ryu, S. G., Koyama, K., Nobukawa, M., Fukuoka, R., T. and Takeshi G., (2009). “An X-Ray Face-On View of the Sagittarius B Molecular Clouds Observed with Suzaku”, Publications of the Astronomical Society of Japan, 61(4):751-761.

[59] Kavanagh, P. J., Sasaki, M., Whelan, E. T., Maggi, P., Haberl, F., Bozzetto, L.

M., Filipović, M. D. and Crawford, E. J., (2015). “XMM-Newton Observation of SNR J0533–7202 in the Large Magellanic Cloud”, Astronomy and Astrophysics, 579(A63).

[60] Wilms, J., Allen, A. and McCray, R., (2000). “On the Absorption of X-Rays in the Interstellar Medium”, The Astrophysical Journal, 542(2):914-924.

[61] Vink, J., Bloemen, H., Kaastra, J. S. and Bleeker, A. M., (1998). “The Expansion of Cassiopeia A as Seen in X-Rays”, Astronomy and Astrophysics, 339:201-207.

[62] Hughes, J. P., Rakowski, C. E, Burrows, D. N. and Slane, P. O., (2000). “Nucleosynthesis and Mixing in Cassiopeia A”, The Astrophysical Journal, 528(2):L109-L113.

[63] Berendse, F., Holt, S. S., Petre, R. and Hwang, U. (2001). “X-ray Synchrotron in the Forward Shock of Cassiopeia A”, AIP Conference Proceedings, 399(2001):565.

[64] Gotthelf, E. V., Koralesky, B., Rudnick, L. Jones, T. W., Hwang, U. and Petre, R., (2001). “Chandra Detection of the Forward and Reverse Shocks in Cassiopeia A”, The Astrophysical Journal, 552(1):L39-L43.

[65] Vink, J., Laming, J. M., Kaastra, J. S., Bleeker, J. A. M., Bloemen, H. and Oberlack, U., (2001). “Detection of the 67.9 and 78.4 keV Lines Associated with the Radioactive Decay of ^{44}Ti in Cassiopeia A”, The Astrophysical Journal, 560(1):L79-L82.

[66] Willingale, R., Bleeker, J. A. M., van der Heyden, K. J., Kaastra, J. S. and Vink, J. (2002). “X-ray spectral imaging and Doppler mapping of Cassiopeia A”, Astronomy and Astrophysics, 381:1039-1048.

[67] DeLaney, T. and Rudnick, L., (2003). “The First Measurement of Cassiopeia A's Forward Shock Expansion Rate”, The Astrophysical Journal, 589(2):818-826.

[68] Rothschild, R. E. and Lingenfelter, R. E., (2003). “Limits to the Cassiopeia A ^{44}Ti Line Flux and Constraints on the Ejecta Energy and the Compact Source”, The Astrophysical Journal, 582(1):257-261.

[69] DeLaney, T., Rudnick, L., Jones, T. W., Fesen, R., Hwang, U., Petre, R. and Morse, J., (2004). “X-ray, Radio and Optical Observations of Cassiopeia A”, X-Ray and Radio Connections, 3-6 February, New Mexico.

[70] Motizuki, Y. and Kumagai, S., (2004). “^{44}Ti Radioactivity in Young Supernova Remnants: Cas A and SN 1987A”, New Astronomy Reviews, 48(1-4):69-73.

[71] Decourchelle, A., (2004). “Elemental Composition and Distribution in SNRs: X-ray Spectroscopy”, New Astronomy Reviews, 48(1-4):75-79.

[72] Hwang, U., Laming, J. M., Badenes, C., Berendse, F., Blondin, J., Cioffi, D., DeLaney, T., Dewey, D., Fesen, R., Flanagan, K. A, Fryer, C. L., Ghavamian, P., Rudnick, L., Sankrit, R., Slane, P. O., Smith, R. K., Vink, J., and Warren, J. S., (2004). “A Million Second Chandra View of Cassiopeia A”, The Astrophysical Journal, 615(2):L117-L120.

[73] DeLaney, T., Rudnick, L., Fesen, R. A., Jones, T. W., Petre, R. and Morse, J. A., (2004). “Kinematics of X-Ray-Emitting Components in Cassiopeia A”, The Astrophysical Journal, 613(1):343-348.

[74] Lazendic, J. S., Dewey, D., Schulz, N. S. and Canizares, C. R., (2006). “The Kinematic and Plasma Properties of X-Ray Knots in Cassiopeia A from the Chandra HETGS”, The Astrophysical Journal, 651(1):250-267.

[75] Yang, X., Lu, F. and Chen, L., (2008). “High Spatial Resolution X-Ray Spectroscopy of Cas A with Chandra”, Chinese Journal of Astronomy and Astrophysics, 8(4):439-450.

[76] Helder, E. A. and Vink, J., (2008). “Characterizing the Nonthermal Emission of Cassiopeia A”, The Astrophysical Journal, 686(2):1094-1102.

[77] Hwang, U. and Laming, J. M., (2009). “The Circumstellar Medium of Cassiopeia A Inferred from the Outer Ejecta Knot Properties”, The Astrophysical Journal, 703(1):883-893.

[78] Maeda, Y., Uchiyama, Y., Bamba, A., Kosugi, H., Tsunemi, H., Helder, E. A., Vink, J., Kodaka, N., Terada, Y., Fukuzawa, Y., Hiraga, j., Hughes J. P., Kokubun, M., Kouzu, T., Matsumoto, H., Miyata, E., Nakamura, R., Okada, S., Someya, K., Tamagawa, T., Tamura, K., Totsuka, K., Tsuboi, Y., Ezoe, Y., Holt, S. S., Ishida, M., Kamae, T., Petre, R. and Takahashi, T., (2009). “Suzaku X-Ray Imaging and Spectroscopy of Cassiopeia A”, Publications of the Astronomical Society of Japan, 61(6):1217-1228.

[79] Araya, M., Lomiashvili, D., Chang, C., Lyutikov, M. and Cui, W., (2010). “Probing Shock Properties with Nonthermal X-ray Filaments in Cas A”. The Astrophysical Journal, 714(1): 396-403.

[80] DeLaney, T., Rudnick, Stage, M. D., Smith, J. D., Isense, K. Rho, J., Allen, G. E., Gomez, H., Kozasa, T., Reach, W. Davis, J. E. and Houck, J. C., (2010). “The Three-dimensional Structure of Cassiopeia A”, The Astrophysical Journal, 725(2):2038-2058.

[81] Hainke, C. O. and Ho, W. C. G., (2010). “Direct Observation of the Cooling of the Cassiopeia A Neutron Star”, The Astrophysical Journal Letters, 719(2):L167-L171.

[82] Elshamouty, K. G., Heinke, C. O., Sivakoff, G. R., Ho, W. C. G., Shternin, P. S., Yakovlev, D. G., Patnaude, D. J. and David, L., (2013). “Measuring the Cooling of the Neutron Star in Cassiopeia A with all Chandra X-Ray Observatory Detectors”, The Astrophysical Journal, 777(1).

[83] Hwang, U. and Laming, J. M., (2012). “A Chandra X-Ray Survey of Ejecta in the Cassiopeia A Supernova Remnant”, The Astrophysical Journal, 746(2).

[84] Maeda, Y., Sato, T., Tsunemi, H., Bamba, A., Vink, J., Terada, Y., Takeda, T., Sawada, M., Gandhi, P., Matsumoto, H., Uchiyama, Y., Helder, E. A., Hiraga, J., Hughes, J. P., Kokubun, M., Tamagawa, T. and Tsuboi, Y., (2014). “X-ray Imaging of the Cr and Fe Lines from Cassiopeia A”, Suzaku-MAXI 2014: Expanding the Frontiers of the X-ray Universe, 19-22 September 2014, Matsuyama.

[85] Lee, J., Park, Sangwook, Hughes, J. P. and Slane, P. O., (2014). “X-Ray Observation of the Shocked Red Supergiant Wind of Cassiopeia A”, The Astrophysical Journal, 789(1).

[86] Grefenstette, B. W., Reynolds, S. P.,Harrison, F. A., Humensky, T. B., Boggs, S. E., Fryer, C. L., DeLaney, T., Madsen, K. K., Miyasaka, H.,

Wik, D. R., Zoglauer, A., Forster, K., Kitaguchi, T., Lopez, L., Nynka, M., Christensen, F. E., Craig, W. W., Hailey, C. J., Stern, D. and Zhang, W. W., (2015). "Locating the Most Energetic Electrons in Cassiopeia A", The Astrophysical Journal, 802(1).

[87] Krivonos, R., Revnivtsev, M., Churazov, E., Sazonov, S., Grebenev, S., and Sunyaev, R., (2007). "INTEGRAL/IBIS all-sky survey in hard X-rays", Astronomy and Astrophysics, 475(2):775-784.

[88] Kalberla, P. M. W., Burton, W. B., Hartmann, D., Arnal, E. M., Bajaja, E., Morras, R., Pöppel, W. G. L., (2005). "The Leiden/Argentine/Bonn (LAB) Survey of Galactic HI. Final Data Release of the Combined LDS and IAR Surveys with Improved Stray-radiation Corrections", Astronomy & Astrophysics, 440(2):775-782.

[89] Masui, K., Mitsuda, K., Yamasaki, N. Y., Takei, Y., Kimura, S., Yoshino, T. and McCammon, D., (2008). "The Nature of Unresolved Soft X-ray Emission from the Galactic Disk", Publications of the Astronomical Society of Japan, 61:115-122.

[90] Bamba, A., Koyama, K. and Tomida, H., (2000). "Discovery of Non-Thermal X-Rays from the Shell of RCW 86", Publications of the Astronomical Society of Japan, (52):1157-1163.

[91] Vink, J., Bocchino, F., Damiani, F. and Kaastra, J. S., (2000). "An Unresolved X-ray Source Inside the Supernova Remnant RCW 86", Astronomy & Astrophysics, 362:711-714.

[92] Vink, J., Bleeker, J., Kaastra, J., van der Heyden, K. and Dicke, J., (2002). "XMM-Newton Observations of MSH 14-63 (RCW 86)", Neutron Stars in Supernova Remnants, ASP Conference Series, 14-17 August 2001, Boston.

[93] Rho, J., Dyer, K. K., Borkowski, K. J. and Reynolds, S. P., (2002). "X-Ray Synchrotron-emitting Fe-rich Ejecta in Supernova Remnant RCW 86", The Astrophysical Journal, 581(2):1116-1131.

[94] Yamaguchi, H., Koyama, K., Nakajima, H., Bamba, A., Yamazaki, R., Vink, J. and Kawachi, A., (2008). "Suzaku Observation of the RCW86 Northeastern Shell", Publications of the Astronomical Society of Japan, 60(SP1):123-130.

[95] Yamaguchi, H., Koyama, K. and Uchida, H., (2012). "Suzaku View of the Supernova Remnant RCW 86: X-Ray Studies of Newly-Discovered Fe-Rich Ejecta", Publications of the Astronomical Society of Japan, 63(SP3):837-848.

[96] Castro, D., Lopez, L. A., Slane, P. O., Yamaguchi H., Ramirez-Ruzi, E. and Figueroa-Feliciano, E., (2013). "A Chandra View of Non-Thermal Emission in the Northwestern Region of Supernova Remnant RCW 86: Particle Acceleration and Magnetic Fields", The Astrophysical Journal, 779(1).

[97] Broersen, S., Chiotellis, A., Vink, J. and Bamba, A., (2014). "The Many Sides of RCW 86: A Type Ia Supernova Remnant Evolving in its Progenitor's Wind Bubble", Monthly Notices of the Royal Astronomical Society, 441(4):3040-3054.

[98] Yamaguchi, H., Katsuda, S., Castro, D., Williams, B. J., Lopez, L. A., Slane, P. O., Smith, R. K. and Petre, R., (2016). "The Refined Shock Velocity of the X-Ray Filaments in the RCW 86 Northeast Rim", The Astrophysical Journal

Letters, 820(1).

[99] Tsubone, Y., Sawada, M., Bamba, A. Katsuda, S. and Vink, J., (2017). "A Systematic Study of the Thermal and Nonthermal Emission in the Supernova Remnant RCW 86 with Suzaku", The Astrophysical Journal, 835(1).

[100] Bamba, A., Terada, Y. Hewitt, J., Petre, R., Angelini, L., Safi-Harb, S., Zhou, P., Bocchino, F. and Sawada, M., (2016). "Discovery of X-Ray Emission from the Galactic Supernova Remnant G32.8-0.1 with Suzaku", The Astrophysical Journal, 818(1).

[101] Pannuti, T. G. and Allen, G. E., (2002). "Observations of the Non-Thermal X-ray Emission from the Galactic Supernova Remnant G347.3-0.5", Neutron Stars in Supernova Remnants, ASP Conference Series, 14-17 August 2001, Boston.

[102] Uchiyama, Y., Takahashi, T. and Aharonian, F. A., (2002). "Flat Spectrum X-Ray Emission from the Direction of a Molecular Cloud Associated with SNR RX J1713.7–3946", Publications of the Astronomical Society of Japan, 54(5):L73-L77.

[103] Pannuti, T. G., Allen, G. E., Houck, J. C. and Sturner, S. J., (2003). "RXTE, ROSAT, and ASCA Observations of G347.3–0.5 (RX J1713.7–3946): Probing Cosmic-Ray Acceleration by a Galactic Shell-Type Supernova Remnant", The Astrophysical Journal, 593(1).

[104] Cassam-Chenaï, G., Decourchelle, A., Ballet, J., Sauvageot, J.-L., Dubner, G. and Giacani, E., (2004). "XMM-Newton Observations of the Supernova Remnant RX J1713.7−3946 and Its Central Source", Astronomy and Astrophysics, 427:199-216.

[105] Hiraga, J. S., Uchiyama, Y., Takahashi, T. and Aharonian, F. A., (2005). "Spectral Properties of Nonthermal X-ray Emission from the Shell-type SNR RX J1713.7 3946 as Revealed by XMM-Newton", Astronomy and Astrophysics, 431(3):953-961.

[106] Zhang, L. and Yang, C. Y., (2011). "X-Ray and Gamma-Ray Emission of the Shell-Type Supernova Remnant RX J1713.7–3946", Publications of the Astronomical Society of Japan, 63:89-94.

[107] Takahashi, T., Tanaka, T., Uchiyama, Y., Hiraga, J. S., Nakazawa, K., Watanabe, S., Bamba, A., Hughes, J. P., Katagiri, H., Kataoka, J., Kokubun, M., Koyama, K., Mori, K., Petre, R., Takahashi, H. and Tsuboi, Y., (2008). "Measuring the Broad-band X-Ray Spectrum from 400 eV to 40 keV in the Southwest Part of the Supernova Remnant RX J1713.7−3946", Publications of the Astronomical Society of Japan, 60(sp1):S131-S140.

[108] Reynolds, S. P., (1998). "Models of Synchrotron X-Rays from Shell Supernova Remnants", The Astrophysical Journal, 493(1):375-396.

[109] Tanaka, T., Uchiyama, Y., Aharonian, F. A., Takahashi, T., Bamba, A., Hiraga, J. S., Kataoka, J., Kishishita, T., Kokubun, M., Mori, K., Nakazawa, K., Petre, R., Tajima, H. and Watanabe, S., (2008). "Study of Nonthermal Emission from SNR RX J1713.7−3946 with Suzaku", The Astrophysical Journal, 685(2):988-1004.

[110] Acero, F., Ballet, J., Decourchelle, A., Lemoine-Goumard, M., Ortega, M.,

Giacani, E., Dubner, G. and Cassam-Chenaï, G., (2009). “A Joint Spectro-imaging Analysis of the XMM-Newton and HESS Observations of the Supernova Remnant RX J1713.7−3946”, Astronomy and Astrophysics, 505(1):157-167.

[111] Fan, Z. H., Liu, S. M., Yuan, Q. and Fletcher, L., (2010). “Lepton Models for TeV Emission from SNR RX J1713.7−3946”, Astronomy and Astrophysics, 517.

[112] Sano, H., Tanaka, T., Torii, K., Fukuda, T., Yoshiike, S., Sato, J., Horachi, H., Kuwahara, T., Hayakaw, T., Matsumoto, H., Inoue, T., Yamazaki, R., Inutsuka, S., Kawamura, A., Tachihara, K., Yamamoto, H., Okuda, T., Mizuno, N., Onishi, T., Mizuno, A. and Fukui, Y., (2013). “Non-thermal X-Rays and Interstellar Gas Toward the γ-Ray Supernova Remnant RX J1713.7−3946: Evidence for X-Ray Enhancement around CO and H I Clumps”, The Astrophysical Journal, 778(1).

[113] Sano, H., Fukuda, T., Yoshiike, S., Sato, J., Horachi, H., Kuwahara, T., Torii, K., Hayakawa, T., Tanaka, T., Matsumoto, H., Inoue, T., Yamazaki, R., Inutsuka, S., Kawamura, A., Yamamoto, H., Okuda, T., Tachihara, K., Mizuno N., Onishi, T., Mizuno, A., Acero, F. and Fukui, Y., (2015). “A Detailed Study of Non-Thermal X-ray Properties and Interstellar Gas Toward the γ-Ray Supernova Remnant RX J1713.7−3946”, The Astrophysical Journal, 799(2).

[114] Katsuda, S., Acero, F., Tominaga, N., Fukui, Y., Hiraga, J. S., Koyama, K., Lee, S., Mori, K., Nagataki, S., Ohira, Y., Petre, R., Sano, H., Takeuchi, Y., Tamagawa, T., Tsuji, N., Tsunemi, H. and Uchiyama, Y., (2015). “Evidence for Thermal X-Ray Line Emission from the Synchrotron-dominated Supernova Remnant RX J1713.7−3946”, The Astrophysical Journal, 814(1).

[115] Sezer, A., Yamazaki, R., Cui, X., Bamba, A. and Ohira, Y., (2016). “Searching for the Time Variation in Supernova Remnant RX J1713.7−3946”, Supernova Remnants: An Odyssey in Space after Stellar Death, 6-11 June 2016, Chania.

[116] Tsuji, N. and Uchiyama, Y., (2016). “Expansion Measurements of Supernova Remnant RX J1713.7-3946”, Publications of the Astronomical Society of Japan, 68(6).

[117] Yasumi, M., Nobukawa, M., Nakashima, S., Uchida, H., Sugawara, R., Tsuru, T. G., Tanaka, T. and Koyama, K., (2014). “Abundances in the ejecta of core-collapse supernova remnants G350.1-0.3 and G349.7+0.2”, Publications of the Astronomical Society of Japan, 66(4).

[118] Lazendic, J. S., Wardle, M., Burton, M. G., Yusef-Zadeh, F., Green, A. J. and Whiteoak, J. B., (2004). “Shocked molecular hydrogen towards the Tornado nebula”, Monthly Notices of the Royal Astronomical Society, 354(2):393-400.

[119] Acero, F., Ballet, J. and Decourchelle, A., (2007). “The Gas Density Around SN 1006”, Astronomy and Astrophysics, 475(3):883-890.

[120] Yamaguchi, H., Koyama, K., Katsuda, S., Nakajima, H., Hughes, J. P., Bamba, A., Hiraga, J. S., Mori, K., Ozaki, M. and Tsuru, T. G., (2008). “X-Ray Spectroscopy of SN 1006 with Suzaku”, Publications of the Astronomical Society of Japan, 60(SP1):S141-S152.

[121] Miceli, M., Bocchino, F., Iakubovskyi, D., Orlando, S., Telezhinsky, I., Kirsch,

M. G. F., Petruk, O., Dubner, G. and Castelletti, G., (2009). "Thermal Emission, Shock Modification, and X-ray Emitting Ejecta in SN 1006", Astronomy and Astrophysics, 501(1):239-249.

[122] Miceli, M., Bocchino, F., Decourchelle, A., Maurin, G., Vink, J., Orlando, S., Reale, F. and Broersen, S., (2012). "XMM-Newton Evidence of Shocked ISM in SN 1006: Indications of Hadronic Acceleration", Astronomy & Astrophysics, 546.

[123] Broersen, S., Vink, J., Miceli, M., Bocchino, F., Maurin, G. and Docourchelle, A., (2013). "The Northwestern Ejecta Knot in SN 1006", Astronomy & Astrophysics, 552.

[124] Miceli, M., Bocchino, F., Decourchelle, A., Vink, J., Broersen, S. and Orlando, S., (2013). "The Shape of the Cutoff in the Synchrotron Emission of SN 1006 Observed with XMM-Newton", Astronomy & Astrophysics, 556.

[125] Yu, H., Fang, J., Zhang, P. F. and Zhang, L., (2015). "Three-dimensional Magnetohydrodynamic Studies of the Non-Thermal X-ray Morphologies of SN 1006", Astronomy & Astrophysics, 579.

[126] Miceli, M., Orlando, S., Pereira, V., Acero, F., Katsuda, S., Decourchelle, F., Winkler, P., Bonito, R., Reale, F., Peres, G., Li, J. and Dubner, G., (2016). "Modeling the Shock-cloud Interaction in SN 1006: Unveiling the Origin of Nonthermal X-ray and γ-ray Emission", Astronomy & Astrophysics, 593.

[127] Dubner, G. M., Giacani, E. B., Goss, W. M., Green, A. J. and Nyman, L.-Å, (2002). "The neutral gas environment of the young supernova remnant SN 1006 (G327.6+14.6)", Astronomy and Astrophysics, 387:1047-1056.

[128] Uchida, H., Yamaguchi, H. and Koyama, K., (2013). "Asymmetric Ejecta Distribution in SN 1006", The Astrophysical Journal, 771(1).

[129] Bamba, A., Yamazaki, R. and Hiraga, J. S., (2005). "Chandra Observations of Galactic Supernova Remnant Vela Jr.: A New Sample of Thin Filaments Emitting Synchrotron X-Rays", The Astrophysical Journal, 632(1):294-301.

[130] Telezhinsky, I., (2009). "A New Model for Vela Jr. Supernova Remnant", Astroparticle Physics, 31(6):431-436.

[131] Iyudin, A. F., Pakhomov, Y. V., Chugai, N. N., Greiner, J., Axelsson, M., Larsson, S. and Ryabchikova, T. A., (2010). "Search for Broad Absorption Lines in Spectra of Stars in the Field of Supernova Remnant RX J0852.0-4622 (Vela Jr.)", Astronomy and Astrophysics, 519:A86.

[132] Acero, F., Gallant, Y., Terrier, R., Renaud, M. and Ballet, J., (2011). "A New Nearby PWN Overlapping the Vela Jr. SNR", Memorie della Societa Astronomica Italiana, 82:752.

[133] Allen, G. E., Chow, K., DeLaney, T., Filipović, M. D., Houck, J. C., Pannuti, T. G. and Stage, M. D., (2015). "On the Expansion Rate, Age, and Distance of the Supernova Remnant G266.2-1.2 (Vela Jr.)", The Astrophysical Journal, 798(2).

[134] Truelove, K. J. and McKee, C. F., (1999). "Evolution of Nonradiative Supernova Remnants", The Astrophysical Journal, 120(2):299-326.

[135] Takeda, S., Bamba, A., Terada, Y., Tashiro, M. S., Katsuda, S., Yamazaki, R., Ohira, Y. and Iwakiri, W., (2016). "Suzaku Observations of the Hard X-ray

Spectrum of Vela Jr. (SNR RX J0852.0-4622)", Publications of the Astronomical Society of Japan, 68(SP1).

[136] Aharonian, F., Akhperjanian, A. G., Bazer-Bachi, A. R.,Beilicke, M., Benbow, W. Berge, D., Bernlöhr, K., Boisson, C., Bolz, O., Borrel, V., Braun, I., Brown, A. M., Bühler, R., Büsching, I., Carrigan, S., Chadwick, P. M., Chounet, L.-M., Coignet, G., Cornils, R., Costamante, L. et al., (2007). "H.E.S.S. Observations of the Supernova Remnant RX J0852.0-4622: Shell-Type Morphology and Spectrum of a Widely Extended Very High Energy Gamma-Ray Source", The Astrophysical Journal, 661(1):236-249.

[137] Hiraga, J. S., Kobayashi, Y., Tamagawa, T., Hayato, A., Bamba, A. Terada, Y., Petre, R., Katagiri, H. and Tsunemi, H., (2009). "Search for Sc-K Line Emission from RX J0852.0-4622 Supernova Remnant with Suzaku", Publications of the Astronomical Society of Japan, 61(2):275-281.

[138] Reynolds, S. P. and Keohane, J. W., (1999). "Maximum Energies of Shock-accelerated Electrons in Young Shell Supernova Remnants", The Astrophysical Journal, 525(1):368-374

[139] Pannuti, T., Allen, G. E., Fite, N. D., Grimes, C. K., Goff, E. J. and Murray, T. M., (2010). "Radio and X-ray Observations of the Galactic Supernova Remnant G156.2+5.7", American Astronomical Society, 42.

[140] Koyama, K., Petre, R., Gotthelf, E. V., Hwang, U., Matsuura, M., Ozaki, M. and Holt, S. S, (1995). "Evidence for shock acceleration of high-energy electrons in the supernova remnant SN1006", 378(6554):255-258.

[141] Yamazaki, R., Ohira, Y., Sawada, M. and Bamba, A., (2014). "Synchrotron X-ray diagnostics of cutoff shape of nonthermal electron spectrum at young supernova remnants", Research in Astronomy and Astrophysics, 14(2):165-178.

[142] Jun, B. And Jones, T. W., (1999). "Radio Emission from a Young Supernova Remnant Interacting with an Interstellar Cloud: Magnetohydrodynamic Simulation with Relativistic Electrons", The American Astronomical Society, 511(2):774-791.

[143] Kishishita, T., Hiraga, J. And Uchiyama, Y. (2013). "Nonthermal emission properties of the northwestern rim of supernova remnant RX J0852.0-4622", Astronomy & Astrophysics, 551.

[144] Parizot, E., Marcowith, A., Ballet, J. and Gallant, Y. A., (2006). "Observational constraints on energetic particle diffusion in young supernovae remnants: amplified magnetic field and maximum energy", Astronomy and Astrophysics, 453(2):387-395.

[145] Fesen, R. A., Hammell, M. C., M., J., Chevalier, R. A., Borkowski, K. J., Dopita, M. A., Gerardy, C. L., Lawrence, S. S., Raymond, J. C. and van den Bergh, S., (2006). "The Expansion Asymmetry and Age of the Cassiopeia A Supernova Remnant", 645(1):283-292.

[146] Castro, D., Lopez, L. A., Slane, P. O., Yamaguchi, H., Ramirez-Ruiz, E. and Figueroa-Feliciano, E., (2013). "A Chandra View of Non-Thermal Emission in the Northwestern Region of Supernova Remnant RCW 86: Particle Acceleration and Magnetic Fields", The Astrophysical Journal, 779(1).

[147] Bocchino, F., Vink, J., Favata, F., Maggio, A. and Sciortino, S., (2000). "A

BeppoSAX and ROSAT view of the RCW86 supernova remnant", Astronomy and Astrophysics, 360:671-682.

[148] Dyer, K. K., Reynolds, S. P., Borkowski, K. J., Allen, G. E. And Petre, R., (2001). "Separating Thermal and Nonthermal X-Rays in Supernova Remnants. I. Total Fits to SN 1006 AD", The American Astronomical Society, 551(1).

[149] Morlino, G., Amato, E., Blasi, P. and Caprioli, D., (2010). "Spatial structure of X-ray filaments in SN 1006", Monthly Notices of the Royal Astronomical Society, 405(1): L21-L25.

[150] Uchiyama, Y., Aharonian, F. A., Tanaka, T., Takahashi, T. And Maeda, Y., (2007). "Extremely fast acceleration of cosmic-rays in a supernova remnant". Nature, 449:576-578.

[151] Takeda, S., Bamba, A., Terada, Y., Tashiro, M. S., Katsuda, S., Yamazaki, R., Ohira, Y., and Iwakiri, W., (2016). "Suzaku observations of the hard X-ray spectrum of Vela Jr. (SNR RX J0852.0-4622)", Publications of the Astronomical Society of Japan, 68(SP1).

[152] Vink, J. and Laming, J. M., (2003). "On the Magnetic Fields and Particle Acceleration in Cassiopeia A", The Astrophysical Journal, 584(2):758-769.

[153] Nakamura, R., Bamba, A., Dotani, T., Ishida, M., Yamazaki, R. and Kohri, K., (2012). "Evolution of Synchrotron X-Rays in Supernova Remnants", The Astrophysical Journal, 746(2).

[154] Reynolds, S. P., Borkowski, K. J., Green, D. A., Hwang, U., Harrus, I. and Petre, R., (2009). "X-Ray Spectral Variations in the Youngest Galactic Supernova Remnant G1.9+0.3", The Astrophysical Journal Letters, 695(2):L149-L153.

[155] Zoglauer, A., Reynolds, S. P., An, H., Boggs, S. E., Christensen, F. E., Craig, W. W., Fryer, C. L., Grefenstette, B. W., Harrison, F. A., Hailey, C. J., Krivonos, R. A., Madsen, K. K., Miyasaka, H., Stern, D. and Zhang, W. W., (2015). "The Hard X-Ray View of the Young Supernova Remnant G1.9+0.3", The Astrophysical Journal, 798(2).

[156] Borkowski, K. J., Rho, J., Reynolds, S. P. and Dyer, K. K., (2001). "Thermal and Nonthermal X-Ray Emission in Supernova Remnant RCW 86", The Astrophysical Journal, 550(1):334-345.

[157] Yamazaki, R., Kohri, K., Bamba, A., Yoshida, T., Tsuribe, T. and Takahara, F., (2006). "TeV γ-rays from old supernova remnants", Monthly Notices of the Royal Astronomical Society, 371(4):1975-1982.

[158] Aharonian, F. A. and Atoyan, A. M., (1999). "On the origin of TeV radiation of SN 1006", Astronomy and Astrophysics, 351:330-340.

[159] Bamba, A. (2004). A Detailed Spatial and Spectral Study of Synchrotron X-rays from Supernova Remnants with Chandra, PhD Thesis, Department of Physics, Graduate School of Science, Kyoto University, Kyoto, Japan.

CURRICULUM VITAE

PERSONAL INFORMATION

Name Surname : Nergis CESUR

Date of birth and place : 07.07.1988, Shumen/Bulgaria

Foreign Languages : English, German, Bulgarian

E-mail : nergiscesur7@gmail.com

EDUCATION

Degree	**Department**	**University**	**Date of Graduation**
Master	Physics	Yıldız Technical University	2018
Undergraduate	Physics	Yıldız Technical University	2015
Associate	Computer Tech. & Programming	İstanbul University	2010
High School	Computer Technologies	Hikmet Nazif K. Anatolian Vocational High School	2007

WORK EXPERIENCE

Year	**Corporation/Institute**	**Enrollment**
2018 – Current	Turkish Air Force Academy	Instructor
2017 – Current	Yıldız Technical University	Graduate Student Assistant
2016 – 2018	Yıldız Technical University Technology Transfer Office	Project Assistant
2016 – 2017	Turkish Astronomical Society Journal	News Editor
2010	Oyak Technology	Intern
2009 – 2010	İstanbul University	Student Assistant
2008	Casper Computer Systems	Intern

PUBLISHMENTS

Papers

Cesur, N., An X-ray study of the plerionic composite supernova remnant 3C 396, Turkish Journal of Physics *(submitted)*.

1 Cesur, N., Sezer, A., and Hüdaverdi, M., (2018). The Effects of X-ray Background on the X-ray Emission from the Galactic Supernova Remnants, Turkish Journal of Physics *(submitted)*.

2. Cesur, N., Sezer, A. and Hüdaverdi, M., (2018). "Spectral Properties of the Galactic Supernova Remnant Vela Jr. (G266.2-1.2) Using Chandra", Turkish Journal of Physics *(in press)*.

Proceedings

1. Cesur, N., Sezer, A. and Hüdaverdi, M., (2018). "An X-ray Study of the Well-known Galactic Shell-type Supernova Remnants", American Institute of Physics Conference Proceedings, 1935.

Conference Posters

1. Cesur, N., Sezer, A. and Hüdaverdi, M., (2018). "Effects of the X-ray Background Estimation on the Spectra of the Galactic Supernova Remnants", 8^{th} International Workshop on Occultation and Eclipse, 1-2 March 2018, Yıldız Technical University, İstanbul, Turkey.

2. Cesur, N. and Hüdaverdi, M., (2017). "Long Term Variable Source J141648.7+522558 at Groth-Westphal Field", Turkish Physical Society 33^{rd} International Physics Congress, 6-10 September 2017, Bodrum, Turkey.

3. Cesur, N., Sezer, A. and Hüdaverdi, M., (2017). "An X-ray Study of the Galactic Shell-type Supernova Remnants Using XMM-Newton and Chandra", The X-ray Universe, 6-9 June 2017, Rome, Italy.

4. Cesur, N., Sezer, A. and Hüdaverdi, M., (2017). "An X-Ray Analysis of Galactic Shell-Type Supernova Remnants", 1^{st} Dilhan Eryurt Astronomy Event, 22 April 2017, Middle East Technical

University, Ankara, Turkey.

5. Cesur, N. and Hüdaverdi, M., (2016). "Long Time Variable Source J141648.7+522558", 41st COSPAR Scientific Assembly, 30 July-7 August 2016, İstanbul, Turkey.